UNIVERSITY OF OKLAHOMA

GRADUATE COLLEGE

STUDY OF MULTICOMPONENT OF HYDROCARBON SYSTEMS WITH MOLECULAR DYNAMICS SIMULATION

A DISSERTATION

SUBMITTED TO THE GRADUATE FACULTY

in partial fulfillment of the requirements for the

Degree of

DOCTOR OF PHILOSOPHY

By

Qiuhao Chang

Norman, Oklahoma

2022

STUDY OF MULTICOMPONENT OF HYDROCARBON SYSTEMS WITH MOLECULAR DYNAMICS SIMULATION

A DISSERTATION APPROVED FOR THE

MEWBOURNE SCHOOL OF PETROLEUM AND GEOLOGICAL ENGINEERING

BY THE COMMITTEE CONSISTING OF

Dr. Xingru Wu, Chair

Dr. Liangliang Huang, Co-Chair

Dr. Mashhad Fahes

Dr. Yingtao Liu

Dr. Benjamin Shiau

Dr. Hamidreza Karami

Acknowledgments

I would like to express my sincere gratitude to my advisors, Dr. Xingru Wu, and Dr. Liangliang Huang, for their instructive advice in my research studies, for their great care and support in my daily life, and their valuable guidance in my career planning. Without their consistent and illuminating instruction, I couldn't finish my Ph.D. program at OU. I am so lucky and proud that Dr. Wu and Dr. Huang could be my advisors.

I appreciate my committee members, Dr. Mashhad Fahes, Dr. Yingtao Liu, Dr. Benjamin Shiau, and Dr. Hamidreza Karami, for their suggestions and insightful comments on my research. I would also like to extend my appreciation to Dr. Edgar A. O'Rear III, Dr. Musharraf Zaman, and Sagar Ghos for their contributions to the construction of the new asphalt model and discussions on experimental studies of asphalt properties. I also thank the OU Supercomputing Center for Education & Research (OSCER) for providing me with the use of powerful and advanced computing facilities during my entire Ph.D. program.

I want to thank my colleagues and friends, Qi Qiao, Guobing Zhou, and Yixin Ma, all of whom gave me great help in the early stage of learning and using molecular dynamics simulation. I also want to thank my friends, Xuxin Chen, Ke Zhang, and Xinglei Zhang who helped me through the struggling time during my research and colored my daily life at OU.

Last but not least, I express my deepest gratitude to my beloved parents who have always been encouraging me and supporting me without any complaint.

Table of Contents

List of Tables

List of Figures

Abstract

Molecular Dynamics (MD) simulation is a powerful tool used in various research fields such as petroleum, geoscience, biochemistry, physics, and materials science. The unique merit of MD simulation is that it can investigate the complex structures or systems of interest at the atomic or molecular level, which could be inaccessible to experimental methods. A naturally accumulated hydrocarbon reservoir is a complex multi-component system where complex phase behavior occurs when different recovery techniques are applied. Given that hydrocarbons are stored in nanoscale to mesoscale pores, MD simulations have widely been used in petroleum engineering to study the interaction between pore-wall and fluids inside the pore body. For example, MD simulation has been widely used to observe the adsorption/desorption and diffusion of gas molecules in carbon nanotube/nanoslit for understanding the gas behaviors in the shale reservoir. Similarly, hydrocarbon products such as asphalts are complex mixtures that pose challenges in molecular-level studies but can be good candidates for MD simulation. In summary, MD has been used in this dissertation research to study the interfacial tension change for CO_2 EOR and rejuvenating asphalt.

The first research project uses MD to study the options for rejuvenating aged asphalts with waste cooking oil (WCO) and waste polyethylene (WPE). The asphalt binder in pavement degrades over time due to oxidation and loss of volatile components resulting from weathering and utilization. Using waste to modify and recycle aged asphalt brings environmental and economic benefits. MD study of WCO for the aged asphalt shows that adding 10 wt% Triglyceride (TG, the main component of WCO) can decrease the viscosity (from 83 cP to 69 cP) and increase the self-diffusion coefficient (from $2.81 \times 10^{-7}$to

$3.24 \times 10^{-7}\ \frac{cm^2}{s}$) of aged asphalt at its compaction conditions. The radial distribution function analysis revealed that the asphaltene-asphaltene nearest neighbor distance increased from 4.0 Å to 7.5 Å. The optimal dosage of TG was determined, which should be in the range of 10-15 wt% of aged asphalt. The results illustrate the fundamental mechanism of using the WCO to reclaim aged asphalt.

The WPE simulation shows that adding WPE could reduce the interactions between asphaltenes-resins, asphaltenes-aromatics, and asphaltenes-saturates. Low compatibility between asphalt and polyethylene results in phase separation of PE-modified asphalt. The maleic anhydride functional group (MAH) is chemically grafted on WPE (WPE-g-MAH) to enhance the compatibility and stability between PE and asphalt. The simulation results show that adding MAH functional group enhanced the interactions between asphaltenes-saturates and asphaltenes-aromatics, which was why MAH could enhance the compatibility between asphalt and WPE. Moreover, the simulation results demonstrated that both WPE and WPE-g-MAH couldn't affect the interactions between asphaltenes-asphaltenes and mitigate the formation of asphaltene aggregations/clusters in aged asphalt, indicating PE and PE-g-MAH are not potential options to restore the rheological properties of aged asphalt.

The second project in this dissertation research uses MD simulation to study the interfacial tension between CO_2-rich oil and the aqueous phase, which could fundamentally explain one of the synergetic driving mechanisms for CO_2-related EOR. Recent laboratory tests showed promising results using urea as a CO_2-generating agent for in-situ CO_2 EOR. However, laboratory tests could not quantify the interfacial tension changes due to CO_2

partitioning to the oil and aqueous phases. MD simulation is performed to study the interface and properties of the CO_2/water/oil multi-components system in this research project. The simulation results demonstrate that the CO_2 concentration of 40% is required to achieve a good reduction of the water/oil IFT for low-pressure conditions (<10 MPa) with 345 K, and that the water/oil IFT decreases significantly when the CO_2 concentration is between 0 and 40%. While at higher CO_2 concentrations of 40–80%, the IFT reduction is small. The literature has not reported this relationship between water/oil IFT and CO_2 concentration. Our findings quantify the contribution of IFT reduction to oil recovery in CO_2 EOR techniques. In addition, at low CO_2 concentrations of 0~40%, CO_2 molecules would change the orientation from the random distribution to parallel to the water/oil interface. Once the contact region of water/oil is saturated by CO_2 molecules at around 40% concentration, increasing the CO_2 concentrations does not change much of the IFT or CO_2 orientation. This study illustrates the mechanism of IFT reduction from the molecular perspective that interfacial CO_2 orientation is affected by bulk CO_2 concentration and is closely correlated to the IFT change between oil and aqueous phases. The fundamental study of CO_2 behavior at the water-oil interface is important to in-situ CO_2 EOR and all CO_2 flooding mechanisms. In addition, the procedures and analysis methods can be applied to other EOR projects for binary and multi-component systems studies for IFT analysis and property computation.

Chapter 1: Introduction

1.1 Research Motivations

In the late 20th century, the application of molecular simulation in science was introduced as a "computer experiment" to fill the gap between the theory and the traditional experimental method. In theoretical studies, mathematical equations are developed to study the behavior of a system, while it is only expected to produce valid results under a specific assumption or at a level at which the equations of the mathematical model can be solved. For example, an equation of state (EoS) could only study the phase behavior of fluid under a bulk condition, not a confined condition. The traditional experiment could provide observations but cannot reveal fundamental mechanisms from the molecular level. The cost of the experiments is also an issue. It is not feasible to perform experiments under extremely high pressure and high temperature conditions. Molecular simulation is a valuable research tool for studies and conditions where theory and experimental methods are limited[1-4].

Covering over 90% of the roads in the United States, asphalt pavement is comprised primarily of rock or "aggregate" held together by an asphalt binder. The asphalt concrete degrades over time due to oxidation and loss of volatile components resulting from weathering. The stiffer physical properties lead to cracking and fragmentation, and eventual pavement failure. Recycling and reusing aged asphalt as the binder in pavement brings economic and environmental benefits. For example, in the United States, it was reported that reclaimed asphalt pavement (RAP) with estimated savings of $2.04 billion at $600 per ton for asphalt binder in 2012[5]. Poor properties after aging have been cited as the

major impediment to asphalt recycling [6]. Recycling asphalt necessitates chemical additives, at the very least, rejuvenating agents. Rejuvenators can restore the rheological properties of asphalt so that recycling becomes economically and functionally attractive. Some of the wastes are considered the rejuvenator for aged asphalt reclamation, which explores a new way of waste disposal. Among different wastes, waste cooking oil (WCO) and waste polyethylene (WPE) have been experimentally shown to function effectively as rejuvenators[7-9]. However, their performance in a sustainable pavement will significantly depend on favorable molecular interactions with the aged asphalt, and the molecular-level mechanism has not been fully understood.

Understanding the molecular interactions between wastes and aged asphalt is difficult to achieve through theoretical and experimental methods. Therefore, the first research work is motivated to obtain a molecular-level understanding of interactions between aged asphalt with wastes and to construct, via MD simulation, a relationship between the microstructure of waste-modified asphalt and its macroscopic properties.

The CO_2-EOR is one of the most effective tertiary EOR techniques[10, 11]. In the United States, CO_2-EOR has been implemented in more than a thousand oil reservoirs, and more than 100 billion barrels of crude oil have been recovered from this technology. For CO_2-based EOR, CO_2 would partition into the oil and aqueous phases, which reduces the interfacial tension and thus improves the microscopic displacement efficiency by increasing mobilities of both displacing and displaced fluids. Because the synergetic mechanism of the magnitude of IFT reduction between CO_2-saturated brine and oil is affected by the interfacial properties between oil and aqueous phases, it is necessary to study the interfacial properties between oil and aqueous phases with the presence of CO_2.

However, it is hard to observe and analyze the nano-scale interface and its property via traditional experimental apparatus. In the literature review, MD simulation has been widely used to observe the molecular behavior at the interface and study the interfacial properties of the binary systems of water-oil, water-CO_2, oil-CO_2, and the ternary system of water-oil-CO_2. Thus, the second research work is motivated to study the water-oil interfacial properties with the presence of CO_2 via MD simulation.

1.2 Research Objectives

In the first project of rejuvenating aged asphalt, the objectives include the following:

- To develop a new aged asphalt model that could capture the nature of aged asphalt and the chemistry change of asphalt under aging.
- To develop the wastes modified asphalt models by introducing the WCO and WPE into new aged asphalt model
- To study the effect of additional wastes on molecular interactions in aged asphalt and its response to macroscopic properties of aged asphalt.
- To validate the fundamental mechanism and illustrate the field performance of waste-modified asphalt.

To study the fundamental mechanism of water/oil IFT reduction during CO_2 EOR and demonstrate the contribution of IFT reduction to oil recovery. This project has the following objectives:

- To construct a binary system of water/oil with the presence of CO_2 to simulate the realistic reservoir condition during the CO_2 EOR process.

- To determine the relationship between water/oil IFT with the concentration of CO_2 for investigating the contribution of IFT reduction to oil recovery.
- To analyze the molecular behaviors of CO_2 at the water-oil interface to study the fundamental mechanism of water-oil IFT reduction during the CO_2 EOR process.

1.3 Organization of Dissertation

Chapter 2 introduces the chemical composition of asphalt and its fundamental oxidation mechanism. The research status of WCO-modified asphalt, waste plastics-modified asphalt, and the background of CO_2-EOR is concluded in this chapter as well. In addition, the core theories of MD simulation are also introduced, including the fundamental theory, the simulation algorithms, the simulation ensembles, the force field concept, and the periodic boundary condition. Last, the applications of MD simulation in the petroleum industry and asphalt modeling are summarized in this chapter.

In chapter 3, a new aged asphalt model was proposed to capture the chemistry change of asphalt under aging. The new aged asphalt model is used to study the molecular interaction and microstructure of aged asphalt. In addition, the relationships between the microstructure and two of the most important macroscopic properties of aged asphalt, shear viscosity and self-diffusion, are investigated.

In chapter 4, the WCO is used to rejuvenate the aged asphalt, particularly to restore the viscosity and self-diffusion of aged asphalt. The corresponding rejuvenation mechanism is investigated by analyzing the molecular interaction and microstructure of aged asphalt and WCO-modified aged asphalt.

In chapter 5, as one of the most common waste plastics, WPE is used to modify aged asphalt. The effects of WPE on the molecular interaction and microstructure of aged asphalt are studied.

In chapter 6, the behaviors of CO_2 at the water-oil interface and its effect on water-oil interfacial properties such as IFT, orientation, and phase interaction are studied at the low-pressure condition of 8 MPa and 345 K.

Chapter 7 highlights the contributions and summarizes the conclusions of this research work with recommended future work.

Chapter 2: Related Research Backgrounds

2.1 Literature Review

A comprehensive literature review related to asphalt composition, asphalt aging, aged asphalt reclamation with wastes, and CO_2-EOR is concluded in this chapter.

2.1.1 Chemistry of Asphalt

Asphalt composes millions of molecules depending on the sources and petroleum refinery. Most asphalts consist of predominantly hydrocarbons, some heteroatoms (such as nitrogen, oxygen, and sulfur), and minerals in the form of inorganic salts and oxides such as nickel, vanadium, iron, and magnesium[12-15]. It has been estimated that asphalt has 10^5-10^6 different molecules[16]. To define the asphalt composition, Corbett[17] proposed the SARA fractions method by dividing the asphalt composition into asphaltenes and maltenes based on their solubility in n-Heptane. The maltenes were divided into saturates, aromatics, and resins according to the size and solubility in polar, non-polar, or aromatic solvents. Thus, the composition of asphalt is divided into four fractions, saturates (S), aromatics (A), resins (R), and Asphaltenes (A).

Asphaltenes are the largest polar components of asphalt, contributing the largest to its viscosity[18]. Asphaltenes normally constitute 5 – 25 wt% of asphalt. The asphaltenes are insoluble in light alkanes such as n-pentane, n-hexane, or n-heptane but are soluble in aromatic solvents such as benzene and toluene. Saturates are light and non-polar molecules that consist of aliphatic chains with branched and cyclic alkanes[19]. The saturates normally constitute 5-15 wt% of asphalt. They show low chemical reactivity and are highly resistant to ambient air oxidation. Aromatics constitute 30-45 wt% of asphalt. The aromatics consist

of non-aromatic rings and non-polar carbon chains. Aromatics are more viscous than saturates but less viscous than resins at the same temperature[20]. Resins are soluble in heptane and pentane. It consists of non-polar paraffinic groups and heteroatoms containing oxygen, sulfur, and nitrogen.

Various chromatographic methods can be used to separate and determine the SARA fractions of an asphalt sample based on their solubility in solvents of differing polarity and their affinity for adsorption on solid granular packing columns, e.g., natural clays, Silica gel and alumina[21]. Three chromatography methods have been employed widely for several decades, gravimetric adsorption chromatography[22, 23], High-performance Liquid Chromatography (HPLC)[24-27], and Thin-Layer Chromatography with Flame Ionization Detection (TLC-FID)[28, 29]. However, each method has its limitations and drawbacks, leading to controversies about its effectiveness, accuracy, and quantitative capability.

Gravimetric adsorption chromatography, also known as clay-silica gel adsorption chromatography, was the earliest method developed for SARA fractions. In this method, the alkane solvent (n-pentane, n-heptane) was first used to precipitate the asphaltene fraction. After de-asphalting, the fractions that remain dissolved (maltenes) are successively passed through a clay-packed column and a silica-gel column to adsorb resins and aromatics, respectively. The final remaining fraction is saturates. This method requires large quantities of solvent and test samples and is time-consuming (up to two weeks per test). Additionally, the analysis results are not always reproducible because of light component losses[27]. HPLC is an improved method of gravimetric adsorption chromatography. This method conducts the de-asphalting process first via an alkane

solvent. In contrast, the subsequent separation of maltenes is conducted through the high-performance liquid (high-pressure liquid) with amino, cyano, silica, or alumina columns (stationary phases). The size of the stationary phase used in HPLD is much smaller than that in the gravimetric method for providing a larger contact area between maltenes and the stationary phase. This method is faster and more automated than gravimetric adsorption chromatography since it uses high pressure to drive the fluid rather than gravity. The limitation of this method is its high cost. The TLC-FID method uses silica rods as the stationary phase and subsequently evaporates the elution solvents to successively pass the rods through flame ionization detection (FID) and determines the relative amounts of SARA fractions. The de-asphalting process is not necessary for this method. The limitation of this method is that some of the polar compounds may remain on the rods, and some aromatics may act like resins during the separation process, both of which cause analytical results that show a large amount of error after repeat tests[30].

2.1.2 Aging of Asphalt

The asphalt pavement degradation over time is caused by oxidation and loss of volatile components resulting from local weather and load conditions. Oxidative aging occurs in short-term and long-term stages (**Figure 1**). Short-term aging occurs when the asphalt is subjected to heat and air in the process of asphalt mixture production, storage, transportation, and paving, primarily attributed to oxidation and loss of volatile components at high temperatures. In the laboratories, short-term aging can be simulated by Rolling Thin Film Oven (RTFO). Long-term aging of asphalt occurs over road pavement's service life, mainly through progressive oxidation[31]. Long-term aging can be simulated through the Pressure Aging Vessel (PAV) method in the laboratories[32, 33].

The aging process deteriorates the physical, mechanical, and rheological properties of asphalt, corresponding to the performance of asphalt/asphalt binder in the pavement. An optimal or desired performance of the asphalt binder is closely related to its flow properties, also known as rheological properties. A change in the rheological properties can result in a reduced asphalt performance[34]. For example, viscosity, one of the most important rheological properties of asphalt, is commonly used as an indicator for asphalt aging. An aging index can be defined as either the viscosity ratio or the relative increase of viscosity versus time[35, 36], as shown in **Figure 1**. The viscosity of asphalt significantly increases with aging[37], which hardens the surface asphalt layer and asphalt binder in the pavement and leads to embrittlement and serious pavement cracking[31].

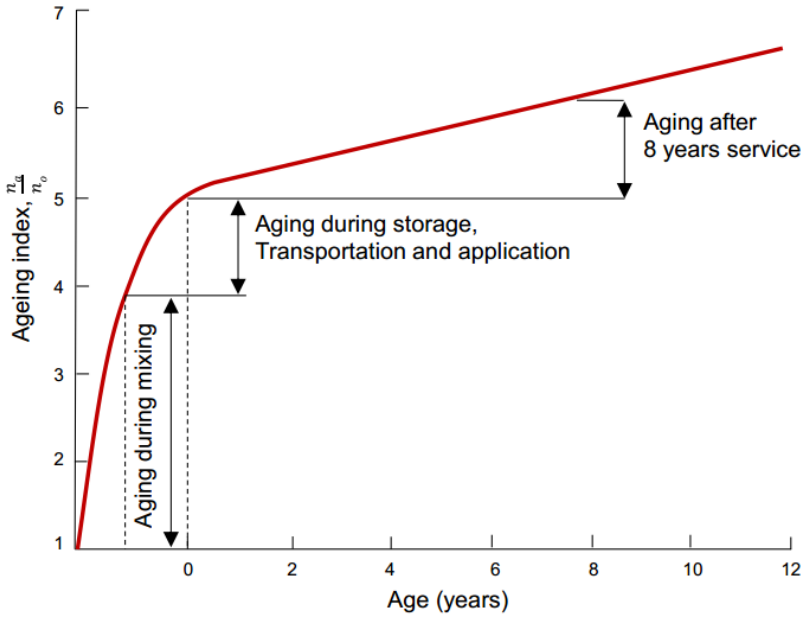

Figure 1. Viscosity aging index change over time shows the deterioration of asphats[38]. The short-term usually occurs within the first couple of years or shorter, while the long-term aging mainly occurs during its service time.

The increase of asphalt viscosity during the aging process can be explained through SARA fractions at a molecular level. According to Peterson's and Lesueur's studies[34, 35], during the aging process, asphaltenes and resins increase, and aromatics decrease in the asphalt; as the aromatics can be converted into resins, then the resins are converted into asphaltenes. The high content of asphaltenes leads to the high viscosity of asphalt. In addition, introducing oxygen-containing chemical functionalities increases the molecular interaction between asphaltenes and forms the asphaltene gel structure in asphalt as shown in **Figure 2**, which also contributes to the increase of asphalt viscosity.

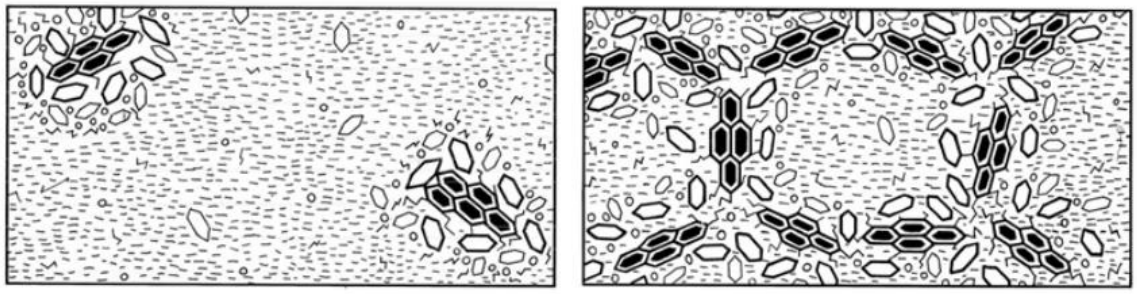

Figure 2. (left) structure of asphalt with low asphaltenes, named sol-structure. (right) Asphalt structure with asphaltenes after aging named gel-structure[39]. The solid black diamond represents asphaltenes, the white diamond represents aromatics with different molecular weights, the small circle and flash-wave represent resins with different structures, and the small straight line represents saturates.

2.1.3 Waste Cooking Oil with Asphalt

The above discussion indicates that asphalt is prone to cracking after aging due to its viscosity and hardness increase. Adding WCO could soften the hardness of asphalt and reduce its viscosity, which is the conclusion widely reported and accepted by researchers[40-47]. In addition, approximately 3 million gallons of WCO are produced annually in the U.S. alone[48]. Using WCO in asphalt pavement also provides a solution for WCO disposal and

treatment[49]. Thus, WCO has been a rejuvenator for aged asphalt pavement reclamation in recent years.

Asphalt viscosity is an important property, as highly viscous asphalt is prone to cracking. A relatively lower viscosity can reduce the mixing and compaction temperature, which is favorable for the construction site and saves costs. However, asphalt with low viscosity results in vulnerable rutting and fatigue resistance[50]. An optimal dosage for WCO could be used to avoid the negative effect on rutting and fatigue resistance. The optimal or desired performance of asphalt binder is closely related to its rheological properties. For example, Zargar *et al.* [51] tested the aged 40/50 grade bitumen with different concentrations of WCO at 135 °C and found that adding 4% WCO could achieve almost the same viscosity of 80/100-grade bitumen. Ji *et al*.[52] found that 6% waste cooking vegetable oil could restore the viscosity, rutting resistance, and fatigue resistance factor of aged asphalt binder to its virgin state. Shorbagy *et al*.[53] added the optimum dosage of 3.5% WCO into the aged 60/70 bitumen and restored the viscosity and rutting parameter ($G^*/\sin\delta$) of aged 60/70 bitumen to the value before the aging. Gökalp *et al*.[54] found that 7% waste vegetable cooking oil could restore the rutting resistance and fatigue resistance factors of aged bitumen to its virgin state. Cao *et al*.[55] compared the safety, physical, and rheological properties of an aged PEN70 asphalt sample with different dosages of waste vegetable oil to the virgin PEN70 asphalt sample. They found the optimal dosage was 13.4 wt%. Sang *et al*.[56] found that the 70[#] aged asphalt binder with 6% waste edible animal oil has the best physical and rheological properties.

2.1.4 Waste Plastic with Asphalt

In the U.S., plastic wastes were mainly disposed through landfill and incineration. The landfill has limitations such as 1) High demand for land resources[57]; 2) The chemicals leaching from the plastics into soil and water cause a serious threat to the environment; 3) The leaching of chemicals may take at least several decades since most plastics are not biodegradable. For the incineration method, the toxic emissions such as carbon monoxide and dioxin into the atmosphere prevent widespread implementation[58]. Since the 1980s, waste plastic has been used to modify the asphalt in pavements to provide a new plastic waste treatment.

Seven main types of waste plastics have been used to modify the properties of asphalt, as shown in **Figure 3**. For example, waste LDPE has been widely used as a modifier to improve the properties of asphalt worldwide since the 1990s[59]. Reinke and Gidden[60] studied the physical properties of LDPE-modified asphalt. They found that the penetration rate of asphalt decreased while the softening point and viscosity increased. Vargas *et al*.[61] observed that LDPE could lower temperature susceptibility and improve aging resistance, fatigue resistance, and resistance to deformation at high temperatures. Ho *et al*.[62] found that molecular weight and molecular weight distribution of LDPE greatly affect its compatibility with asphalt. The recycled LDPE with lower molecular weight and wider molecular weight distribution is more suitable for asphalt modification. Compared with LDPE, the high crystallinity of HDPE makes it difficult to immerse in asphalt and affects its compatibility with asphalt. Punith *et al*.[63] found that HDPE-modified asphalt has higher stiffness and larger viscosity but better moisture resistance. Balanghais *et al*.[64] studied the rheological properties of plastic-modified asphalts with LDPE, HDPE, and PET.

They found that the rheological properties of plastic-modified asphalt are very sensitive and depend on external factors such as the mixing duration and mixing methods and internal factors such as type of asphalt and type of plastic. In addition, the study reported that LDPE-modified asphalt has a better rheological performance than PET-modified asphalt and HDPE-modified asphalt.

PP could enhance the high-temperature performances of asphalt but reduce the ductility and weaken the fatigue cracking performance[65]. Recent studies[66] found that adding waste PVC could increase the viscosity and stiffness of asphalt, thus enhancing the rutting resistance of asphalt. Ziari *et al*.[67] indicated that waste PVC-modified asphalt has a better fatigue resistance but a poorer thermal cracking resistance. PET is one of the most recycled plastic wastes[68]. It was found that PET could improve the high-temperature performance but reduce the fracture resistance of asphalt[69]. Fang *et al*.[70] applied a very low-density PS waste to reduce the stiffness of asphalt and improve its rutting resistance. Hasan *et al*.[65] added the waste high-impact PS in asphalt and found the stiffness was improved, but the low-temperature properties were weakened. In addition, it has to be mentioned that harmful substances are released when PS is heated above 70 °C.

Figure 3. Seven main types of solid plastics (plasticsforchange.org, accessed on 9/28/2022).

The pre-treatment of waste plastic significantly affects its properties and its modification on asphalt. There are four types of pre-treatment of waste plastics before their application to asphalt modification: re-extrusion, mechanical method, chemical method, and energy recovery method [71]. The primary method of re-extrusion is re-introducing scrap, single-polymer plastic edges, and parts to the extrusion cycle and producing products of similar material. The limitation of this method is that it can only be applied in the case of semi-clean scrap.

The mechanical method involves reprocessing and modifying plastic waste using mechanical-physical means to form similar plastic products at nearly the same or lower

performance level compared with the original products[72]. The mechanical method can only be applied to single-polymer plastic, such as PE, PP, PS, and others. It is more difficult to use mechanical recycling on waste plastic that is more complex and contaminated. Extrusion is the foremost secondary method[73]. In this method, an extruder uses heat and rotating screws to soften the plastic. The plastic is fed through temperature-controlled barrel sections to produce a fixed cross-section extrudate, as shown in **Figure 4** [71]. The major drawback of the mechanical method is that plastic products' properties deteriorate during every cycle, and it should be noted that each plastic can endure only a limited number of reprocessing cycles[74].

Chemical recycling involves converting waste plastic into smaller molecules, usually liquids or gases (e.g., fuels, monomers), which can be used as a feedstock to produce new petrochemicals and plastics. The conversion can be gone through either solvolysis or thermolysis. During solvolysis, waste plastic is dissolved in a solvent and treated with or without catalysts and initiators. During thermolysis, waste plastic is heated in an inert atmosphere (e.g., N_2) without air or oxygen. It consists of various further processes, including pyrolysis, gasification, and hydrogenation[75]. Although the chemical method is considered an environmentally and economically feasible technique, there are still some challenges, for example, the complexity of reactions in the pyrolysis process and the high cost of hydrogen in the hydrogenation process.

In the energy recovery method, the waste plastics are incinerated in a boiler or in other industrial equipment to produce energy in the form of heat and electricity. Nevertheless, if incomplete incineration occurs, toxic substances, such as dioxins, furans,

and others, could be formed and released into the atmosphere, resulting in environmental issues[76].

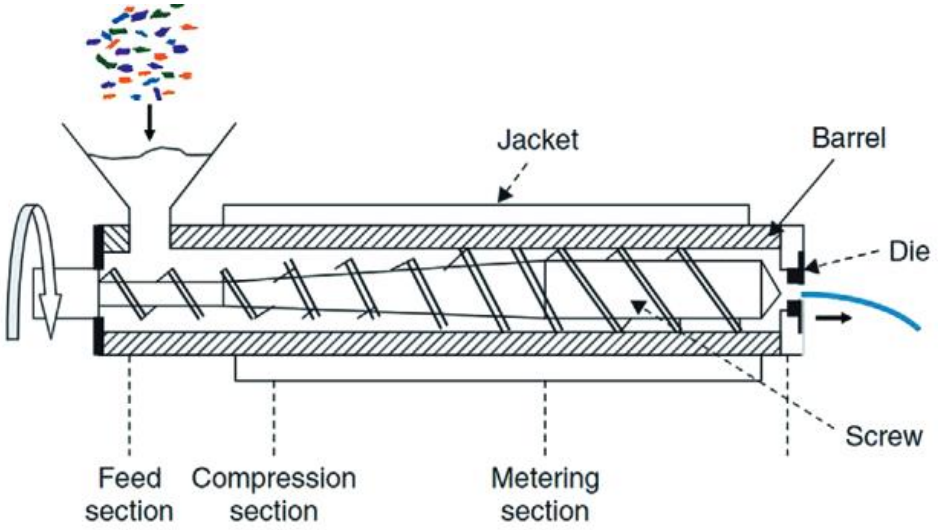

Figure 4. Extrusion process of waste plastic in a single screw extruder[71].

2.1.5 CO_2 Enhanced Oil Recovery Techniques

The tertiary enhanced oil recovery techniques are widely implemented in conventional oil fields since more than 50% of the original oil remains in the reservoir after the primary and secondary oil recovery[77, 78]. The CO_2-EOR is one of the most effective tertiary EOR techniques [10, 11]. The immiscible/miscible CO_2 flooding are two classical CO_2-EOR techniques. The miscible CO_2 flooding is designed for the reservoir with pressure above the minimum miscible pressure (MMP) of CO_2 and oil. Under this pressure condition, the injected CO_2 completely dissolves into the oil. Part of the CO_2 accumulates at the interface between the miscible oil/CO_2 phase and the aqueous phase, which reduces the interfacial tension between oil and water[79, 80]. The immiscible CO_2 flooding is designed for the reservoir with low pressure and medium/heavy oil components[81]. During the

immiscible CO_2 flooding, the injected CO_2 partially dissolves into the oil, leading to oil swelling and viscosity reduction[82, 83].

In places where supercritical CO_2-EOR is infeasible, in-situ CO_2 generation can be used. The In-situ CO_2 EOR(ICE) combines chemical and CO_2 EORs. This method injects the chemical agent with water into the reservoir, releasing CO_2 and other relevant products. Different chemical agents have been used to apply ICE, for example, ammonium carbamate, aluminum carbamide, ammonium bicarbonate, and sodium carbonate. Shiau's research group used urea(NH_2CONH_2) as the chemical agent since It exhibits a very high water solubility(1079 g/L at 20°C) and can be safely transported as a solid form or in concentrate solution with minimum hazard to humans and the environment[84]. Under the reservoir condition with a relatively high temperature, urea produces the ammonium carbamate in the aqueous solution (eq 1.1), and then ammonium carbamate decomposes into CO_2 and NH_3 (eq 1.2).

$$NH_2COONH_4 \rightleftarrows NH_2CONH_2 + H_2O \quad (1.1)$$

$$NH_2COONH_2 + H_2O \rightleftarrows 2NH_3 + CO_2 \quad (1.2)$$

From Dr.Wang's[84] and Sadam's[85] study, there are at least four oil-recovery mechanisms in the ICE process: (1) Oil swelling; (2) Oil viscosity reduction; (3) Water/oil IFT reduction; (4) Wettability reversal of reservoir rock.

According to the review above, in classical CO_2 EORs or ICE, understanding the effect of CO_2 on water-oil interfacial properties is important, especially the effect of CO_2 on water-oil IFT, which significantly affects the oil recovery efficiency[86-89].

2.2 MD Simulation and its Applications

Molecular dynamics simulation involves the application of Newton's laws of mechanics at the level of molecules and atoms. Complex structures of interest may be described with atomic detail or through the coarse-grained approach, where atoms are grouped for a simplified 3D topology representation. Inter- and intra-interactions are accounted for, including electrostatic, van der Waals, dipole, and hydrogen bonding (HB) forces between atoms. Molecular topology and flexibility due to bond stretching, bending, and rotation are also accessible to MD simulations. With the advancement of high-performance supercomputing hardware and efficient parallel software, MD simulations can deal with complex systems of hundreds or thousands of atoms and archive system evolutions up to microsecond scales.

The theories of MD simulation are quite straightforward. In general, the positions and velocities of the atoms at the initial state in the system and a description of particle interactions are needed. The particle interactions determine the forces acting on the atoms, and with the masses of the atoms known, the accelerations of atoms in the system can be determined. Positions, velocities, and accelerations are enough to determine the time evolution of the system. The output of the MD simulation is a trajectory that specifies how the positions and velocities of the atoms in the system vary with time. The simulated motion and rearrangements of mixtures of molecules with time allow the study of static and dynamics of the system, such as the radial distribution function, HB network, viscosity, and self-diffusion. Other physical properties as a function of temperature and composition can also be estimated from ensemble averages of a finite number of molecules.

2.2.1 MD Simulation Algorithms

For a system that has N particles, if r(x, y, z) is used to describe the coordinate of the particle in the system, then the potential energy of the system is $F = (F_{1x}, F_{1y}, F_{1z}, \ldots., F_{Nx}, F_{Ny}, F_{Nz})$, where $F = -\nabla V(r)$, V represents the potential energy. If the mass of the particle is known as m, the acceleration of particles in the system would be

$$a = -\left(\frac{1}{m_1}\frac{\partial V(r)}{\partial r_{1x}}, \frac{1}{m_1}\frac{\partial V(r)}{\partial r_{1y}}, \frac{1}{m_1}\frac{\partial V(r)}{\partial r_{1z}}, \ldots\ldots, \frac{1}{m_N}\frac{\partial V(r)}{\partial r_{Nx}}, \frac{1}{m_N}\frac{\partial V(r)}{\partial r_{Ny}}, \frac{1}{m_N}\frac{\partial V(r)}{\partial r_{Nz}}\right) \quad (2.1)$$

Next, several algorithms can be used to determine the relationship between $r(t)$ and $r(t + \Delta t)$, such as the verlet algorithm, leap-frog algorithm, velocity verlet algorithm, and others. For example, if the verlet algorithm is used with Taylor expansion, the $r(t + \Delta t)$ can be expressed as:

$$r(t + \Delta t) \approx r(t) + \Delta t\dot{r}(t) + \frac{1}{2}\Delta t^2 r\ddot{(t)} \quad (2.2)$$

$$\dot{r}(t) = v(t) \quad (2.3)$$

$$r\ddot{(t)}, = a(t) \quad (2.4)$$

The "over dots" represent the first and second derivatives with respect to position, which are velocity and acceleration. The $r(t - \Delta t)$ can be expressed as:

$$r(t - \Delta t) \approx r(t) - \Delta t\dot{r}(t) + \frac{1}{2}\Delta t^2 r\ddot{(t)} \quad (2.5)$$

Summing up the above two equations, the new positions and velocities of particles are:

$$r(t + \Delta t) = 2r(t) - r(t - \Delta t) + \Delta t^2 a(t) \quad (2.6)$$

$$v(t) = \frac{[r(t+\Delta t) - r(t-\Delta t)]}{2\Delta t} \quad (2.7)$$

The details of other algorithms like leap-frog and velocity verlet can be found in the book published by Frenkel and Smith[90].

2.2.2 Force Fields

The force acting on the atom is the negative derivative of its potential energy. For potential energy calculation, the molecular interaction among the atoms is defined through a force field. In MD simulation, the force field normally includes bonded and non-bonded terms. The bonded term describes the intramolecular interactions that include bond interactions between two atoms(V_{bond}), angle interactions between three atoms(V_{angle}), and dihedral interactions between four atoms($V_{dihedral}$), as shown in eq 2.8-2.10.

$$V_{bond} = \sum_{bonds} k_i^{bond}(r_i - r_0)^2 \quad (2.8)$$

$$V_{angle} = \sum_{angles} k_i^{angle}(\Theta_i - \Theta_0)^2 \quad (2.9)$$

$$V_{dihedral} = \sum_{dihedrals} k_i^{dihedral}[1 + \cos(n_i\phi_i + \delta_i)] \quad (2.10)$$

The non-bonded term describes the intermolecular interactions that include the Van Der Waals (VDW) and the coulombic interactions. VDW interaction describes the interactions between uncharged particles and is normally determined by the classical Lenard-Jones potential equation as shown in eq 2.11. The coulombic interaction describes the interactions between charged particles and could be determined by eq 2.12. The definition of parameters in eq 2.8-2.12 can be found on the LAMMPS website (https://www.lammps.org) and the value of parameters depends on the force fields the users selected.

$$V_{Lenard-Jones} = \sum_i \sum_{i \neq j} 4\varepsilon_{ij} \left[\left(\frac{\sigma_{ij}}{r_{ij}} \right)^{12} - \left(\frac{\sigma_{ij}}{r_{ij}} \right)^{6} \right] \quad (2.11)$$

$$V_{coulombic} = \sum_i \sum_{i \neq j} \frac{q_i q_j}{\varepsilon r_{ij}} \quad (2.12)$$

2.2.3 Simulation Ensembles

Three main ensembles are often used to constrain the state variables of a system in MD simulation, namely the microcanonical, canonical, and isothermal-isobaric ensembles. The microcanonical ensemble is also known as the NVE ensemble. With this ensemble, the total number of particles(N), the volume of the system(V), and the total energy of the system(E) are constant in simulation. The canonical ensemble, also known as the NVT ensemble, can be described as a system with a constant temperature during simulation via thermal energy transfer between the surroundings and the system. In the NVT ensemble, the total number of particles, the volume of the system, and the temperature of the system are constant. Isothermal-isobaric ensemble, or NPT ensemble, is a system that keeps the temperature constant via energy transfer with the surrounding. In contrast, the volume of the system can change to match the pressure exerted on the system by its surroundings. In the NPT ensemble, the number of particles, the system temperature, and the system pressure maintains constant.

2.2.4 Periodic Boundary Conditions

Periodic boundary conditions (PBC) are used in MD simulations to mitigate problems with boundary effects caused by the finite size and make the system like an infinite one. The PBC is commonly applied when users want to compute the bulk properties of a system. PBC is implemented by repeating the simulation box in all directions so that a particle moves out of the box; an imaged particle moves into the simulation box to replace

it. In other words, particles in the simulation box crossing a boundary enter back from the opposite boundary, as shown in **Figure 5**. The minimum image convention needs to be employed in PBD conditions that a given particle interacts with another particle only once, regardless of the particle itself or its image.

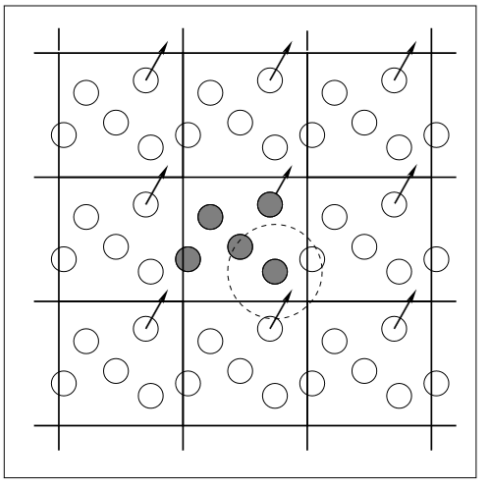

Figure 5. Schematic of particles moving out and re-entering the simulation box[91]. The black circles represent particles in the simulation box, and the white circles represent their periodic image in other unit cells.

2.2.5 Molecular Dynamics Simulation of Asphalt Materials

Molecular dynamics has become an active area of research on asphalt and a valuable tool with many papers appearing over the last 5 years[92]. Simulations became possible as chemists suggested specific examples of chemical compounds in asphalt, like the SARA fractions theory introduced before. Researchers then created representative structures to enable the application of MD to the study of asphalt.

Early work focused on asphaltenes and their aggregates to determine viscosity and viscoelastic properties. Pacheco-Sánchez *et al*.[93] used 4 structures representative of asphaltenes to investigate their orientations within aggregates. Later work on molecular

orientation by Zhang and Greenfield[94] placed asphaltenes in a more realistic environment with compounds selected for each saturate, aromatic, and asphaltene fractions. Specifically, their compounds were n-docosane (C22), 1,7-dimethynaphthalene, and either of two asphaltenes proposed by Artok *et al.*[95] or by Groezin and Mullins[96]. Building on Mullins's asphaltene molecules, Zhang and Greenfield[94] and Li and Greenfield[97] progressed from a C22-alkane and 1,7-dimethylnaphthalene model mixture with 2 asphaltenes to one containing a total of 12 representative molecules. These component systems with actual chemical structures have served as a platform to launch MD simulation studies on the properties of asphalt. One can vary composition with selected combinations of molecules from this basis set to simulate asphalts with desired SARA fractions.

Wang[98] expanded the above set with additional aromatic, resin, and asphaltene molecules. These systems provide a consistent framework for investigating the properties and performance of asphalt in different situations. For example, self-healing is of great importance as cracks evolving from microcracks can lead to the failure of pavements. Using Zhang and Greenfield's 3-component model structures and others proposed by Jennings[99], Bhasin *et al.* employed MD simulation to investigate diffusion across a microcrack and better understand self-healing in asphalt[100]. That included, for example, the effect of SARA composition on the self-healing property. Taking an unusual approach to micro-healing study, Sun *et al.* carried out MD simulations by constructing a single "average molecule" for asphalt, thereby implicitly treating asphalt as a pure compound[101]. A single structure would seem likely to fail in capturing the entropic complexity of a multicomponent system and thus be unable to capitalize well on the ability of MD to investigate the effects of temperature.

Notwithstanding, the researchers concluded that the optimal temperature range for self-healing was 40.3-48.7 ℃. MD simulation has also been used to investigate the formation of nano-aggregates of asphaltenes. Samieadel *et al*. found that nano-aggregates of a polycyclic aromatic asphaltene were reduced on the addition of undecane wax, providing possible insight into the underlying mechanism by which commercial wax products function as a warm mix asphalt additive[102]. MD has examined many other properties, including glass transition temperature, viscosity, bulk modulus, and adhesion[103, 104].

In addition to studying virgin asphalt, many groups have looked at asphalt aging with MD simulation. The sophistication of these simulations has improved as better representations of virgin asphalt with model compounds appeared. Most reports emphasize oxidation as responsible for changes in physical properties with aging, though some consider changes in SARA composition with volatilization. Ding *et al*. employed Zhang and Greenfield's 3-component model to study aging and the diffusion of the rejuvenator in RAP and virgin binders[105]. To account for aging, the number of C22 maltene molecules in the simulation was reduced, and the number of asphaltenes increased. This failed to consider the key factor of oxidation by modifying structures with oxygen atoms.

An early MD study with oxidation was carried out by Tarefder *et al*. using a system comprised of only 3 structures taken from the literature, the asphaltene of Groezin and Mullins and two resin species based on Venezuelan crude oil[106]. Saturates were not included, apparently based on the recognition that most of the oxidation is known to occur in the polar resins and asphaltenes. They investigated the glass transition temperature (Tg) with oxidation. Above Tg, asphalt is more deformable, which is interesting because some

have suggested that it is tied to low-temperature cracking. Tg can be found as a discontinuity in the rate of change of specific volume with temperature. Tarefder increased the number of oxygen atoms in the asphaltenes and resins from 0.1% to 1%, 12%, 23%, and 46.5%. They found that oxygen levels below 20% did not affect glass transition temperature and decreased with higher percentages. A shortcoming of Tarefder *et al*'s work was the absence of a description of oxidation states and functional groups present. Oxygen functionalities differ from one to the other. Interaction between molecules having more polar hydroxyl or acid groups will be substantially different from those with ketones.

Other researchers advanced the model for aged asphalt by "oxidizing" the Li-Greenfield set of 12 molecules. In these new models, investigators created sulfoxides and ketones, thereby indicating an appreciation of the known relationship of viscosity to the two functional groups[107, 108]. The placement of ketones in the design of oxidation products was guided by chemistry. In particular, Dorrence *et al*. noted the susceptibility of benzylic hydrogens to oxidation to form ketones[109] so that all secondary benzylic carbons for all structures were converted to a ketone moiety. This fits nicely with the known relative reactivity of resins and asphaltenes being much greater than that of the naphthenic aromatic and saturate fractions [37:42:7:1]. Later, Chang *et al.*[110] developed a new aged asphalt model containing more oxygen-containing functional groups such as anhydrides, polynuclear aromatics. A central feature of their aged asphalt model is consideration of oxidation chemistry and reported functional group concentrations. Its details are introduced in chapter 3. This produced a set of base molecules mixed in different combinations by several researchers to simulate different aged asphalt samples according to SARA composition.

For example, Pan and Tarefder showed oxidation resulted in greater strength of intermolecular bonds with an increase in density, viscosity, and bulk modulus[111]. Qu and colleagues performed MD with the same base set to propose correlations between micro- and macroscopic properties[112]. G. Xu *et al*. found that oxidation increased the density and viscosity while decreasing the self-diffusion coefficient of asphalt[31]. G. Xu *et al*. also conducted MD simulations of their model compounds selection to investigate the rejuvenator's diffusion into a binder with RAP species[113]. These studies help demonstrate the potential of molecular dynamics for studying aged asphalt.

2.2.6 Applications of MD in Petroleum Engineering

MD simulation has been used in different research fields in the petroleum industry. For example, the researchers employed the MD simulation to investigate the thermodynamic properties of natural gas under conditions with ultra-high temperature or ultra-high pressure that couldn't be achieved in the laboratory. In addition, due to the lack of experimental data under ultra-high temperature and ultra-high pressure conditions, the reliability of the classical equation of state cannot be validated and used to compute the properties of natural gas. Therefore, Aimoli *et al.*[114] used MD simulation to determine the viscosity, self-diffusion coefficient, and thermal conductivity of pure methane and pure carbon dioxide under an ultra-high pressure condition of 800 MPa. Jin *et al.*[1] used MD simulations to predict the densities of pure alkanes, methane-propane mixtures, methane-butane mixtures, and pure hydrogen sulfide under ultra-high temperature and ultra-high pressure conditions. With the energy consumption increase, solid mineral resources are constantly exploited, for example, lithium resource in oil/gas field brine[115]. Kumar *et al.*[116] used MD simulation to study the LiCl in water and methanol. They studied the molecular

interaction between LiCl with solvents via radial distribution function, void and neck distributions, and other properties.

Furthermore, the MD simulation has been widely used to study the gas/oil phase behavior in shale formations. The amount of adsorbed gas on the shale matrix surface and dissolved gas in the shale matrix is a significant factor in the long-term productivity of the shale reservoir. Although experimental measurements have been carried out to investigate the gas adsorption and diffusion properties in the shale matrix, they cannot detail the microscopic transport mechanism of shale gas during the gas production process. MD simulation can accurately visualize the gas adsorption/desorption and diffusion processes in the shale matrix, which is why the MD simulation has been extensively used to study shale gas in the past decade. The shale matrix contains two parts, non-organic matter (montmorillonite, illite, kaolinite, quartz, calcite, and others) and organic matter(kerogen)[117, 118], both of which have been constructed to study the adsorption/desorption, diffusion behaviors of shale gas via MD simulation.

For non-organic matter, Xiong *et al.*[119] constructed a molecular model of a quartz slit based on oxygen and silicon atoms **(**shown in **Figure 6A**) to study the methane adsorption in quartz slits. They found that the interaction force between methane molecules and the pore wall is why methane molecules could be adsorbed. The interaction force between the methane molecule and the pore wall decreases as the distance between them increases. Sharma *et al.*[120] built a montmorillonite slit model based on silicon, aluminum, oxygen, and hydrogen atoms (as shown in **Figure 6B)** to study the effects of slit width and pressure on the adsorption of methane and ethane. They found methane molecules could only form a single adsorption layer on the pore wall, while ethane could form a second

adsorption layer. When methane and ethane are mixed in the slit, the pore wall prefers to adsorb ethane than methane, but this preference decreases with pressure or pore width. Zhai *et al*.[121] studied the effect of different formation depths on methane adsorption by constructing a montmorillonite slit model. They found that increasing burial depth slightly increased the methane adsorbed in the pore wall. When the burial depth is about 5 km, methane molecules have the largest diffusion coefficient in the slit pore, so they believe that for shale gas exploitation, the most reasonable burial depth is 3-5 km. Zhang *et al*.[122] studied the competitive adsorption between methane and ethane in an illite pore model. At low pressure, the adsorption capacity of ethane on the pore wall is higher than methane on the pore wall. With the increase in pressure, the increase of methane adsorption on the pore wall is higher than the increase of ethane adsorption on the pore wall.

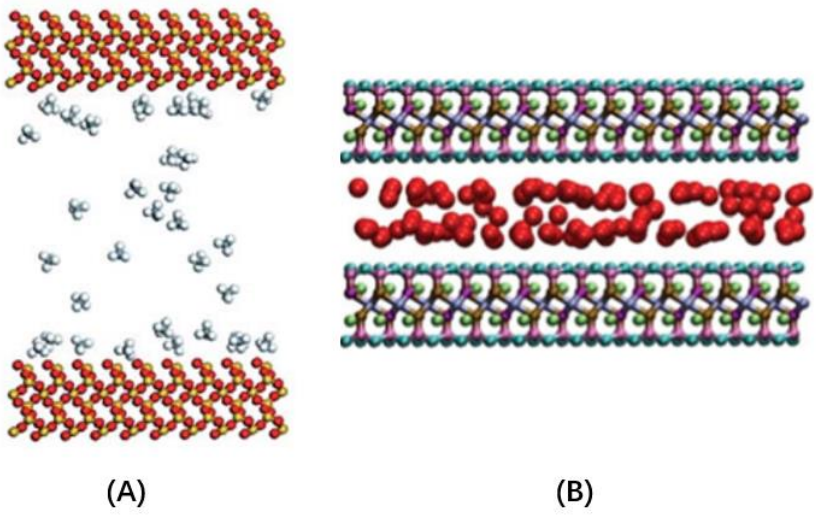

Figure 6. (A) white: methane molecules, red and yellow: quartz slit pore. (B) red: methane molecules, colorful atoms: montmorillonite slit.

The study of shale gas in organic matter can be divided into two categories via MD simulation. The first category is to construct a simple graphene slit or carbon nanotube representing organic matter; the second is to construct realistic kerogen models. Graphite slits and carbon nanotubes are mainly composed of carbon atoms. The components of the realistic kerogen model consist of carbon, hydrogen, a small amount of oxygen, sulfur, and other atoms.

To study the shale gas in slit pore structure, Yang *et al*.[123] determined the methane isotherm adsorption curve and density distribution curve in graphite slits with different widths, as shown in **Figure 7A**. By studying the adsorption capacity of methane in graphene slits with different widths (**Figure 7B**), Li *et al*.[124] found that when the width of the graphene slit is less than 2 nm, all methane molecules would be adsorbed on the slit wall. Wang *et al*.[125] studied the adsorption of shale oil with different components in slits, as shown in **Figure 7C**. They found that the number of adsorption layers of shale oil on the pore wall mainly depends on the width of the slit pore and the composition of shale oil. They found that the heavy oil components are more easily adsorbed to the pore wall. Wu *et al*.[126] simulated using the CO_2 and N_2 molecules to displace adsorbed methane molecules in the slit pore, as shown in **Figure 7D**. They found that the displacement mechanisms of these two gas molecules for methane molecules are different. CO_2 gas molecules directly occupy the position of adsorbed methane molecules on the pore wall, while N_2 gas molecules displace adsorbed methane by reducing the partial pressure of methane molecules on the pore wall.

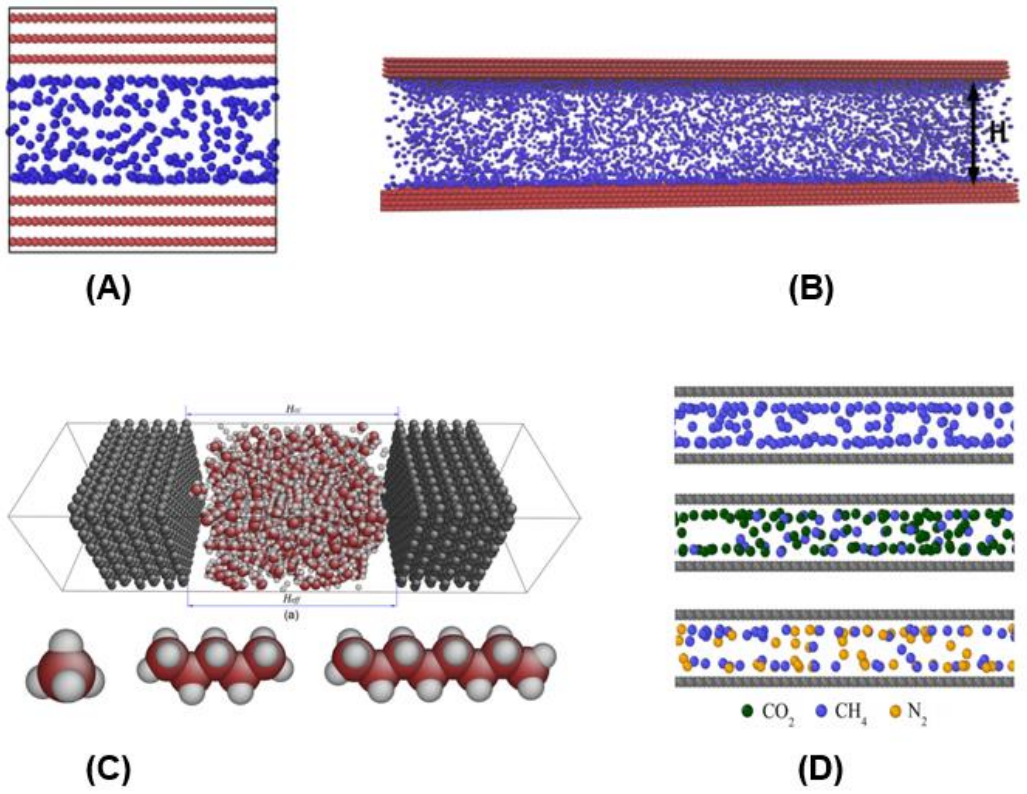

Figure 7. (A)(B) blue: methane molecules, red: slit pore. (C) black: slit pore, red: alkane molecules. (D) black: slit pore, colorful: different gas molecules.

Besides the slit models concluded above, the nanotube model has also been widely used to study the shale gas behaviors in organic matter. For example, Zhang *et al.*[127] studied the adsorption and diffusion of CO_2 and methane in carbon nanotubes at different burial depths (2-4 km), as shown in **Figure 8A**. They found that the adsorption of methane and CO_2 belonged to the physical adsorption and 2 km is the optimal depth for producing shale gas. Combining the local density theory and MD simulation, Chang et al.[128, 129] studied the local density distribution of natural gas in cylindrical shale nanopores. They found that as pressure increased, more adsorption layers of natural gas would present on the pore wall. Ohba *et al.*[130] found that the amount of methane adsorbed increased as the width of the

carbon tube decreased. In addition, they found that the methane molecules would appear as clusters in the pore with a large width (**Figure 8B**). Yuan *et al*.[131] added two layers of carbon plate on the sides of a carbon nanotube and visualized the methane displacement by CO_2 as shown in **Figure 8C**. They found that as the simulation time increased, the methane molecules were gradually displaced out of the nanotube, which could make at least 14.78% extra methane production. Zhu and Zhao[132] used a similar model shown in **Figure 8D** to study methane adsorption. They found that when the pore width was less than 1.2 nm, the amount of adsorbed methane significantly increased as the pore width increased. When the pore width was greater than 1.2 nm, the amount of adsorbed methane decreased fast as the pore width increased.

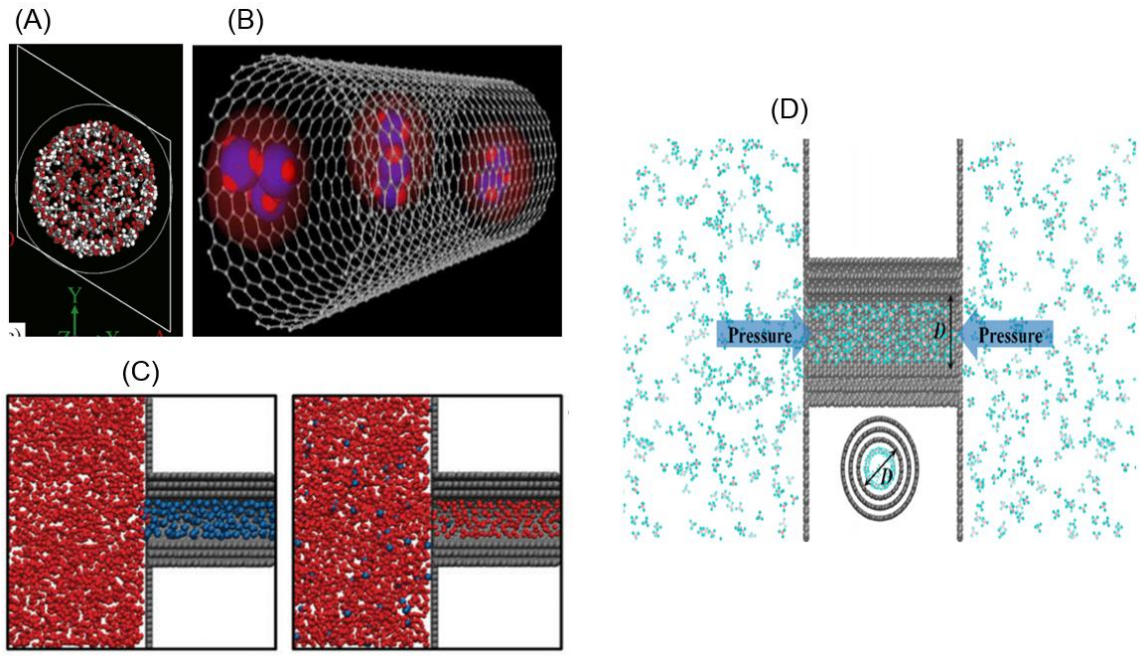

Figure 8. (A) red and white: methane and carbon dioxide molecules (B) blue and red: methane molecules (C) red: carbon dioxide molecules; dark blue: methane molecules (D) shallow blue: methane molecules.

In addition to simple slit or nanotube models, researchers developed realistic kerogen models for representing organic matter. Ungerer's group[133] developed kerogen models based on different H/C ratios, including one type-I, four type-II, and one type-III kerogen (see **Figure 9**). Their kerogen models were widely used to study the gas in the shale matrix. For example, Zhao *et al.*[134] studied the effect of water content on the adsorption of methane in II-D kerogen. The results show that kerogen was more inclined to adsorb water molecules than methane molecules. The water content on the kerogen would significantly affect the amount of methane adsorbed on the kerogen. Michalec *et al.*[135] constructed II-D the kerogen matrix to study the competitive adsorption between methane, ethane, and propane in the matrix. The results show that the kerogen is more inclined to adsorb propane molecules among the ethane and propane molecules.

The roughness of shale formation is another factor that could affect shale gas behavior. Stephane and Firoozabadi[136] used the II-A kerogen model to construct a smooth slit pore. Then, they used the different numbers of nitrogen atoms covering the slit surface to represent the different degrees of pore wall roughness. They found that the roughness had a large effect on the adsorption of methane. The high degree of roughness would largely weaken methane adsorption on the pore wall. At pressures greater than 40 atm, the methane molecules would form a second adsorption layer on the smooth slit wall, but not on the rough slit wall.

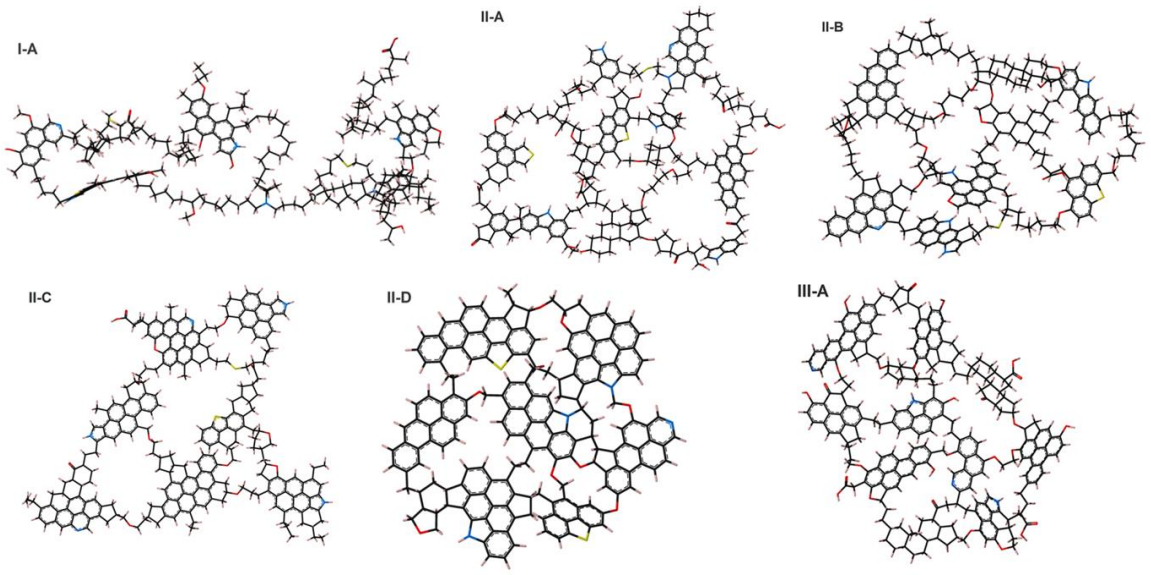

Figure 9. Six molecular models were developed for representing kerogen Type-I, II, and III from Ungerer's research group.

Similar to slit and nanotube models, researchers also studied the shale gas displacement with CO_2 injection in realistic kerogen. According to studies by Zhou *et al*.[137], Borujeni *et al*.[138], Pathak *et al*.[139], and Wang *et al*.[140, 141], it has been found that kerogens preferred to adsorb CO_2 rather than methane because of CO_2's stronger permanent quadrupole moment. However, the kerogen's preference for adsorbing CO_2 molecules would be weakened as pressure increased. However, when the pressure exceeded the critical pressure of CO_2, the preference adsorption behavior would no longer be affected as pressure increased. In addition, decreasing temperature and increasing pressure would increase the amount of gas mixture adsorbed on kerogen. Finally, if water was presented, water molecules tended to be adsorbed in the kerogen matrix and reduced methane/ CO_2 mixture adsorption in the kerogen matrix.

Chapter 3: Model Development and Study of Aged Asphalt

3.1 Introduction

Understanding the aging effect on the microstructure and macroscopic properties of asphalt provides an essential reference for its rejuvenation. In the laboratory, the microscope scanning tools, such as the atomic force microscope, transmission electron microscope, and scanning electron microscope, have been regularly utilized to study the surface microstructure of aged asphalt[142]. Yet, there are two limitations to using these scanning tools. Firstly, different processes of preparing the asphalt sample could yield different results and conflicting outcomes[143-148]. For example, Kuang *et al*.[147] found that the size and the density of "bee-structure" in asphalt increased after aging, while Zhang *et al*.[148] found that the density of "bee-structure" in asphalt decreased after aging. Secondly, there is controversy about whether the microstructure observed on the asphalt surface can represent its internal structure or not [149, 150].

Computational studies such as MD simulation can overcome some limitations of the microscope scanning tool on asphalt. In addition, MD simulation can reveal structural details, dynamic evolutions, and composition-property dependence of asphalt mixtures. The construction of an aged asphalt model that can capture the nature of real aged asphalt significantly affects the reliability of the microstructure analysis of asphalt. As shown in **Figure 10**, Greenfield and co-workers proposed virgin asphalt models of 12 representative molecules by selecting n-docosane (C22), 1,7-dimethyl naphthalene, and asphaltenes recommended by Artok *et al*.[95] and by Groezin and Mullins[95]. Later, Wang and co-workers expanded the set with more aromatic, resin, and asphaltene molecules. These molecular structures have served as a platform for investigating the properties and performance of

virgin asphalt in different situations[92, 100-104]. More importantly, one can vary composition by combinations of molecules from this basis set to simulate new experimental asphalt samples with desired SARA fractions. Six functional groups have been identified as the product during asphalt oxidation. These include ketones, sulfoxides, anhydrides, carboxylic acids, alcohols, and polynuclear aromatics[34, 151]. Therefore, Xu *el al*.[31], Pan and Tarefder[111] added ketone and sulfoxide functional groups on the asphalt molecules to represent aged asphalt molecules. M. Xu *et al.* [152] recently developed an oxidized asphalt model to include alcohols and ketones. Xu *et al*., Pan and Tarefder used their aged asphalt models to study the effect of aging on the physical, and rheological properties of asphalt, such as viscosity, self-diffusion, and moisture resistance.

However, there are some issues with the aforementioned aged models. At first, the absence of other oxygen-containing functional groups is a limitation, such as anhydrides, carboxylic acids, and polynuclear aromatics. Second, one of the structures resulting from simply converting all secondary benzylic carbons to ketone without considering organic chemistry[31, 111] should be revised. The diketone structure of their oxidized asphaltene-pyrrole is doubtful since oxidation of the first ketone will almost certainly cause the conversion to the phenol tautomer with the favorable formation of an aromatic ring. Therefore, in this chapter, a new aged asphalt model is developed and used to study the effect of aging on the properties of asphalt.

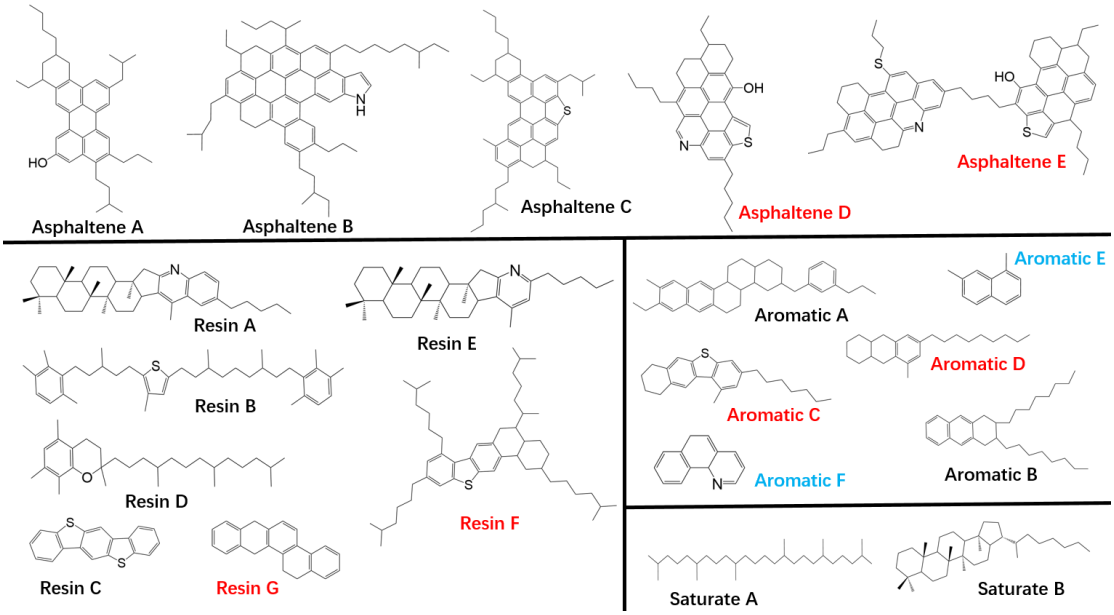

Figure 10. Virgin asphalt model and its composition molecules: Li and Greenfile[97] (black); Zhang and Greenfield[94] (blue); Wang *et al.* [98] (red).

3.2 New Model Development

The principles used to construct the oxidized asphalt model are introduced below. In general, like in the previous studies[31, 111], the functional groups are added to the right sites on the virgin asphalt molecule to represent its oxidation. From Petersen's scheme[153], asphalts oxidize in two phases, a fast reaction and a slow reaction. The fast reaction phase involves the aromatization of polycyclic structures like resin G (**Figure 10**) with byproduct hydrogen peroxide or other peroxide intermediates acting to oxidize thioethers to sulfoxides. The slow reaction phase proceeds through forming the hydroperoxide of tertiary benzylic species, which can yield ketone and alcohol or benzylic alcohol and other oxidation products such as sulfoxide. While this is correct, the literature indicates that ketone is a minor product. The thermal free radical decomposition of the tertiary benzylic hydroperoxide formed from cumene yields over 80% of the alcohol product. Therefore, the

tertiary benzylic sites in Aromatic A, Resin E, Resin F, and Asphaltenes A-E (**Figure 10**) are converted to alcohol. Most of these sites exist in the resin and asphaltene fractions in line with the fact that they have a much higher susceptibility to oxidation than the aromatic fraction.

Dorrence *et al*. found strong evidence for oxidation yielding ketones at the benzylic position[109]. In addition, it was noted that the ketone products are mainly from the slow phase degradation of the tertiary benzylic hydroperoxide. This is because the hydroperoxide degradation mainly yields the alcohols, not the ketones. Thus, in this chapter, the ketone moieties were only created from the secondary benzylic carbon molecules of the virgin asphalt molecules. The secondary benzylic sites on the asphaltenes and resins were the first choice since the asphaltene and resin fractions are highly susceptible to oxidation. Then some of the sites on the aromatics were selected. To account for ketones, the secondary benzylic carbon sites were converted in these molecules: Aromatics A and C, Resins A, B, E, and F, and Asphaltenes A, B, D, and E.

Primary benzylic carbons in the virgin asphalt model offer a site for carboxylic acids and anhydrides. A methyl substituent with benzylic hydrogens on an aromatic ring can be oxidized to the aldehyde and a carboxylic acid group. Aldehydes in the air are readily converted to the corresponding carboxylic acid. Hence an aryl methyl group or primary benzylic carbon on Aromatic A was envisioned as being oxidized to the aldehyde. Adjacent aryl methyl structure on Resins B and D created sites for the anhydride moiety reported for aged asphalt.

Thioethers and thiophenes (Aromatic C, Resins B, C, F, and Asphaltenes C, D, F) were oxidized to sulfoxide. Asphalt contains multiring molecules with both aromatic and aliphatic portions (Resin G) that can be oxidized to a polynuclear aromatic species.

The newly developed aged asphalt model contains 14 oxidized asphalt structures, as shown in **Figure 11**.

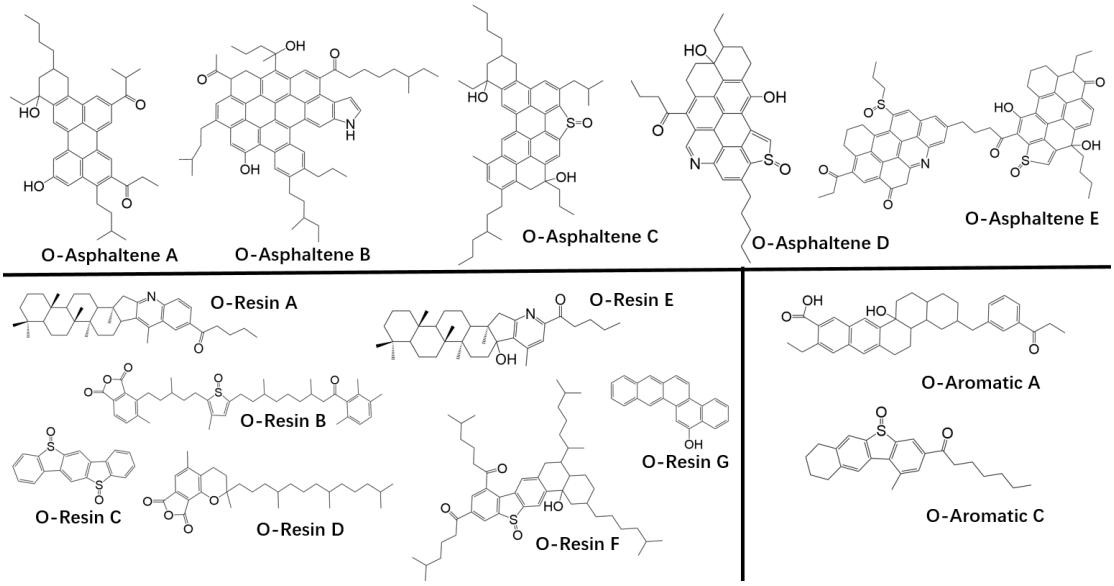

Figure 11. Representative molecules for oxidized asphaltene, resin, and aromatic in newly developed aged asphalt model.

At 1 atm and 404 K, Petersen and coworkers[34] reported the functional group concentrations from four aged asphalt samples (approximately 5 years service time) taken from widely disparate sources. Values were nominally 0.60 mol/l ketone, 0.27 mol/l sulfoxide, 0.023 mol/l anhydride, and 0.0068 mol/l carboxylic acid. No data was reported about the level of alcohol moiety. However, based on details in the dual oxidation mechanism, it was expected to be in the same order as the sulfoxide. By adjusting the number of virgin and aged asphalt molecules from **Figure 10** and **Figure 11**, an aged asphalt model was constructed and named it Model-1. The composition of Model-1 is

provided in **Table 1**, with the SARA mass fraction of 17% saturates, 36% aromatics, 33% resins, and 14% asphaltenes. At 1 atm and 404 K, Model-1 has concentrations of 0.60, 0.28, 0.38, 0.027, and 0.0090 mol/l for ketone, sulfoxide, alcohol, anhydride, and carboxylic acid, respectively. These functional group concentrations agree with the ones that Peterson's study reported. **Figure 12** shows the initial configuration of Model-1 in MD simulation. In addition, By removing all the oxygen-containing functional groups in Model-1, a virgin asphalt model was constructed to represent the virgin state of Model-1 and named Model-0.

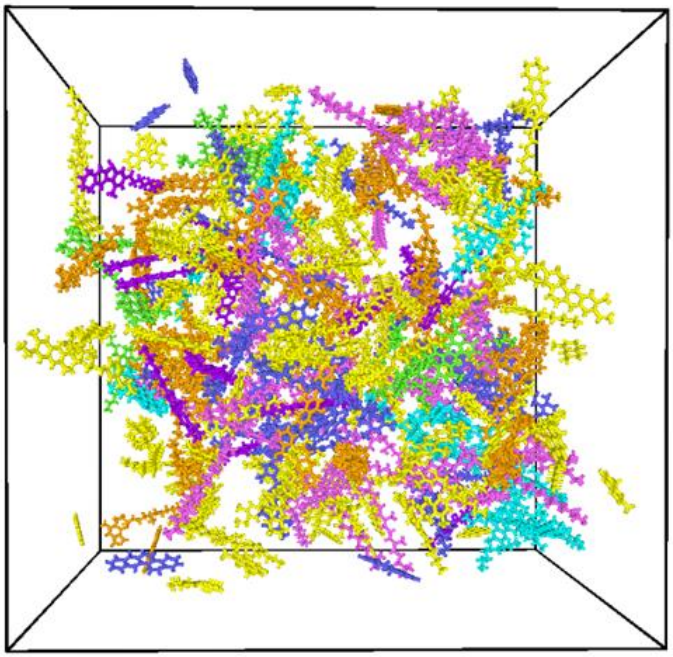

Figure 12. Initial configuration of Model-1: blue, virgin asphaltenes; purple, virgin resins; yellow, virgin aromatics; light pink, saturates; green, aged asphaltenes; orange, aged resins; dark pink, aged aromatics.

Table 1. SARA compositions of aged asphalt model

Saturates	Asphaltenes	O-Asphaltenes	Resins	O-Resins	Aromatics	O-Aromatics
A 17	A 2	A 2	A 3	A 14	A 16	A 1
B 24	B 4	B 2	B 8	B 2	B 17	
	C 4	C 1	C 3	C 2	C 19	C 14
	D 1	D 2	D 4	D 1	D 20	
	E 1	E 1	E 4	E 9	E 21	
			F 5	F 6	F 18	
			G 2	G 7		

3.3 Simulation Details

The OPLS-AA force field has successfully described interactions of asphalt systems[97 94, 104, 154, 155], and thus is adopted in this research. The force field parameters are available from publications of Li and Greenfield, Sun and Wang, and Jorgensen *et al.* [97, 154, 156-159]. For those newly developed aged asphalt molecules, those alcohol, ketone, and sulfoxide functional groups are also described by the OPLA-AA force field. The force field parameters of anhydride and carboxylic acid functional groups were referenced to the work of Ponnichamy[160] and Kamath[161], respectively.

All simulations were performed using a large-scale atomic/molecular massively parallel simulator (LAMMPS, 3 Mar 2020 version). The molecules were randomly placed in a cubic simulation box with a length of 10 nm via the PACKMOL software. Periodic boundary conditions were applied in X, Y, and Z directions. A cutoff of 1.5 nm was set for the non-bonded interaction, while the long-range electrostatic interaction was calculated by the PPPM method. The time steps from 0.1 to 1.0 fs were used at different simulation stages. For Model-0 and Model-1, an entire trajectory of 40 ns has been collected at the

NPT ensemble, with a time step of 1 fs, under 298 K/404 K and 1 atm. Several physical properties of Model-1 were computed, and compared their values with other aged asphalt samples from published papers at 298 K for model validation. The RDFs, shear viscosity and self-diffusion of Model-1 and Model-0 were determined to study the aging effect on the macroscopic properties of asphalt at 404 K.

3.4 Computational Properties of Asphalt

This chapter concludes all the asphalt properties computed for research. All of them are calculated directly or indirectly based on the different output data from MD simulations.

3.4.1 Radial Distribution Function

The radial distribution function (RDF) can be an important measure of the microstructure of asphalt because it can indicate how molecules are packed together. In other words, it can be used to analyze the molecular interaction between molecules in the asphalt. The RDF defines the normalized probability of finding a particle at a distance r away from another particle, which is expressed as:

$$g(r) = \lim_{dr \to 0} \frac{\rho(r)}{4\pi \rho_{bulk} r^2 dr} \tag{3.1}$$

In eq 3.1, $g(r)$ is the RDF, $\rho(r)$ is the average number of particle pairs located between distance r and $r + dr$, and ρ_{bulk} represents the bulk density of particle pairs in the simulation box.

3.4.2 Viscosity

Several methods have been developed to computationally determine the shear viscosity of a fluid in MD simulation. They fall into equilibrium molecular dynamics (EMD) and nonequilibrium dynamics (NEMD). Green-Kubo (GK) method is the most

widely used EMD method that results from a pressure-tensor autocorrelation calculation. The SLLOD algorithm is the typical NEMD method in which shear viscosity is determined from the ratio of the shear stress to the velocity gradient. This chapter employed EMD-GK and NEMD-SLLOD to determine the shear viscosity of asphalt models.

In the EMD-GK method, the shear viscosity is determined through the integral of the pressure-tensor autocorrelation function over a correlation length[162],

$$\mu = \frac{V}{kT}\int_0^\infty < P_{ij}^S(0)P_{ij}^S(t) > dt \tag{3.2}$$

Where P_{ij}^S is the off-diagonal pressure tensor of element ij, V is the volume of the system, T is the temperature, k is the Boltzmann constant, t is the time, and the angle bracket means the ensemble average. From the EMD-GK equation, theoretically, the pressure-tensor autocorrelation function (ACF) will converge and decay to zero in the long-time limit (long correlation length), and its integral will achieve a plateau or be a constant value that corresponds to the predicted shear viscosity.

NEMD-SLLOD method could avoid the high computational cost associated with the EMD method.[163, 164] With the SLLOD method, the shear viscosity is estimated by imposing a Couette flow to the fluid. A shear field is specified to manipulate the boundary of the simulation system and measure the shear viscosity via the off-diagonal component of the pressure or stress tensors. The fundamental equation of the SLLOD method is:

$$\mu(\dot{r}) = -\frac{P_{ij}}{\dot{r}} \tag{3.3}$$

where P_{ij} is an off-diagonal component of the stress tensor, and $\dot{r}$ is the applied shear rate. i is the flow direction induced by the imposed shear, whereas j is the direction normal to the flow direction.

3.4.3 Self-diffusion Coefficient

The self-diffusion coefficient of asphalt can be derived from its mean-squared displacement (MSD). MSD normally is used to indicate the translation mobility [31] and its' generic formula is as follows:

$$MSD(t) = < |r_i(t) - r_i(0)|^2 > \tag{3.4}$$

Where $r_i(t)$ is the position of particle i at time t, $r_i(0)$ is the position of particle i at the initial time (t=0) and the angular bracket represents the ensemble average. The self-diffusion coefficient(D) with Fickian diffusion can be derived from the MSD via the equation:

$$D = \lim_{t\to\infty} \frac{1}{6t} MSD(t) \tag{3.5}$$

3.4.4 Cohesive Energy Density and Solubility Parameter

The cohesive energy density (CED) equals the mutual attractiveness of all molecules in the asphalt per unit volume[154], which can be determined through the equation below. The solubility parameter is defined as the square root of CED. It assesses the degree of attractive interaction between molecules inside the asphalt.

$$CED = \frac{E_{intra} - E_{total}}{V} \tag{3.6}$$

Where E_{intra} and E_{total} are the intramolecular energy and total energy of the asphalt at its equilibrium state at a specified condition.

3.4.5 Surface Free Energy

Surface free energy (SFE) describes the work needed to extract the molecules from the bulk asphalt to form a new area of the surface. At the macroscopic level, SFE reflects the ability of the asphalt to crack and form a new surface[165]. The larger SFE indicates the increased brittleness of the asphalt[166]. The SFE is determined through the equation below[166].

$$r_a=(E_{confined}-E_{bulk})/2A \tag{3.7}$$

Where r_a is the SFE, $E_{confined}$ and E_{bulk} are the potential energy of the asphalt confined and bulk models at specified conditions (as shown in the figure below). A is the area of the surface perpendicular to the Z direction in the confined model.

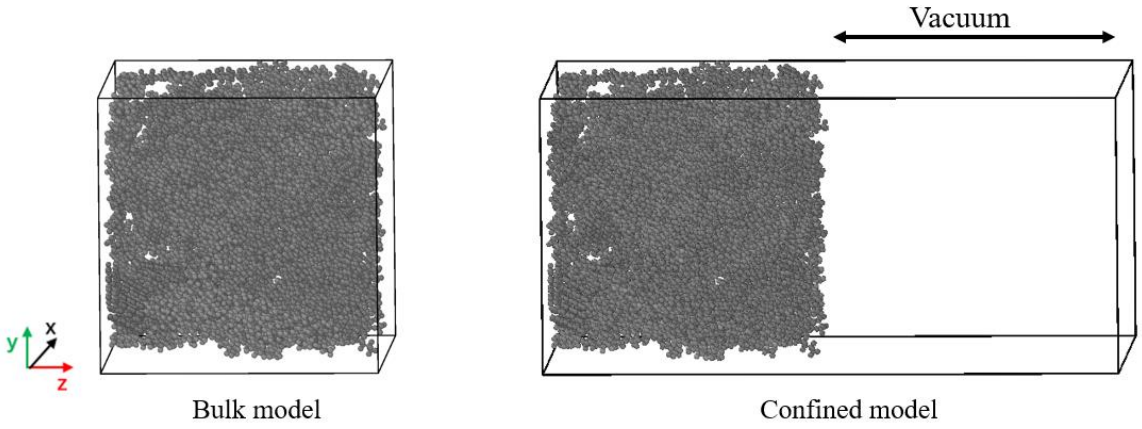

Figure 13. The example of bulk and confined models of asphalt in MD simulation. Black: asphalt molecules.

3.4.6 Mechanical Properties

Bulk modulus(K) defines the ability of a material to resist uniform compression, which is the basic property of asphalt. In this dissertation, the bulk modulus is computed as the quotient of the normal stress to the volumetric strain of asphalt. The generic equations are shown below:

$$\varepsilon_{xx} = \varepsilon_{yy} = \varepsilon_{zz} = \pm 0.005 \tag{3.8}$$

$$\Delta = \varepsilon_{xx} + \varepsilon_{yy} + \varepsilon_{zz} \tag{3.9}$$

$$\sigma_{average} = \frac{1}{3}(\varepsilon_{xx} + \varepsilon_{yy} + \varepsilon_{zz}) \tag{3.10}$$

$$K = \frac{\sigma_{average}}{\Delta} \tag{3.11}$$

ε is the strain in all three directions, σ is the normal stress applied in the three directions. K is the bulk modulus.

Shear modulus(G) is the ratio of shear stress to shear strain, which characterizes the ability of materials to resist shear strain. The shear modulus of asphalt can be related to the field performance of asphalt pavement. The equations for computing the shear modulus of asphalt are:

$$G = \frac{\tau_{xy}}{r_{xy}}, r_{xy} = \pm 0.005 \tag{3.12}$$

Where G is the shear modulus, τ_{xy} is the shear stress applied on the simulation box through the X-Y direction and r_{xy} is the shear strain in the X-Y direction.

Poisson's ratio is used to measure the "Poisson effect" which describes the deformation of a material in directions perpendicular to the direction of pressure loading. The Poisson's ratio (v) of asphalt is determined by using its bulk and shear modulus:

$$v = \frac{3K - 2G}{6K + 2G} \tag{3.13}$$

3.4.7 Glass Transition Temperature

Asphalt is a temperature-sensitive material. As the temperature increases, the behaviors of the asphalt can be divided into three stages, Newtonian-flow state, viscoelastic state, and vitrification state. The Tg is the temperature when the asphalt changes from the viscoelastic state to the vitrification state. At the macroscopic level, the glass transition process defines a reversible change of asphalt from a rubbery state to a brittle glass state, which significantly affects the properties of asphalt. The glass transition temperature can be determined at the intersection where two asymptotes intersect in the curve of the specific volume of asphalt versus the temperature[103]. **Figure *14*** shows a Tg value determined for Model-1.

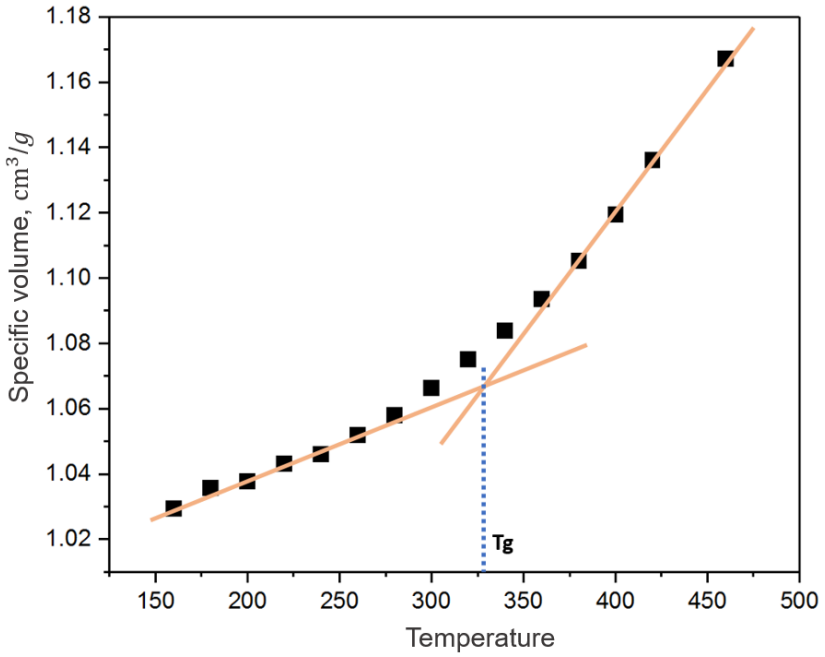

Figure 14. The specific volume of Model-1 at different temperatures. The Tg value could be determined at the intersection as shown in the figure.

3.4.8 Density

The density is an important and basic property of asphalt. In MD simulation, it can be determined through:

$$\rho = \frac{N_m MW}{N_A V} \tag{3.14}$$

Where N_m is the number of molecules in the asphalt, MW is the molecular weight of the molecule, V is the volume of asphalt, and N_A is Avogadro's number.

3.4.9 Adhesion Between Asphalt and Aggregate

The adhesion energy (E_adhesion) can be used to quantify the bonding strength between the asphalt and aggregate. The bonding strength between the asphalt and aggregate significantly relates to the resistance of the asphalt mixture to fracture-related failure behavior and durability[167]. Silicon dioxide (SiO_2) is one of the most common components in mineral aggregates. Therefore, the SiO_2 molecule was used to build the aggregate. One unit cell of SiO_2 is shown in the figure below, which has lattice parameters of a = b = 4.913Å, c = 5.405 Å, α= β=90°, and γ=120°. A single unit cell of SiO_2 was first cleaved in the [0,0,1] direction and then followed by a geometry transformation for making α= β=γ=90°. Finally, by repeating the single unit cell in x, y, and z directions(supercell), a three-layers aggregate with the same length and width as the equilibrium vacuum asphalt model was constructed as shown in **Figure 16(b)**.

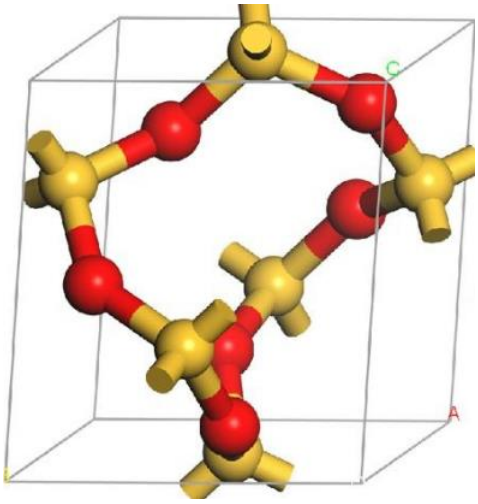

Figure 15. A single unit cell of SiO_2, red: oxygen atom, brown: silicon atom.

The $E_{adhesion}$ was determined through the equations shown below.

$$E_{adhesion} = E_{total} - (E_{asphalt\_vaccum} + E_{aggregate}) \tag{3.15}$$

$$W_{adhesion} = \Delta E_{interface}/A \tag{3.16}$$

where $E_{adhesion}$ is the adhesive interaction energy between asphalt and aggregate; E_{total} is the total potential energy of asphalt/aggregate system at equilibrium state with 298 K as shown in **Figure 16(c)**; $E_{asphalt\_vaccum}$ and $E_{aggregate}$ are the potential energies of asphalt and aggregate separately in the vacuum at the equilibrium state with 298 K as shown in **Figure 16(a,b)**; A is the area of interface between the asphalt and aggregate. $W_{adhesion}$ is the adhesion energy per unit area of the interface.

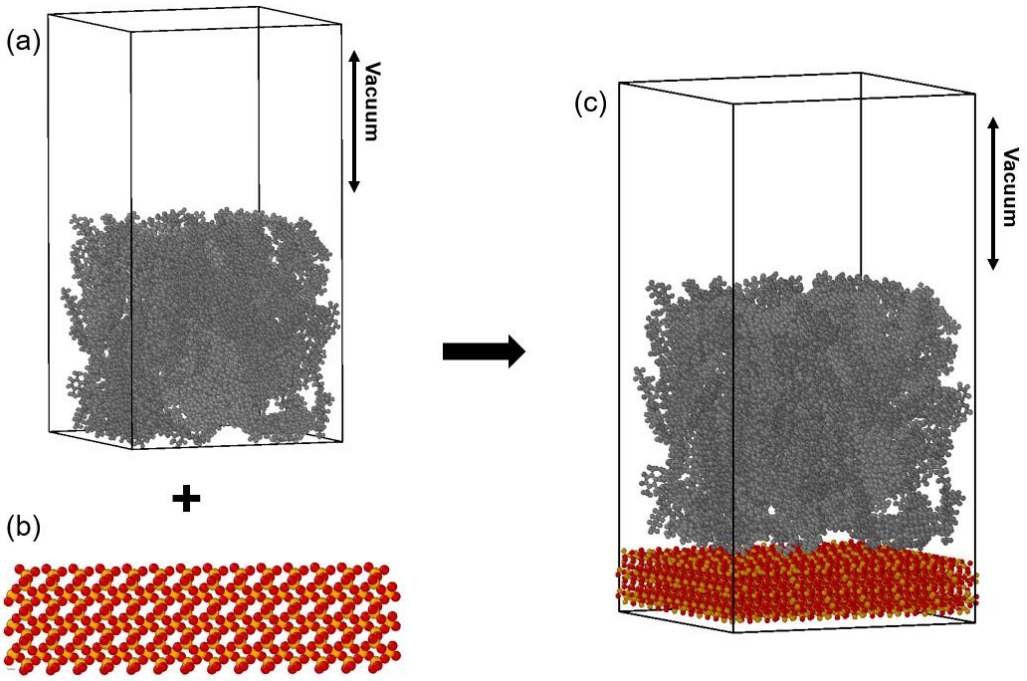

Figure 16. (a) vacuum asphalt system, (b) SiO_2 aggregate, (c) asphalt/ SiO_2 aggregate system. Red: oxygen atom, brown: silicon atom, black: asphalt molecules.

3.5 Results and Discussions

3.5.1 New Model Validation

Several physical properties of Model-1 were calculated to compare with available reports and further validate the model development of oxidized components. The results are provided in **Table 2**. All properties were calculated at 298 K, the same temperature as the references.

Table 2 shows that satisfactory agreements have been achieved for all properties. In addition, at 1 atm and 403.15 K (130 °C), Petersen and coworkers[34] reported the functional group concentrations of real aged asphalt models. Average values were nominally 0.60 mol/l ketone, 0.27 mol/l sulfoxide, 0.023 mol/l anhydride, and 0.0068 mol/l carboxylic acid. The functional group concentrations of Model-1 at 404 K were calculated

and the values were 0.55 mol/l ketone, 0.26 mol/l sulfoxide, 0.025 mol/l anhydride, and 0.0083 mol/l carboxylic acids, which are consistent with the reported values by Petersen.

Table 2. Properties of Model-1 at 298 K and 1 atm.

Calculated Property	**This work**	**References**
Density, g/cm^3	0.94	0.95-1.08[31, 112, 168, 169]
Self-diffusion,$\times 10^{-9}$ cm^2/s	4.5	2.0-6.0[170]
Surface free energy, mJ/m^2	87	30-79[31, 171, 172]
Cohesive energy density, $\times 10^8$ J/m^3	3.7	3.2-4.0[165, 168, 171, 173, 174]
Bulk modulus, GPa	4.5	4.3[174]
Shear modulus, GPa	1.1	0.7[174]
Poisson's ratio	0.38	0.20-0.50[175-177]
Adhesion of asphalt/quartz, mJ/m^2	88.24	23.31-100.6[168, 173, 178]
Glass transition temperature	317.5	267.06-350.5[168, 169, 179]
Solubility, $(\mathrm{J/cm^3})^{1/2}$	19.2	18.1-19.5[154, 169, 171]

3.5.2 Self-diffusion and Viscosity

Viscosity and self-diffusion are two particularly important properties of asphalt. The viscosity of asphalt affects aggregate coating at the hot mix asphalt plant and compaction at the site of lay down. Separately, molecular self-diffusion across the crack interface is one of the healing mechanisms of asphalt. The aging of asphalt increases its viscosity and decreases its self-diffusion, which makes the asphalt crack easily and reduces its self-healing rate.

The self-diffusion coefficient and viscosity are calculated under 404 K and 1 atm, which is a condition for asphalt compaction on the road. The EMD-GK method was first used to determine the zero-shear viscosity of Model-1. Two parameters in the GK method significantly affect the accuracy of the predicted shear viscosity value. They are sample

interval and correlation length. The sample interval should be relatively small, so pressure tensor components can be written out frequently enough and accurately estimate the time integral[180]. Based on suggestions from Maginn's study[180], the sample interval was set as 10 fs. The correlation length should be long enough to achieve the integral plateau of ACF. A correlation length of 500 ps was used to determine the zero-shear viscosity of Model-1 at first upon three independent cases. The integral of ACFs is shown in **Figure 17A**. It is not clear that the convergence plateau region shows up in the ACF integral of all cases. The ACF integrals of case 2, case 3 and average case look like almost reaching their plateau region. In **Figure 17B**, the correlation length was increased from 500 ps to 2000 ps. It can be observed that only ACF integral of case 2 has a clear plateau region and other 2 cases still need a long time to converge.

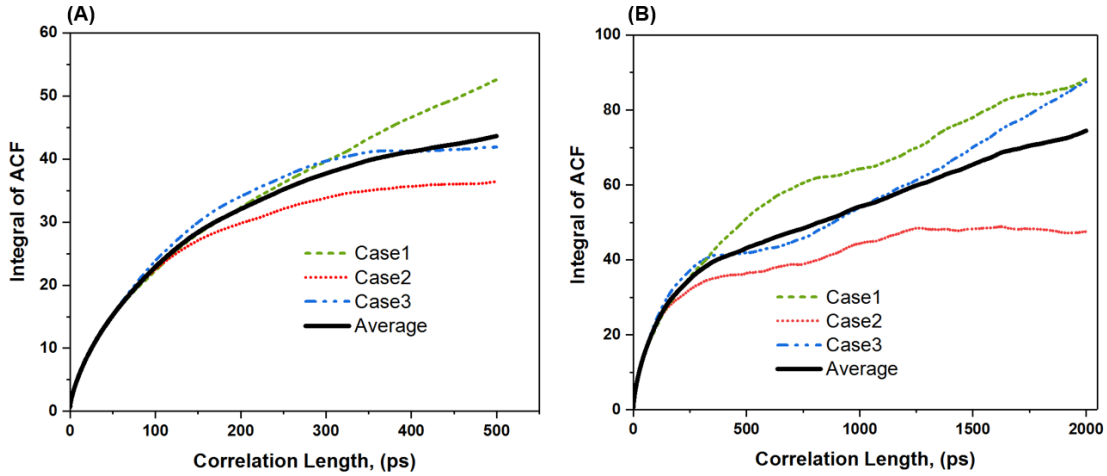

Figure 17. Integral of ACF of three independent cases and their average case. (A) 500 ps correlation length (B) 2000 correlation length.

Van-Oanh *et al.*[181] found that the viscosity convergence plateau can be reached only if the correlation length is much longer than the relaxation time of the system. The asphalt

system consists of complex and heavy molecular-weight molecules so its relaxation time is quite long, especially under low-temperature conditions. Zhang and Greenfield[182] found the relaxation time of their asphalt system is about 7.5×10^3 ns at 358.15 K and about 0.24 ns at 443.15 K. I didn't calculate the relaxation time of my asphalt models. However, I believed it should be longer than the relaxation time of Zhang's asphalt system because the asphalt models developed in this research are much more complex than Zhang's asphalt model. It is necessary to significantly increase the correlation length for having a reliable viscosity result, but this will largely increase the computational cost. Hence, due to the high computational cost of using the EMD-GK method, the GK method was finally abandoned in this dissertation to determine the shear viscosity of asphalt models. The final result of the shear viscosity of Model-1 via the GK method is not reported since it is unreliable.

The NEMD-SLLOD method could avoid the high computational cost associated with the EMD-GK method. Fallah *et al.*[183] and Lemarchand *et al.*[184] found that by using the SLLOD method to determine the shear viscosity of the asphalt, the low shear rate might result in an inaccurate viscosity result. Therefore, for the shear rate lower than < 1E8 (1/s), its shear viscosity value was averaged over 20 independent cases. For the shear rate between 1E8 and 1E9 (1/s), its shear viscosity value was averaged over 10 independent cases. For the shear rate larger than 1E9(1/s), its shear viscosity value was averaged over 5 independent cases. The shear viscosities of Model-0 and Model-1 versus shear rates are shown in **Figure 18(A)**. The MSDs of Model-0 and Model-1 are shown in **Figure 18(B)**, and the corresponding self-diffusion coefficients are 6.79E-07, and 2.81E-07 (cm^2/s). It is clear that the oxidation of asphalt decreases its self-diffusion coefficient and increases its viscosity. These findings are consistent with the previous studies[31, 185].

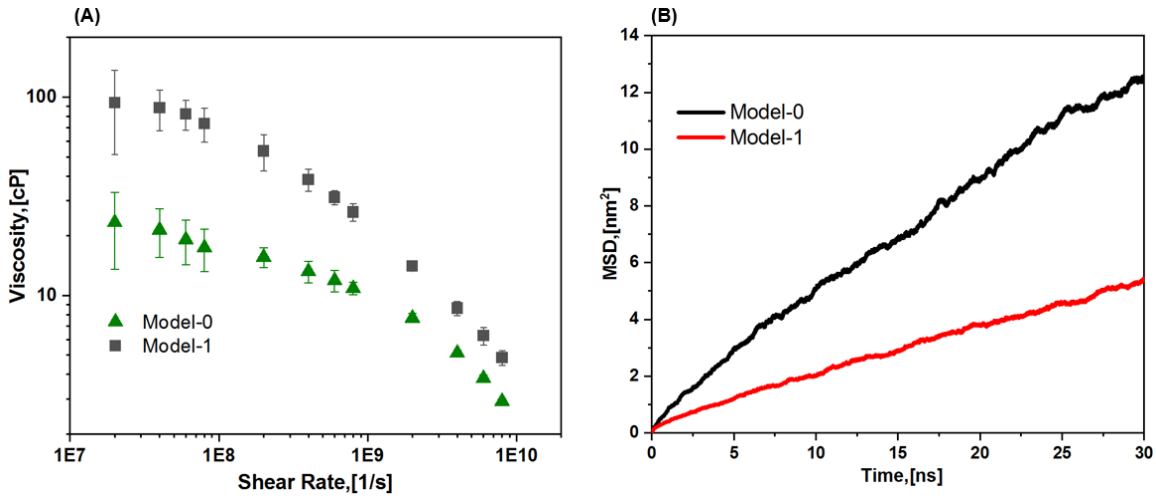

Figure 18. (A) shear viscosity versus the shear rate of Model-0 and Model-1. (B) MSDs of Model-0 and Model-1.

3.5.3 Radial Distribution Function

Asphaltene is the most viscous and polar component in asphalt, and significantly affects the rheological properties of asphalt. Thus, I mainly focused on analyzing the molecular interaction between asphaltenes with themselves and asphaltenes with the other three fractions to understand the aging effect on the microstructure of asphalt. MD simulations were conducted for another 30 ns at the NPT ensemble after the first 40 ns to generate 3000 trajectory files for RDF analysis. In every trajectory file, the position of the center atom in each molecule was used to determine RDFs.

The RDFs of asphaltene-SARA fractions in Model-1 and Model-0 are shown in **Figure 19**. In Model-0, the RDF of the asphaltene-asphaltene pair has the largest peak at r, around 4.5 Å than the RDFs of asphaltene with the other three fractions, indicating the strong preferential molecular interaction between asphaltene-asphaltene molecules. The large molecular interactions between asphaltene molecules form the asphaltene aggregations in the asphalt model, which is why the g(r) value at the first peak is larger

than 1. In addition, the RDF of the asphaltene-resin pair also has an obvious peak at r around 4.5, larger than 1 but much smaller than it of the asphaltene-asphaltene pair. This means the aggregations also formed between asphaltenes and resins, but the aggregation strength is much smaller than that formed between asphaltenes-asphaltenes. The RDFs of asphaltene-aromatic and asphaltene-saturate have no peak versus distance, indicating that the aromatic and saturate molecules distribute homogeneously around asphaltenes in asphalt. The asphaltene and resin are two fractions with large polarity in asphalt. I believe this is why the interactions between these two fractions are stronger than those between the other two fractions with asphaltenes.

In Model-1, a notable observation is that the first peak of asphaltene-asphaltene RDF significantly increased, indicating that oxidation could enhance the molecular interaction between asphaltenes. It also means the oxidation could significantly enhance the aggregations formed between asphaltenes in asphalt, which is consistent with the results reported by Kuang *et al*.[147] Such stronger asphaltene aggregations form the larger and heavier asphaltene clusters in asphalt and thus increase the viscosity and decrease the self-diffusion coefficient of asphalt after oxidation.

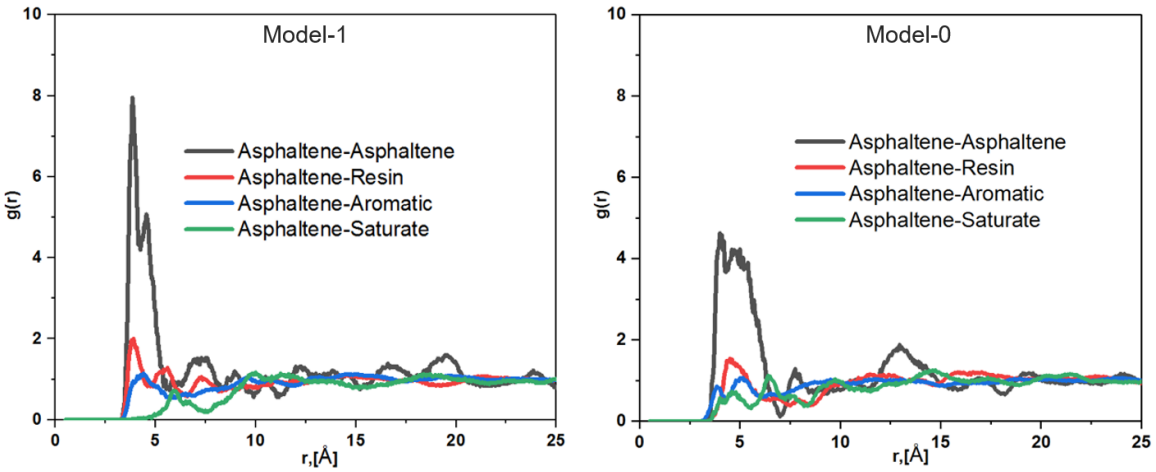

Figure 19. RDFs of asphaltenes with SARA fractions in Model-0 and Model-1.

3.6 Conclusions

In this chapter, a new aged asphalt model is constructed. The improvements regarding the new aged asphalt model include: (1) The new aged asphalt model covers all the oxygen-containing functional groups. The functional groups such as anhydride, carboxylic acid, and polynuclear aromatic should also be considered since they may be important in affecting the asphalt properties[31]. (2) The placement of some ketones in the new model was revised based on chemistry. (3) The realistic aged asphalt model is validated and can successfully capture the nature of real-aged asphalt. By analyzing the shear viscosity, self-diffusion coefficient, molecular interaction, and microstructure of asphalt before and after oxidation, I believe the stronger aggregations formed between asphaltenes due to oxidation are why asphalt has a change in viscosity and self-diffusion coefficient after oxidation.

Chapter 4: A Study of Waste Cooking Oil/Aged Asphalt Mixture

4.1 Introduction

Several papers have been published for studying the effect of WCO on viscosity, self-diffusion, and other properties of asphalt via experiments and MD simulations. Zargar *et al*.[51] used a WCO consisting of palmitic, oleic, and linoleic acid to rejuvenate the aged asphalt. They found that applying 4 wt% of WCO could restore the viscosity of 40/50 aged asphalt to its original state at 408.15 K. Ji and co-workers[52] used waste corn and soybean oil to modify the properties of aged asphalt. They reported that the viscosity of the aged asphalt decreased as the WCO ratio increased and that the addition of 6 wt% of WCO could restore the viscosity of the aged asphalt to that of the virgin asphalt. Sonibare *et al*. reported their MD simulation results that adding WCO would reduce viscosity and increase the self-diffusion of virgin asphalt. In addition, their radial distribution function analysis revealed that components of asphalt interacted more homogeneously due to the addition of WCO[186]. Li *et al*. [174] increased the virgin asphaltene fraction to form an aged asphalt model with the virgin asphalt components. By introducing the 6%,9%, and 12% (by the weight of asphalt sample) WCO that consisted of hexadecenoic, linolenic, oleic, and stearic acids, into the aged asphalt model at 1 atm and 298 K, their simulation result found the WCO reduced the viscosity and increased the cohesive energy density of aged asphalt. Xin *et al.* used the triglyceride as the WCO mixing with a virgin asphalt model at 1 atm and 413 K[187]. Unlike the observation of the CED result from Li's study, the simulation result from Xin's study found the WCO decreased the CED of virgin asphalt, indicating the intermolecular interaction between the asphalt molecules was weakened by the WCO. Xin *et al* thought

TG molecule has three long flexible molecular branches, which result in a weak intermolecular interaction between asphalt molecules and viscosity reduction.

However, neither experimental nor simulation studies could show how the WCO affects the viscosity and self-diffusion of aged asphalt. Therefore, in this chapter, the rejuvenation mechanism of WCO on viscosity and self-diffusion of aged asphalt is revealed by studying the molecular interaction between aged asphalt and WCO.

4.2 Models and Simulation Details

In addition to virgin and aged asphalt models constructed in chapter 3, a WCO-modified asphalt model (named Model-2) is constructed in this chapter. Triglyceride, the main component of WCO, is an ester derived from glycerol and fatty acids. It was adopted to represent the WCO in this chapter. The molecular structure of TG is shown in **Figure 20**. 12 triglyceride molecules, corresponding to about 10 wt% of the aged asphalt model, are added to construct the TG/aged asphalt mixture (Model-2). It was noted that 10 wt% of WCO is commonly used in asphalt experiments,[188-190] and that other mass ratios of TG have not been investigated in this chapter. It was also noted that the bulk TG density at 353 K and 1 bar was calculated to be 0.889 g/cm^3, which agrees well with available experimental (0.856) and computational (0.885) studies.

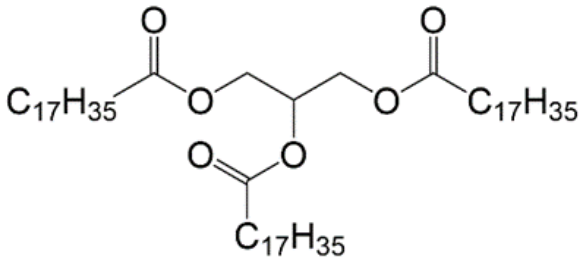

Figure 20. Molecular structure of single TG molecule.

The force field parameters for all asphalt molecules have been mentioned in chapter 3. For TG molecules, the force field parameters were taken from the work of Paulina *et al.* [191]. As suggested by experiments[44, 192-195], the temperature of blending the WCO with virgin/aged asphalts varies from 403 to 433 K. Thus, the Model-0, Model-1, and Model-2 were simulated at 404 K and 1 atm in this chapter. At the initial condition of the simulation, the molecules were randomly placed in a cubic simulation box with a length of 10 nm via the PACKMOL software. Periodic boundary conditions were applied in X, Y, and Z directions. A cutoff of 1.5 nm was set for the non-bonded interaction, while the long-range electrostatic interaction was calculated by the PPPM method. The time steps from 0.1 to 1.0 fs were used at different simulation stages. For each asphalt model, an entire trajectory of 40 ns has been collected at the NPT ensemble, with a time step of 1 fs. **Figure 21** shows the initial configurations of Model-1 and Model-2. The virgin asphalt Model is not shown.

The computation methods described in chapter 3.4 were used to determine the shear viscosity, self-diffusion coefficient, and RDFs of asphalt models in this chapter.

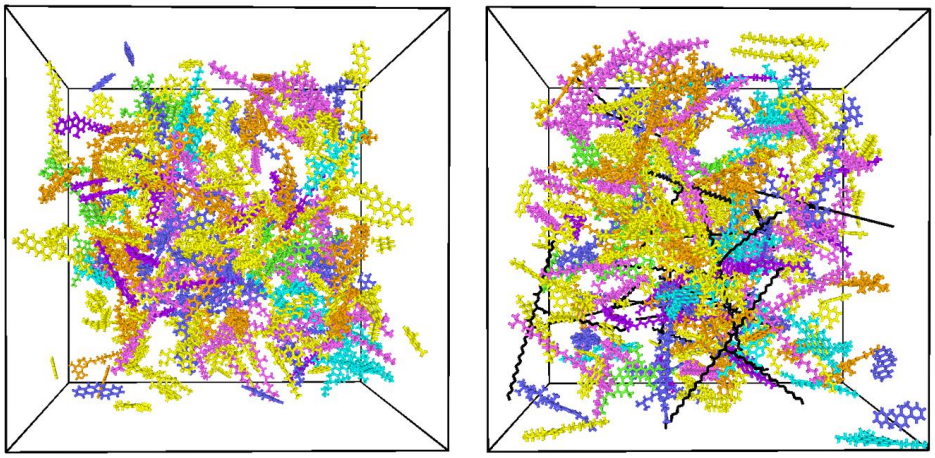

Figure 21. Initial configurations: (Left) the aged asphalt, Model-1; (Right) the TG/aged asphalt, Model-2. The color codes are: blue, virgin asphaltenes; purple, virgin resins; yellow, virgin aromatics; light pink, saturates; green, aged asphaltenes; orange, aged resins; dark pink, aged aromatics; black, TG.

4.3 Results and Discussions

4.3.1 Shear Viscosity

The SLLOD method calculates the shear viscosities of Model-0, Model-1, and Model-2. In addition, once the shear viscosities at different shear rates of Model-0, Model-1, and Model-2 were determined, two empirical models were used to predict their zero-shear viscosities. The first empirical model is the cross model[184, 186] which can be expressed as:

$$\mu = \mu_\infty + (\mu_0 - \mu_\infty)/[1 + (K\dot{r})^m] \quad (4.1)$$

Where μ is the shear viscosity at the shear rate $\dot{r}$, μ_0 is the zero-shear viscosity, μ_∞ is the shear viscosity at the infinite shear rate, K is the cross-time constant, and m is a power-law exponent. The second empirical model is known as the Carreau-Yasuda model[184, 196], which can be expressed as:

$$\mu = \mu_0/[1 + (\dot{r}/\dot{r}_c)^2]^p \quad (4.2)$$

Where $\dot{r}_c$ means a critical shear rate for the onset of the shear-thinning region and p is a power-law exponent.

Figure 22 shows the shear viscosities of Model-0, Model-1, and Model-2 at different shear rates at 1 atm and 404 K. The Cross model and Carreau model were used to fit the data of Model-1 and Model-2. The shear viscosity of Model-2 at every shear rate is smaller than that of Model-1, even at low shear rates with a relatively large error bar (shear rates < 1E8 1/s). This result indicates that the TG could reduce the shear viscosity of aged asphalt. From the shear rates of 4×10^8 (1/s) to 8×10^9 (1/s), the shear viscosity decreases fast, indicating a shear-thinning behavior. The shear-thinning behavior of asphalt can be simply described as follows. The asphaltenes in asphalt tend to form nanoaggregates[31, 184] and cause the high viscosity of asphalt. As the shear rate increases, the aggregations in asphalt are gradually broken up and sharply reduce the asphalt viscosity. In addition, I believe the high shear rate could also separate the TG molecules from other asphalt molecules and thus weaken the effect of TG on the viscosity of Model-1. This is why the shear viscosities of Model-1 and Model-2 at high shear rates (>1E9 1/s) are almost the same. In general, both empirical models fit adequately well to the viscosity data of Model-1 and Model-2. The values of the parameters corresponding to the two empirical models are listed in **Table 3** and **Table 4**. The values of zero-shear viscosity (μ_0) predicted by two empirical models are similar.

It is a fact that those four shear viscosity values in the low shear rate region (shear rates < 1E8 1/s) have poor accuracy (large error bar). In the experiment, the Couette flow induced on the asphalt sample to estimate the shear viscosity is imposed by the external force on the macroscopic level. In contrast, the SLLOD method in the MD simulation

induces the Couette flow on the asphalt model not by imposing the external force but by setting the linear velocity profile on the atomic level. The linearity of the velocity profile significantly affects the accuracy of the predicted shear-viscosity value. Good linearity of the velocity profile means the velocity gradient can be well transported from the top layer to the bottom layer of the model and can lead to an accurate shear viscosity value. In the simple liquid system, the linear velocity profile can keep well in both low and high shear rate regions due to the homogenous distribution of molecules in the system. But in a complex liquid system, such as asphalt, the molecular structure of most asphalt molecules is not simple but very complicated. Besides, some asphalt molecules form aggregations and entanglements. These two factors highly affect the linearity of the velocity profile. For example, at the low shear rate, the small shear velocity can't break up the aggregations and entanglements formed between asphalt molecules, which significantly disturbs the velocity profile and predicts a viscosity value with a large error bar. At the high shear rate, the large shear velocity can separate the aggregations and entanglements formed between the asphalt molecules (shear thinning behavior), which keeps the linearity of the velocity profile well and then results in a viscosity value with a small error bar.

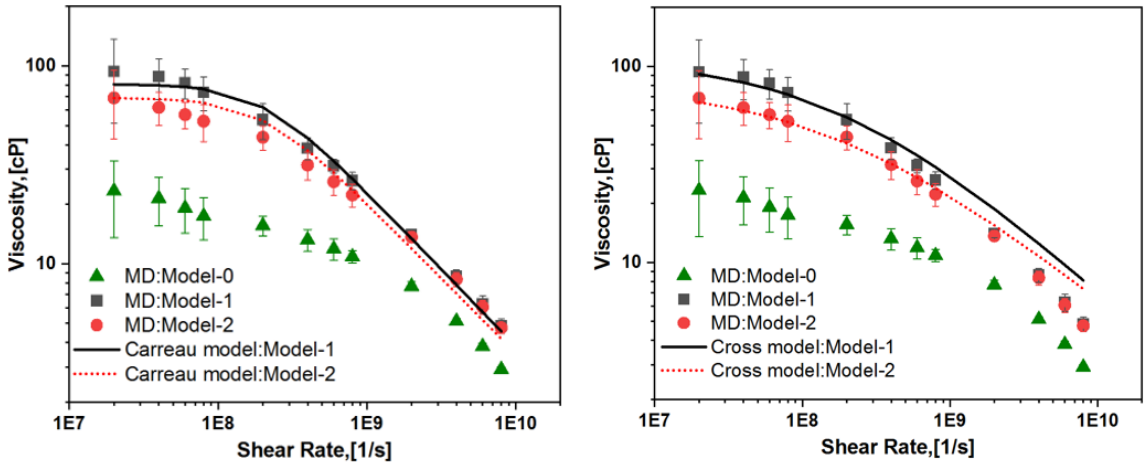

Figure 22.Shear viscosities of three asphalt models with different shear rates.

Table 3. Values of parameters in the Carreau model used to fit the shear viscosity curves of Model-1 and Model-2.

	μ_0(cP)	$\tau(s)$	p
Model-1	83	5.0×10^{-9}	0.39
Model-2	69	5.0×10^{-9}	0.38

Table 4. Values of parameters in the Cross model used to fit the shear viscosity curves of Model-1 and Model-2.

	μ_0(cP)	K(s)	μ_∞(cP)	m
Model-1	110	2.0×10^{8}	0.12	0.69
Model-2	81	2.0×10^{8}	0.17	0.63

4.3.2 Radial Distribution Function

In chapter 4.3.1, it is observed that the addition of TG could reduce the shear viscosity of aged asphalt, but the mechanism corresponding to this observation has not been understood. Asphaltene is the most viscous and polar component in asphalt, and

asphaltenes strongly contribute to the asphalt's viscosity. Therefore, to study this mechanism, I only focused on analyzing the interaction between the asphaltene-asphaltene molecules in Model-1 and Model-2. MD simulations were conducted for another 30 ns at the NPT ensemble after the first 40 ns to generate 3000 trajectory files for RDF analysis. In every trajectory file, the position of the center atom of each asphaltene molecule was used to determine the RDFs.

The RDFs of aged asphaltene-aged asphaltene, virgin asphaltene-virgin asphaltene, and aged asphaltene-virgin asphaltene pairs in Model-1 are shown in **Figure 23**. At first, the RDFs of all these three pairs have a strong first peak around 4.0 Å, indicating that the asphaltene molecules tend to form aggregations. Three types of asphaltene aggregation are formed: the aggregation formed between aged asphaltene with aged asphaltene molecules, the aggregation formed between aged asphaltene with virgin asphaltene molecules, and the aggregation formed between virgin asphaltene with virgin asphaltene molecules. Among these three types of asphaltene aggregation, the strength of aggregation formed between aged asphaltene molecules is the strongest since its RDF has the highest height of the first peak. The strength of aggregation formed between virgin asphaltene molecules is the weakest because its RDF has the lowest height of the first peak. In the aged asphaltene-aged asphaltene pair, its' RDF even shows a second peak around 11 Å, indicating an extension of the stacked structure. Such a nano-aggregation structure of asphaltene molecules has also been found in other studies[197, 198], which gives me some confidence in the reliability of my RDF analysis. Last but not least, all three pairs have a first peak around 4.0 Å, which means the interaction distance between the two asphaltene molecules is

around 4.0 Å. This distance is very close to the minimum distance between molecules caused by the van der Waals interaction[197].

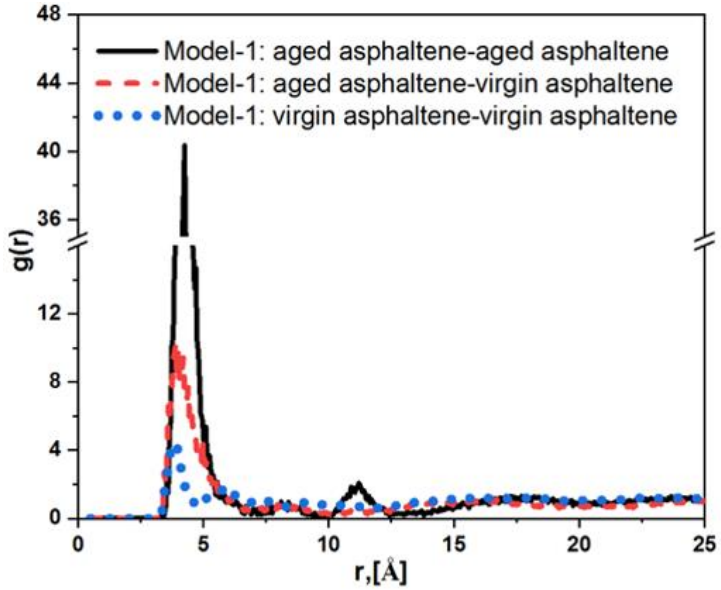

Figure 23. RDFs of different asphaltene-asphaltene pairs in Model-1.

Figure 24 shows the RDFs of aged asphaltene-aged asphaltene pairs in Model-1 and Model-2. By directly comparing these two RDFs, there are two important observations. The first observation is the first peak of RDF of aged asphaltene-aged asphaltene pair moves from 4.0 Å to 7.5 Å after introducing the TG molecules into the aged model. This observation indicates that the TG molecules could move between the aged asphaltene molecules and increase the distance between the aged asphaltene molecules from 4.0 Å to 7.5 Å. The second observation is that the height of the first peak of aged asphaltene-aged asphaltene RDF has a large drawdown from g(r) = 40 to g(r) = 10, and the second peak of aged asphaltene-aged asphaltene RDF disappears as the introduction of TG molecules into the Model-1. The g(r) = 10 means the aggregations still form between aged asphaltene molecules in Model-2. However, the strength of aggregations formed between aged

asphaltene molecules in Model-2 is much smaller than that in Model-1. The second observation indicates that the TG molecule can strongly weaken the aggregation formed between the aged asphaltene molecules. **Figure 25** shows the weakening effect of TG on the aggregations formed between the aged asphaltene molecules. It is clear that in Model-2, the TG molecules approach and move around the aged asphaltene molecules, which weakens the interaction between the aged asphaltene molecules. In **Figure 25(a)**, the aggregations formed between aged asphaltene molecules result in large-size asphaltene clusters. While, in **Figure 25(b),** the size of asphaltene clusters is minimized after introducing the TG.

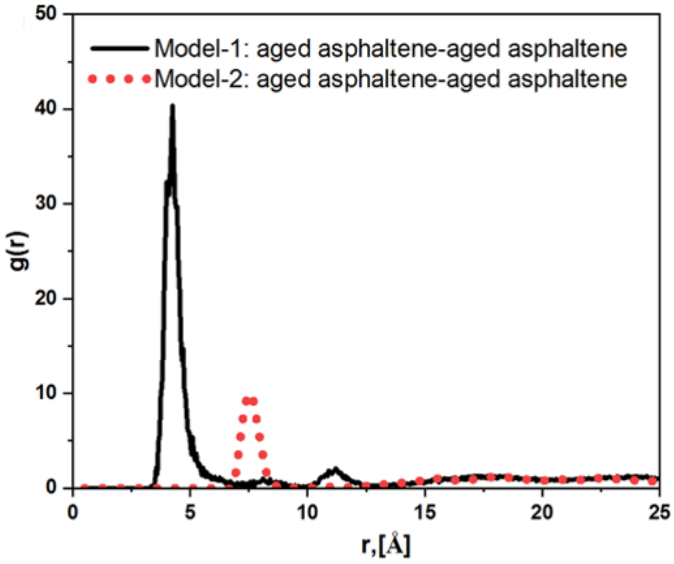

Figure 24. RDFs of aged asphaltene-aged asphaltene pair in Model-1 and Model-2.

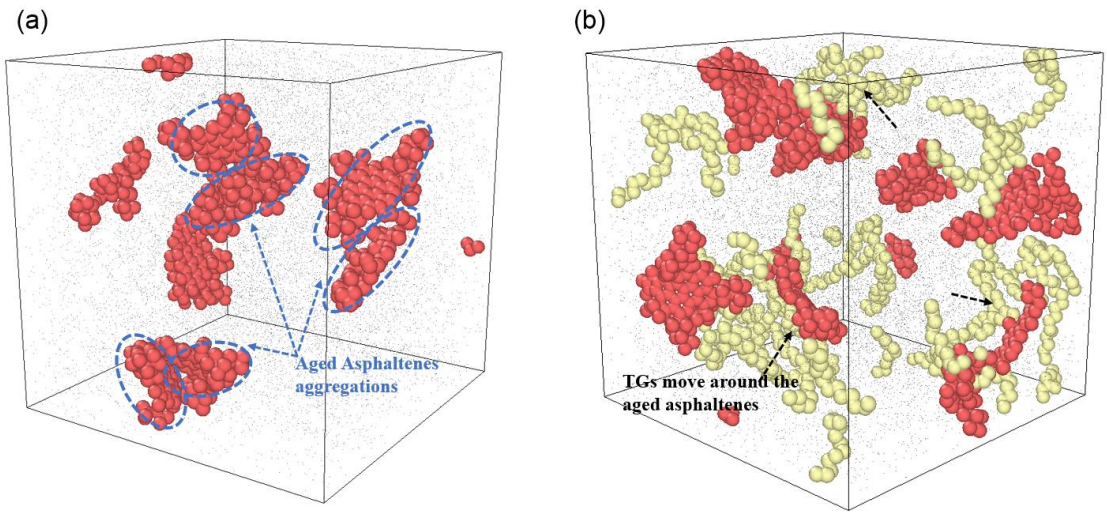

Figure 25. Visualization of TG weakening effect on the aggregations between the aged asphaltene molecules. (A): Configuration of Model-1 in simulation at 27.5 ns, red: aged asphaltene molecules. (B): Configuration of Model-2 in simulation at 32.4 ns, yellow: TG molecules.

Figure 26 shows the RDFs of the aged asphaltene-virgin asphaltene pairs in Model-1 and Model-2. The effect of TG molecules on the interaction between the aged asphaltene with virgin asphaltene molecules is the same as it is on the interaction between the aged asphaltene with aged asphaltene molecules. The g(r) value at the first peak of aged asphaltene-virgin asphaltene RDF decreases from 10 to 4.8, which means the TG molecule can also weaken the aggregation formed between aged asphaltene with virgin asphaltene molecules.

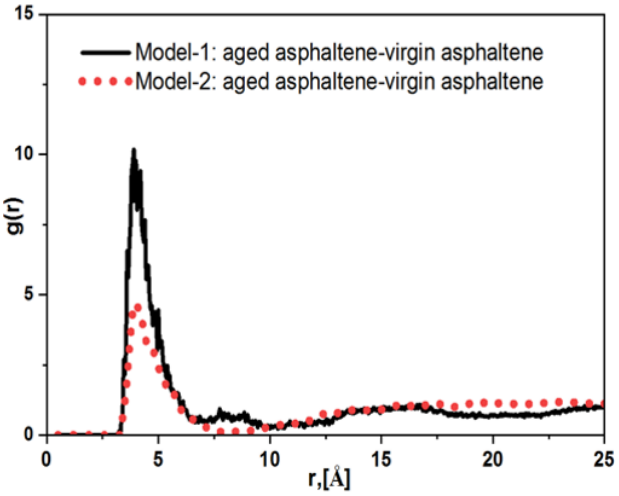

Figure 26. RDFs of aged asphaltene-virgin asphaltene pair in Model-1 and Model-2.

Figure 27 shows the RDFs of virgin asphaltene-virgin asphaltene pairs in Model-1 and Model-2. The g(r) value at the first peak of RDF decreases from 4.0 to 1.9, indicating the TG molecule can also weaken the aggregation formed between the virgin asphaltene molecules. However, the weakening effect is not too strong.

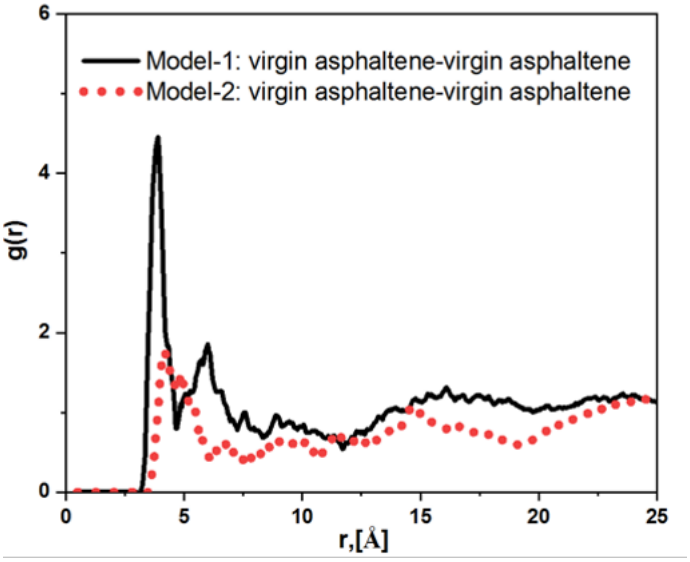

Figure 27. RDFs of virgin asphaltene-virgin asphaltene pair in Model-1 and Model-2.

Figure 23 to **Figure 27**, there are some interesting observations. At first, among those three asphaltene aggregations, the aggregation strength from the strongest to the weakest is the aggregation formed between aged asphaltene molecules, the aggregation formed between aged asphaltene with virgin asphaltene molecules, and then the aggregation formed between virgin asphaltene molecules. This indicates that oxygen-containing groups can enhance the molecular interaction between asphaltene molecules. This observation has also been found in Xu's study[170]. Second, the TG molecule can weaken the aggregation formed between asphaltene molecules and thus decrease the size of the asphaltene cluster, which is why TG can decrease the viscosity of aged asphalt.

4.3.3 Self-diffusion Coefficient

The MSDs of Model-0, Model-1, and Model-2 at 404 K were computed by conducting another 30 ns after the first 40 ns simulation at 404 K. The MSDs are shown in **Figure 28**, and their corresponding self-diffusion coefficients are listed in **Table 5**. From the result, oxidation significantly decreases the self-diffusion coefficient of the virgin asphalt model, and the additional TG can recover the self-diffusion coefficient of the aged asphalt model.

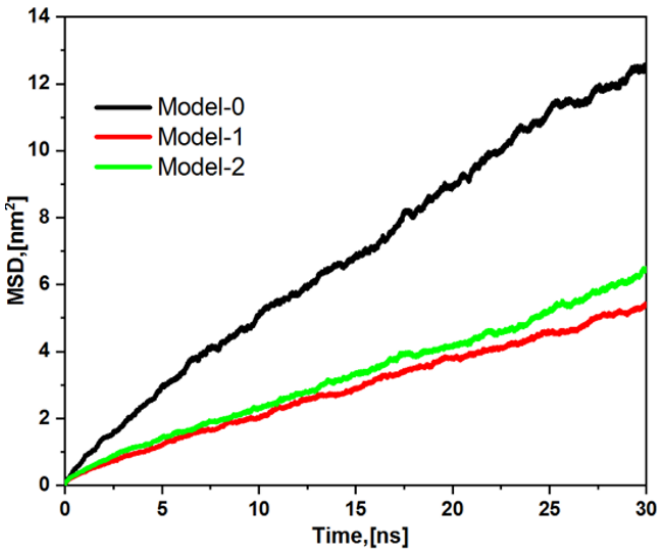

Figure 28. MSDs of three asphalt models at 404 K and 1 atm.

Next, the effect of TG on the self-diffusion coefficients of asphaltenes was determined. The asphaltenes in asphalt normally have the lowest self-diffusion coefficient. Thus, increasing the self-diffusion coefficient of the asphaltenes can improve the self-diffusion coefficient of the entire asphalt. **Figure 29** shows MSDs of asphaltene and TG molecules in Model-1 and Model-2. The self-diffusion coefficients of TG, virgin, and aged asphaltene molecules in Model-1 and Model-2 are listed in **Table 5**. The results are consistent with the RDFs analysis in chapter 4.3.2. In Model-1, virgin and aged asphaltene molecules highly tend to form asphaltene aggregations without the TG molecules. Therefore, they have the smallest diffusion coefficients.

Moreover, the self-diffusion coefficient of aged asphaltene molecules is much smaller than that of virgin asphaltene molecules in Model-1. This is because, in Model-1, the aggregations formed between the aged asphaltenes are much stronger than those formed between the virgin asphaltenes, which is also consistent with the RDFs in **Figure 23**. In

Model-2, the TG molecules weaken the aggregations formed between the asphaltenes and minimize the size of asphaltene clusters, so the self-diffusion coefficients of both aged asphaltenes and virgin asphaltenes increase.

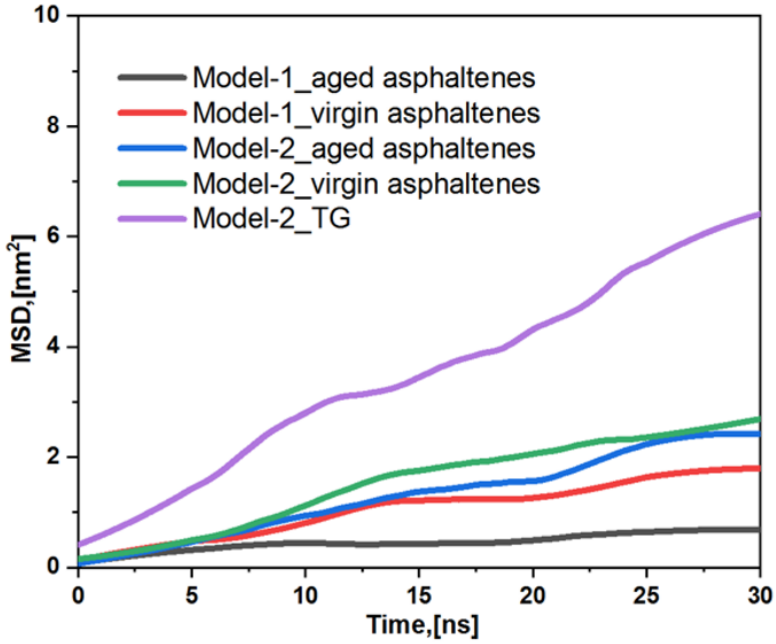

Figure 29. Comparison of the MSDs of asphaltenes in Model-1 and Model-2 at 404 K.

Table 5. The self-diffusion coefficients of the entire Model-0, Model-1, Model-2, different types of asphaltene and TG molecules in the Model-1 and Model-2 at 404 K.

	Self-diffusion coefficient (cm^2/s)
Model-0	6.79E-07
Model-1	2.81E-07
Model-2	3.24E-07
Model-1: Aged Asphaltenes	2.80E-08
Model-1: Virgin Asphaltenes	9.30E-08
Model-2: Aged Asphaltenes	1.38E-07
Model-2: Virgin Asphaltenes	1.50E-07
Model-2: TG	3.29E-07

4.3.4 Consideration of WCO Dosage on Aged Asphalt Reclamation

Determination of the optimal WCO dosage is important because it directly affects the performance of WCO-modified aged asphalt. In most experimental studies, the optimal dosage of WCO is decided when it can restore the properties of aged asphalt to its virgin state. The optimal WCO dosage determined in previous studies is in a wide range because it depends on several factors, such as the aged asphalt sample tested, the type of WCO used, and the aging state of the asphalt sample. For example, Ji *et al*.[52] found that 6% of waste cooking vegetable oil could restore the viscosity, rutting resistance factor, and fatigue resistance factor of aged asphalt binder to its virgin state. Shorbagy *et al*.[53] added the optimum dosage of 3.5% WCO into the aged 60/70 bitumen and restored the rutting parameter ($G^*/\sin\delta$) of aged 60/70 bitumen to the value before the aging. Gokalp *et al*.[54] found that 7% of waste vegetable cooking oil could restore the rutting resistance and fatigue resistance factors of aged bitumen to its virgin state. Cao *et al*.[55] compared the safety, physical, and rheological properties of an aged PEN70 asphalt sample with different dosages of waste vegetable oil to the virgin PEN70 asphalt sample and found the optimal dosage was 13.4 wt%. Sang *et al*.[56] found that the 70# aged asphalt binder with 6% waste edible animal oil has the best physical properties. In this chapter, the effect of WCO dosage on several important properties of aged asphalt was analyzed, such as molecular interaction, self-diffusion, cohesive energy density, surface free energy density, bulk modulus, shear modulus, and Poisson's ratio. Comparing the properties of virgin asphalt and aged asphalt with different dosages, this chapter determines the optimal WCO dosage for restoring a 5 years service-time aged asphalt. The compuational method of these properties is described

in chapter 3. The simulation temperature and pressure were set as 298 K and 1 atm, similar to the most of local weather conditions in the U.S.

The RDF analyses between asphaltenes-TGs and asphaltenes-asphaltenes with different TG dosages were used to study the effect of dosage on the molecular interaction and microstructure of aged asphalt. The RDFs of the asphaltene-TG pair in the TG-modified model with different TG dosages are shown in **Figure 30A**. In **Figure 30A**, the g(r) value at the first peak increases from 10% to 15% and keeps the same from 15% to 25%. This result indicates that, from 0-15% dosage, as more TG molecules are added into the aged asphalt model, the number of TG molecules around the asphaltene molecules increases. At the dosage of 15%, I believe the number of TG molecules around asphaltene molecules achieves a saturate condition. Therefore, even more TG molecules (> 15%) were added in the aged asphalt model; there were no more TG molecules that could approach the asphaltene molecules, which is the reason why the g(r) value at the first peak keeps the same as TG dosage increases from 15% to 25%. **Figure 30(B)** and **Figure 30(C)** show the RDFs of the asphaltene-asphaltene pair in the TG-modified asphalt model with different TG dosages. At first, in **Figure 30B**, the height of the first peak in RDF decreases due to the introduction of TG molecules. This means the additional TG molecules in the aged asphalt model can weaken and mitigate the aggregations formed between the asphaltene molecules. As the dosage increases from 0% to 15%, the more TG molecules approach the asphaltene molecules and separate the asphaltene molecules, which makes the mitigation effect stronger and results in a lower height of the first peak in asphaltene-asphaltene RDF. While, in **Figure 30C**, with the dosage from 15% to 25%, the height of the first peak in asphaltene-asphaltene RDF does not change. This means the mitigation effect of TG on the

asphaltene aggregations is limited and it is related to the number of TG molecules around the asphaltene molecules. The number of TG molecules around the asphaltene molecules reaches its maximum value (saturate condition) at the 15% dosage, so the mitigation effect of TG on the asphaltene aggregation is also maximized at the 15% dosage. The mitigation effect on asphaltene aggregations helps restore the rheological properties of the aged asphalt (for example, viscosity and self-diffusion discussed in the previous chapter). Therefore, from this point of view, the optimal TG dosage should be 15%.

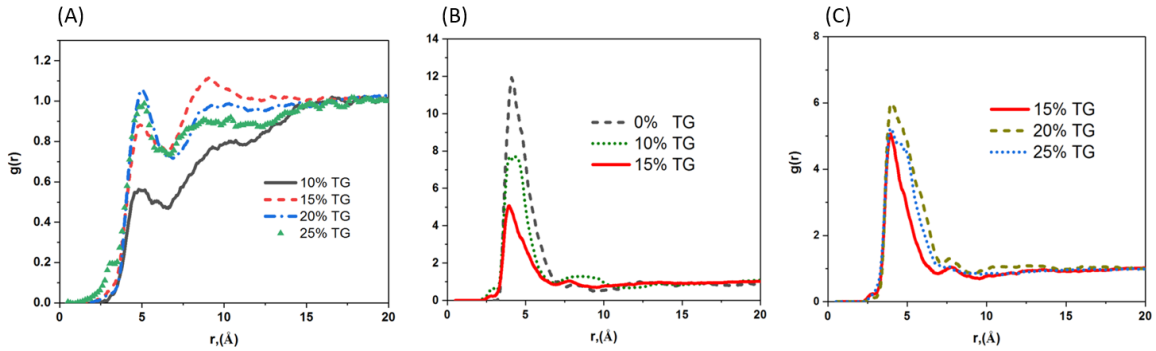

Figure 30. (A) RDFs of TG-asphaltene pair in TG-modified asphalt model with different TG dosages at 404 K. Asphaltene contains both virgin and aged asphaltene molecules. (B) (C): RDFs of asphaltene-asphaltene pair in TG-modified asphalt model with different TG dosages.

Figure 31(left) shows the CED increases after oxidation. This is because the polarity of the asphalt components is enhanced after oxidation, which increases the intermolecular interaction in the aged asphalt[199]. The increase of CED in asphalt is consistent with the increase in asphalt viscosity after oxidation. The TG molecules weaken the interactions between the asphaltene molecules, leading to decreased CED in the aged asphalt model. At the dosage of 15%, the CED in the aged asphalt model could be almost restored to the level of its virgin state. SFE reflects the ability of the asphalt to crack and

form a new surface. The large SFE of asphalt represents the strong brittleness of asphalt[166, 200]. In the right of **Figure 31**, the SFE of the virgin asphalt model increases after oxidation, which is consistent with the brittleness of asphalt increases after oxidation. The addition of TG has a positive effect on restoring the brittleness of aged asphalt because it decreases the SFE of the aged asphalt model. When the TG dosage is between 10-15%, the SFE of the aged asphalt model could be restored to the level of its virgin state.

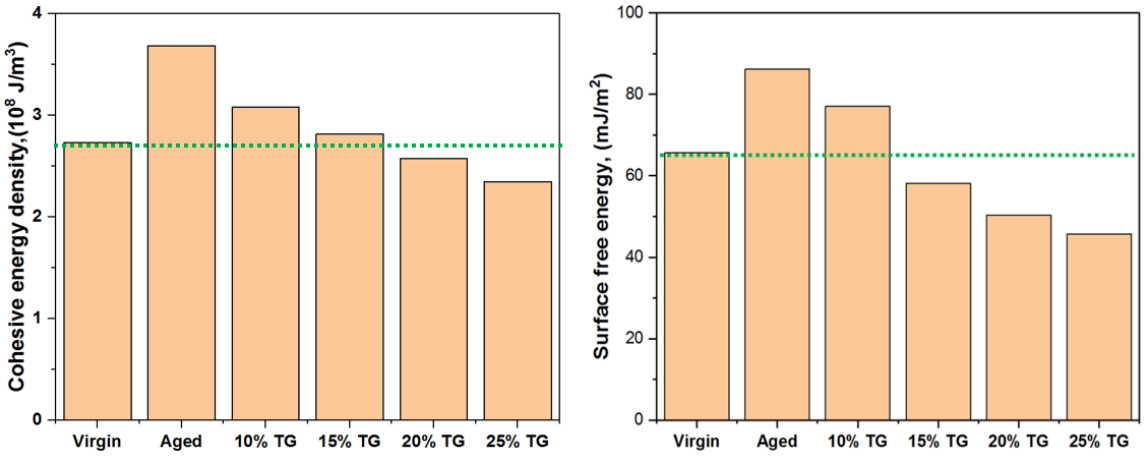

Figure 31. The cohesive energy density(left) and surface free energy density(right) of virgin asphalt model, aged asphalt model, and TG-modified asphalt model with different TG dosages at 298 K.

The bulk modulus can evaluate the resistance of the asphalt to uniform compression and the shear modulus can be used to evaluate the ability of asphalt to resist shear strain, both of which can be indicators for evaluating the deformation resistance of asphalt. **Figure 32(left)** shows the bulk and shear modulus of asphalt increase after oxidation, which is consistent with the observation that the hardness of asphalt increases after oxidation. The Poisson's ratio is an elastic constant that can reflect the lateral deformation of the asphalt. The Poisson's ratio of asphalt is not affected significantly by oxidation, only a slight

increase after the oxidation. The additional TG in the aged asphalt model decreases the bulk modulus, shear modulus, and Poisson's ratio of the aged asphalt model, indicating that the TG can soften the hardness of the aged asphalt model. When the TG dosage is between 10-15%, all these three mechanical properties of the aged asphalt model could be approximately restored to the level of its virgin state.

The self-diffusion coefficient is an important property of asphalt because it can be related to the self-healing rate of the asphalt. The higher self-diffusion coefficient brings a better self-healing behavior of asphalt. The MSD of virgin asphalt model, aged asphalt model, and TG-modified model with different TG dosages are shown in **Figure 32(right)** and their corresponding self-diffusion coefficients are 1.15E-08，4.51E-09，5.67E-09，8.83E-09，1.10E-08，1.10E-08 cm^2/s, respectively. According to the result, the self-diffusion coefficient of the virgin asphalt model decreases after oxidation. The additional TG can increase the self-diffusion coefficient of the aged asphalt model. When the TG dosage is between 20-25%, the self-diffusion coefficient of the aged asphalt model could be restored to the level of its virgin state.

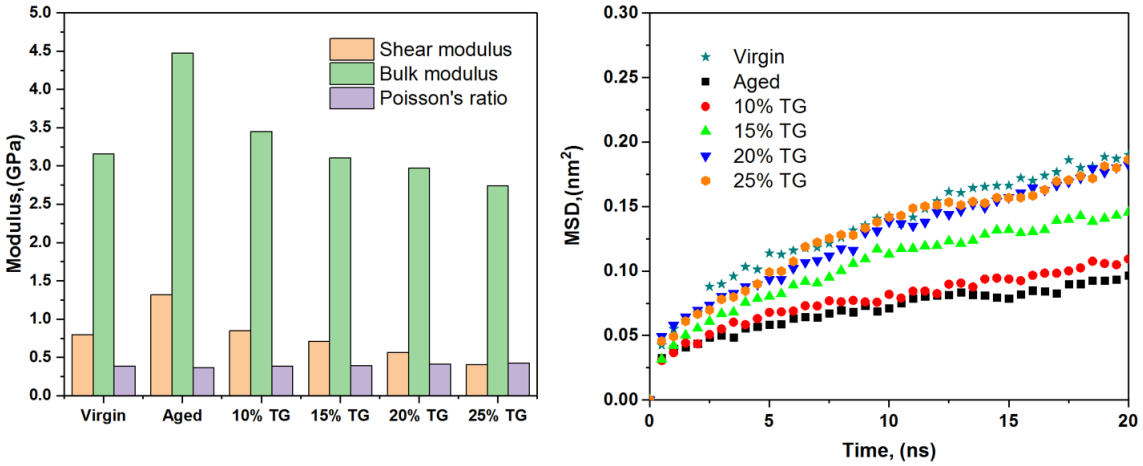

Figure 32. Mechanical properties(left) and MSDs(right) of virgin asphalt model, aged asphalt model, and TG-modified asphalt model with different TG dosages at 298 K.

The optimal TG dosage for restoring every property to its virgin state separately is listed in **Table 6**. Considering them together, the final optimal TG dosage should be in the range of 10-15%.

Table 6. The optimal TG dosage for each single asphalt property, separately.

Asphalt properties	Optimal TG dosage
Microstructure analysis (RDF)	15%
Surface free energy	10-15%
Cohesive energy density	15%
Shear modulus	10-15%
Bulk modulus	15%
Poisson's ratio	10%
Self-diffusion coefficient	20-25%

4.4 Conclusions

In this chapter, the effect of WCO on the viscosity, self-diffusion, and microstructure of aged asphalt was studied. Since the TG is the main component of the WCO, 10 wt.% TG was introduced in the aged asphalt model to study its effect on the properties of the aged asphalt model at 404 K and 1 atm. It was found that TG decreased the viscosity and increased the self-diffusion coefficient of aged asphalt, which was consistent with the observation from previous studies[51, 52]. The RDF was determined to study the microstructure of the aged asphalt/TG mixture. TG could decrease the viscosity and increase the self-diffusion coefficient of aged asphalt by weakening the aggregations formed between asphaltenes and decreasing the size of asphaltene clusters in aged asphalt. This finding describes the fundamental mechanism of using the WCO to restore aged asphalt.

In addition, the optimal dosage of TG was determined to restore a 5 years service-time aged asphalt model from microscopic and macroscopic views. At the microscopic level, the TG in the aged asphalt model has a mitigation effect on the aggregation formed between the asphaltenes. However, this mitigation effect is limited. When the TG dosage is around 15%, the mitigation effect is maximized. In other words, it means the aggregations formed between the asphaltenes in the aged asphalt are hard to break down fully by only using the TG. At the macroscopic level, the effects of TG dosage on self-diffusion, cohesive energy density, surface free energy density, bulk modulus, shear modulus, and Poisson's ratio of the aged asphalt model were studied. Generally, the TG can soften the aged asphalt model and reduce its hardness, consistent with previous experimental studies. Hence, as TG dosage increases, the self-diffusion rate of the aged asphalt model increases while the cohesive energy density, surface free energy density, and mechanical modulus decrease. Finally, based on macroscopic and microscopic analyses, the optimal TG dosage is decided, which should be in the range of 10-15% (on the weight percent of the aged asphalt model).

Chapter 5: A Study of Waste Polyethylene/Aged Asphalt Mixture

5.1 Introduction

Researchers have recently used waste plastics to restore and improve the properties of aged asphalt. It is found that plastics could restore the properties of aged asphalt, such as workability, rutting resistance, fatigue resistance, low-temperature cracking resistance, mechanical properties, softening point, ductility, and so on[8, 201-204]. PE has become more popular among various plastics due to its excellent resistance to heat and oxidation and low price[205]. For example, Peng *et al*.[206] combined the waste engine oil and WPE to modify the asphalt that experienced the ultraviolet aging process. They found that the combination of waste engine oil and WPE could improve the storage stability of aged asphalt. In addition, using the AFM, they observed the WPE dispersed in the aged asphalt and retarded the formation of the "Bee-like" structure in the aged asphalt. Ye *et al*.[207] made several rejuvenators by combining different proportions of waste vegetable oil and LDPE. They used rejuvenators to modify the aged asphalt. They found that the workability and low-temperature performance of the rejuvenated asphalt were restored to the level of its virgin state. The fatigue and high-temperature performance of rejuvenated asphalt were better than its virgin state. Finally, they noted that the 15% waste vegetable oil combined with 4% LDPE would yield the best rejuvenator for modifying the aged asphalt. Guo[178] studied the effect of LDPE on the adhesion ability between aged bitumen with aggregate minerals. He found that the adhesion ability between the bitumen and mineral increases when the LDPE mixes with aged bitumen via the wet method. While the adhesion ability between the bitumen and mineral decreases once the LDPE is introduced by the dry method. Two experimental studies[208, 209] and one simulation study[210] found that PE could reduce the

viscosity of virgin and aged asphalt under high-temperature conditions.

As mentioned above, various properties of asphalt could be modified or restored by PE, but the corresponding mechanism hasn't been understood well. In this chapter, the effect of WPE on the microstructure of aged asphalt was investigated via RDF analysis, which could be a reference for understanding the modification mechanism of PE/WPE on aged asphalt. In addition, since the maleic anhydride functional group (MAH) grafted on PE could enhance the compatibility and stability between PE and asphalt[211-213], the MAH was also added on WPE to build the maleic anhydride grafted polyethylene (WPE-g-MAH) and study its effect on microstructure structure of aged asphalt, which hasn't been reported before.

5.2 Models and Simulation Details

Three different asphalt models were built in this chapter. They are the aged asphalt model, the WPE-modified asphalt model, and the WPE-g-MAH asphalt model. The details of the aged asphalt model are described in chapter 3, and its configuration is shown in Error! R eference source not found. The molecular weight of PE used in Yan's experimental study[208] was between 540 to 3418. Thus, the WPE used in this chapter had an MW of around 1400 g/mol ($C_{100}H_{202}$). Guo[178] and Chang *et al.*[155] used the branched alkane model representing the LDPE molecule in their MD simulation. However, in this chapter, a typical polymer structure with only one linear straight chain was used for representing WPE molecules[71, 214-218]. The single PE model is shown in Error! Reference source not found. The molecular model of WPE-g-MAH was constructed by adding MAH functional groups into the PE model as shown in Error! Reference source not found.

According to the experimental studies[62, 219-223], the dosage of PE mixed with asphalt normally was in the range of 2-12% by weight of asphalt. Thus, 9 WPE molecules (about 8 wt%) were introduced into aged asphalt to build WPE-modified asphalt (simply written as PE-modified asphalt in the following content). Similarly, 9 WPE-g-MAH molecules (about 13 wt%) were introduced into aged asphalt to build WPE-g-MAH modified asphalt (written as PE-g-MAH modified asphalt in the following content).

The OPLS-AA force field has been adopted to describe the interaction potential between the asphalt molecules. The partial charge for each atom in the asphalt molecule was determined using the Charge Equilibration method[224]. The united atom (UA) model is used to describe the PE molecule, which means each methyl (CH3) and methylene (CH2) unit in PE is treated as one interaction site. The force fields for describing the potential of PE and MAH came from Siepmann's study[225] and Mayo's study[226], respectively. The method of computing RDFs is described in chapter 3. The temperature and pressure were set as 298 K and 1 atm.

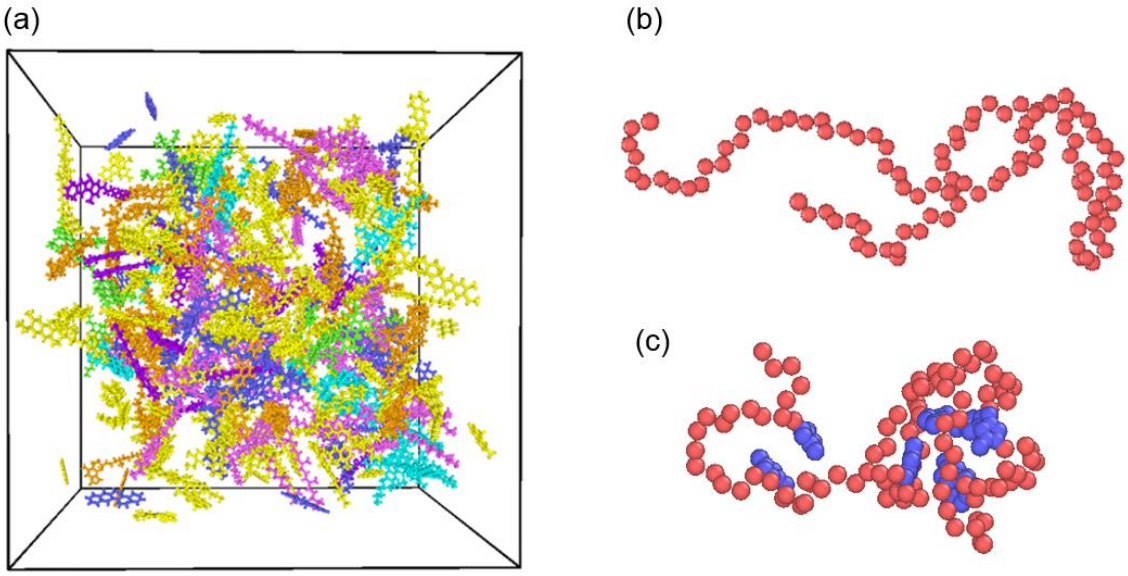

Figure 33. (a) Initial configuration of aged asphalt model in MD simulation. The color codes are blue, virgin asphaltenes; purple, virgin resins; yellow, virgin aromatics; light pink, saturates; green, aged asphaltenes; orange, aged resins; dark pink, aged aromatics. (b) molecular model of a single PE molecule. (c) molecular model of a single PE-g-MAH molecule. Red: -CH_2-, -CH_3 groups, Blue: MAH group.

5.3 Results and Discussions

As discussed before, the asphaltene fraction plays a key role in the property behavior of asphalt. Therefore, I still only analyze the interactions between asphaltene/SARA fractions as shown in **Figure 34**. Without introducing PE molecules, the RDF of the asphaltene-asphaltene pair has the largest g(r) value at its first peak, indicating strong preferential interactions between asphaltene molecules. Such strong interactions between asphaltene molecules result in the formation of asphaltene aggregations/clusters in the aged asphalt (as shown in **Figure 25**) which significantly contributes to the rheological properties of aged asphalt. The RDF of the asphaltene-resin pair has the second largest g(r) value at its first peak, indicating preferential interactions also exist between asphaltene and resin molecules. However, its interaction strength is much smaller than that

between the asphaltene and asphaltene molecules. The RDFs of asphaltene-aromatic and asphaltene-saturate pairs have a g(r) value close to 1 (around 1.25) at their first peak, indicating very small preferential interactions between asphaltene molecules with aromatic/saturate molecules. These molecular-level structural observations are consistent with the colloidal structure of asphalt observed by Lesueur[227]. In the colloidal structure of asphalt, asphaltenes highly tend to aggregate and form asphaltene micelles. Resins form the shells around micelles as a stabilizer of the micelle, while aromatics/saturates behave as a dispersion medium.

With the introduction of PE in aged asphalt, the RDF of the asphaltene-asphaltene pair didn't have an obvious change, indicating the additional PE would not affect the interactions between asphaltene molecules and thus would not mitigate the formation of asphaltene clusters in aged asphalt. While the RDFs of asphaltene-aromatic, asphaltene-resin, and asphaltene-saturate pairs show that their first peak value had decreased, indicating the additional PE could weaken the interactions between asphaltenes with aromatics, resins, and saturates.

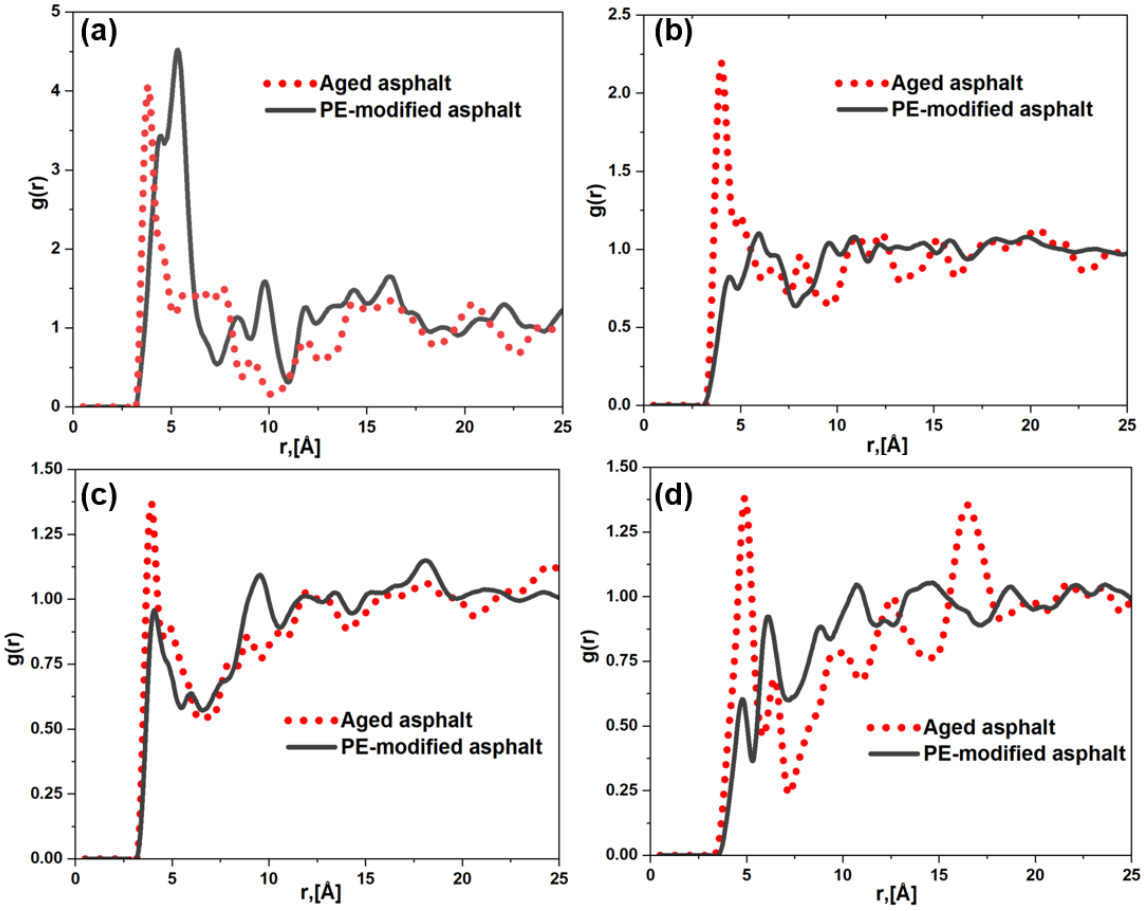

Figure 34. RDFs of asphaltene-SARA fractions in aged asphalt model and PE-modified asphalt model. (a) RDFs of asphaltenes-asphaltenes pair. (b) RDFs of asphaltenes-resins pair. (c) RDFs of asphaltenes-aromatics pair. (d) RDFs of asphaltenes-saturates pair.

Figure 35 shows the RDFs of PE-SARA fractions. The RDF of the PE-asphaltene pair has the smallest g(r) value at its first peak, indicating that the interaction between the PE and asphaltene is smaller than that between the PE with the other three fractions (maltenes). The RDFs of PE-saturate and PE-aromatic pairs have the first peak value larger than 1, indicating the PE molecules prefer to attract or adsorb low-MW and small polarity molecules.

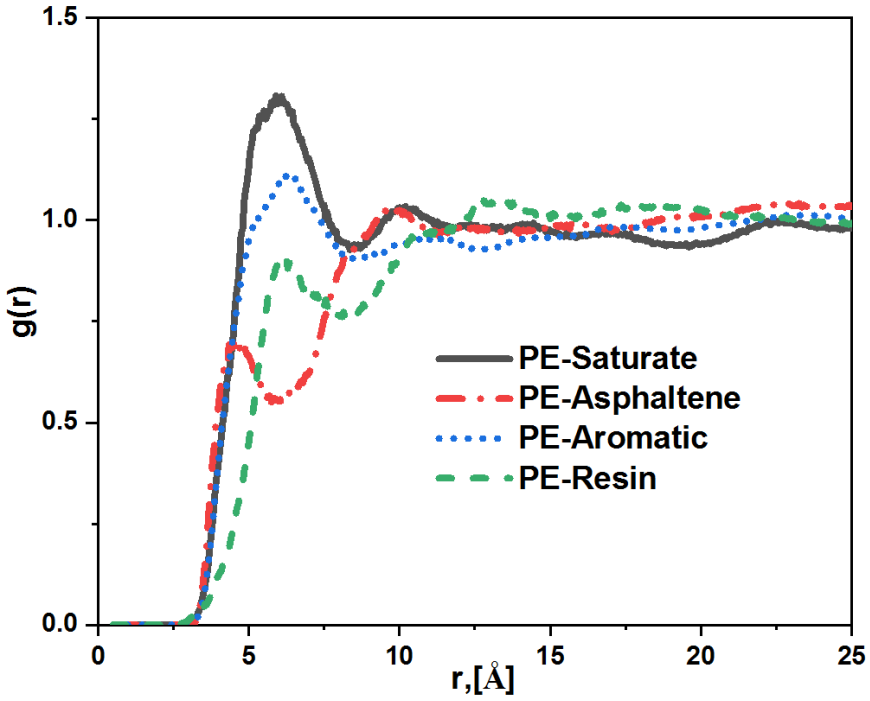

Figure 35. RDFs of PE-SARA fractions in PE-modified asphalt model.

The strong preferential interactions among asphaltene molecules result in large-size asphaltene clusters in aged asphalt. Reducing the interactions between asphaltene molecules and mitigating the formation of asphaltene clusters could efficiently restore the rheological properties of aged asphalt, for example, viscosity and self-diffusion. The MAH functional groups were added on the WPE molecule to enhance its polarity, wishing the PE-g-MAH molecules could interact with asphaltene molecules and reduce the interactions between asphaltene-asphaltene molecules. The effect of PE-g-MAH on RDFs of asphaltene-SARA fractions is shown in **Figure 36** below. By comparing the RDFs of PE-g-MAH modified asphalt and aged asphalt, only the RDF of the asphaltene-resin pair decreased its g(r) value at the first peak, indicating the additional PE-g-MAH reduced the interaction between asphaltene and resin molecules. By comparing the RDFs of PE-

modified asphalt and PE-g-MAH modified asphalt, an obvious observation is that the RDFs of asphaltene-aromatic and asphaltene-saturate pairs had an increase in the g(r) value at their first peak, indicating the MAH functional group enhanced the interactions between asphaltene-aromatic and asphaltene-saturate molecules. However, the RDF of the asphaltene-asphaltene pair still did not be affected by MAH functional group, indicating that the MAH functional groups could not reduce the interaction between asphaltene molecules and mitigate the formation of asphaltene clusters.

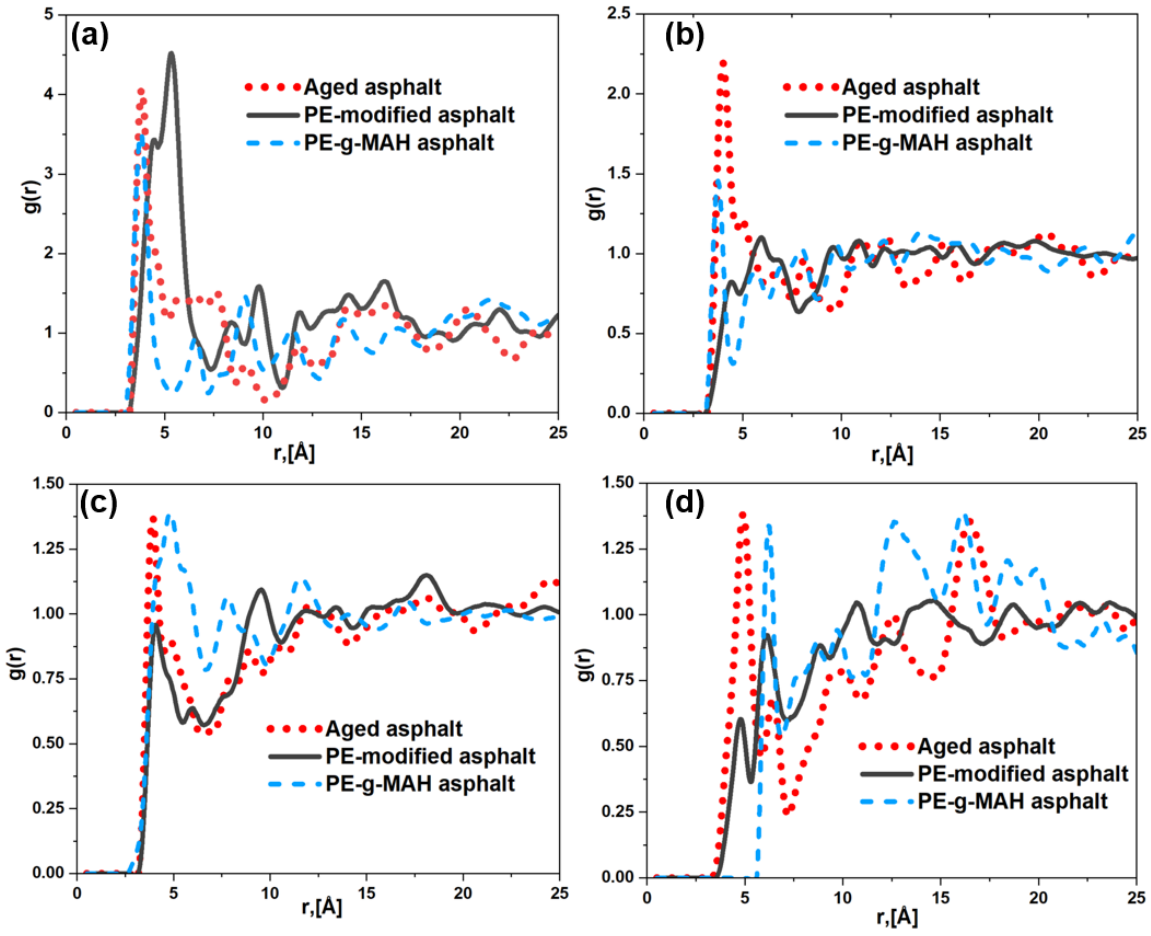

Figure 36. RDFs of asphaltene-SARA fractions in aged asphalt, PE-modified asphalt, and PE-g-MAH modified asphalt model s. (a) RDFs of asphaltenes-asphaltenes pair. (b) RDFs of asphaltenes-resins pair. (c) RDFs of asphaltenes-aromatics pair. (d) RDFs of asphaltenes-saturates pair.

Figure 37 shows the RDFs of MAH-SARA fractions. In **Figure 37**, only the RDF of MAH-asphaltene pair had a strong first peak, indicating that MAH functional groups preferentially interacted with only asphaltene molecules, which could enhance the interaction between PE-g-MAH and asphaltene molecules. However, I believe the strength of interaction between MAH and asphaltene molecules was smaller than that between asphaltene-asphaltene molecules, which is why the RDF of the asphaltene-asphaltene pair still did not be affected by PE-g-MAH.

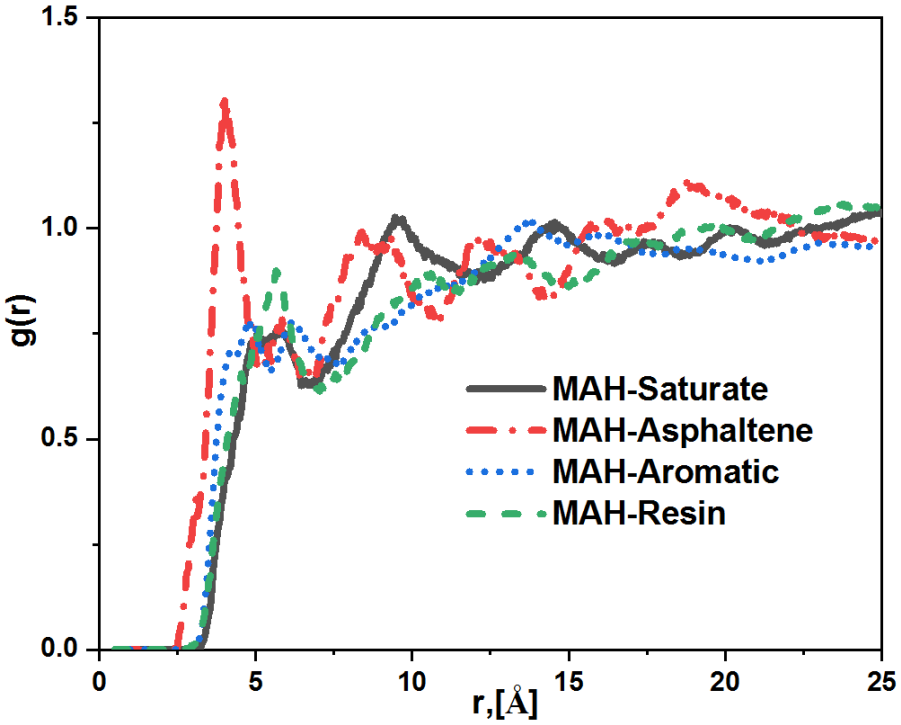

Figure 37. RDFs of MAH-SARA fractions in PE-g-MAH modified asphalt model.

Due to the difference between the density and polarity of PE and asphalt components, the phase separation of PE-modified asphalt was commonly observed in experimental studies as shown in **Figure 38**. At a low PE concentration, the PE phase normally acted as a dispersed phase in asphalt, as shown in **Figure 39(b)**. As PE

concentration increased, the number and the size of the dispersed phase increased, and finally connected and separated from the asphalt phase, as shown in **Figure 39(e)**.

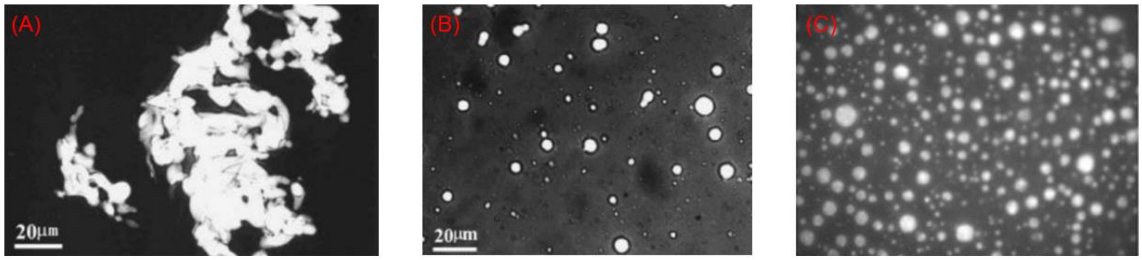

Figure 38. Scanning of asphalt microstructure with three different PEs. (A) Black: asphalt, white: HDPE[228]. (B) Black: asphalt, white: LLDPE[228]. (C) Black: asphalt, while: LDPE[61].

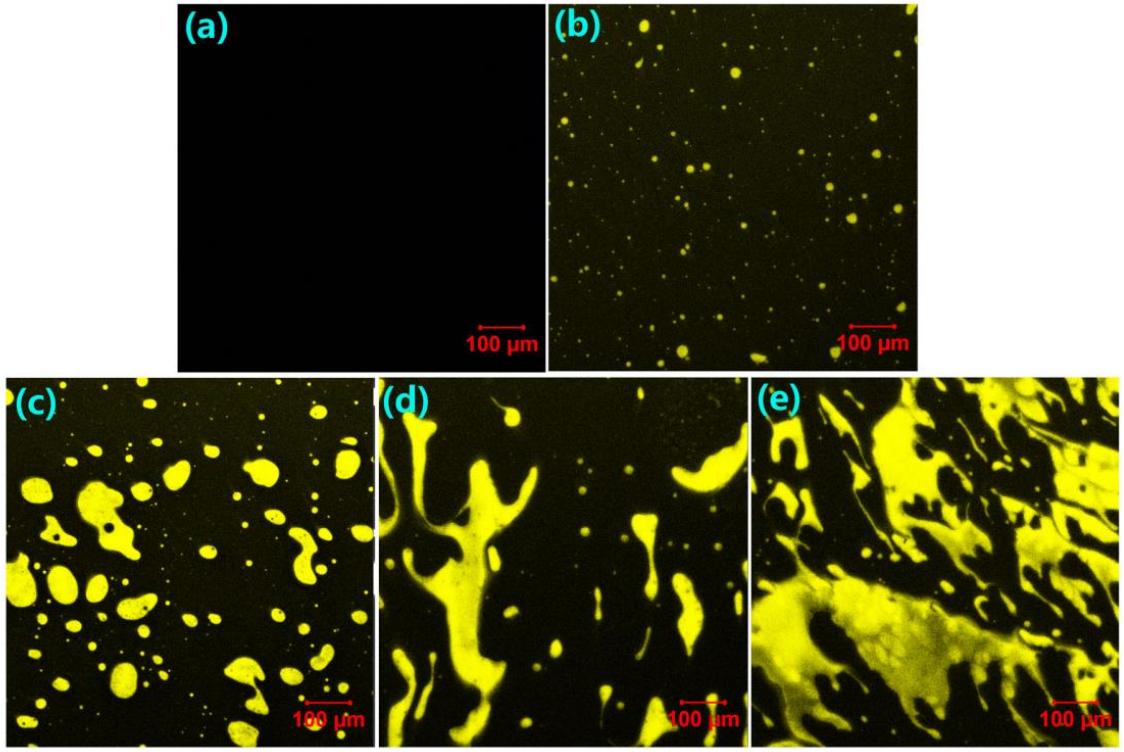

Figure 39. Scanning of asphalt microstructure with different concentrations of recycled PE, (a):0%, (b): 2%, (c): 4%, (d): 6%, and (e): 8%[229].

At 8% PE concentration, the visualization of PEs distribution in aged asphalt from MD simulation is shown in **Figure 40**. It didn't show there was any aggregation formed between PE molecules. The PE molecules were homogeneously distributed in the aged asphalt, indicating that the PE was completely miscible with aged asphalt and no phase separation existed. There are two likely reasons why my MD simulation couldn't model phase separation of PE-modified asphalt with 8% PE concentration. At first, the length of the PE molecules used in my simulation was too small to entangle with each other and form the dispersed phase. From another point of view, if the PE used to modify the asphalt has a small MW and short-enough chain length, the phase separation likely could be avoided. Second, the simulation scale size was not large enough to observe the formation of a separated PE phase in aged asphalt. For example, the scale of my MD simulation was on a nanoscale, while the scale of PE-modified asphalt scanned in the laboratory was on a microscale.

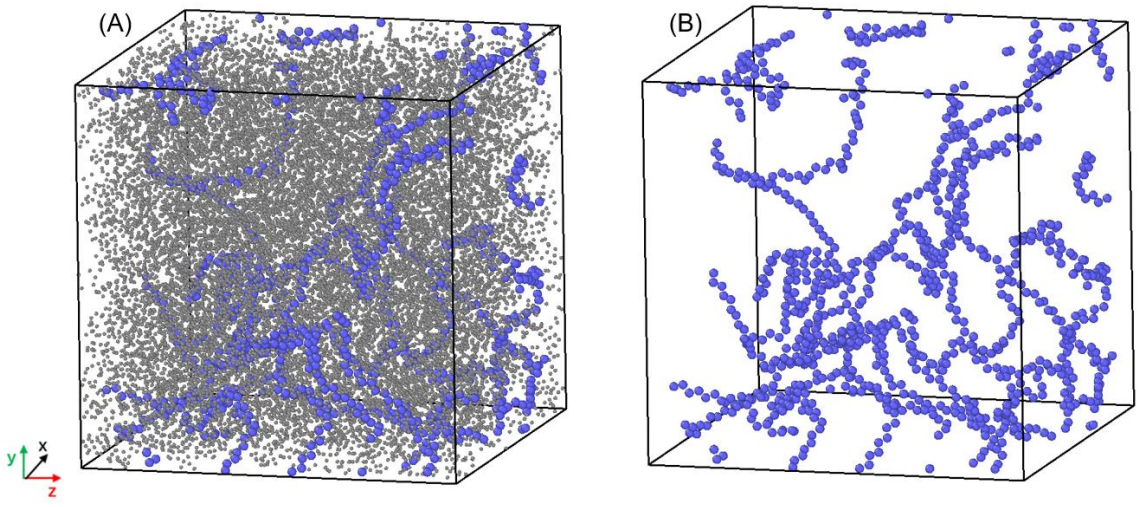

Figure 40. Visualization of PE molecules in PE-modified asphalt. (A). minimize the molecular size of asphalt molecules for clarity. (B). hide the asphalt molecules for clarity. Black: asphalt molecules, Blue: PE molecules.

5.4 Conclusions

In this chapter, the MD simulation was used to investigate the effect of PE and PE-g-MAH on the microstructure of aged asphalt. The result shows that PE preferentially interacts with the maltenes, thus weakening the interactions between asphaltenes and maltenes. The MAH functional group preferentially interacts with only asphaltenes and enhances the interaction between PE-g-MAH with asphaltenes. I believe this is why MAH could increase the compatibility between PE and asphalt. Besides, the MAH functional group enhances the interactions between asphaltenes-saturates and asphaltenes-aromatics.

Last but not least, PE and PE-g-MAH couldn't affect the interactions between asphaltenes-asphaltenes and mitigate the formation of asphaltene clusters in aged asphalt. However, it must be noted that the difference existed between the microstructure of PE-modified asphalt observed from MD simulation and experiments. Unlike the observation from experimental studies, the phase separation phenomenon of PE-modified asphalt hasn't been observed in MD simulation. According to this, a new point of view is that if the PE used to modify the asphalt has a small MW and short-enough chain length, the phase separation likely could be avoided.

Chapter 6: Low-pressure CO_2 in the Water-oil Interface for Enhanced Oil Recovery

6.1 Introduction

Tertiary-enhanced oil recovery techniques are widely implemented in conventional oil fields to recover residual oil. Out of available choices, the supercritical CO_2-EOR of the immiscible and miscible CO_2 flooding methods are effective tertiary EOR techniques[230, 231]. The miscible CO_2 flooding is designed for the reservoir with pressure above the MMP of the CO_2 and oil system. On the other hand, immiscible CO_2 flooding is popular for reservoirs with low pressure and medium/heavy components rich in oils[81]. Both techniques require CO_2 injection in the supercritical or vapor phase. The EOR is achieved via oil swelling and viscosity reduction. It is worth pointing out that even though the pore-level displacement efficiency is high, CO_2-EOR techniques may yield unfavorable sweeping efficiency due to gravity segregation and viscous fingering. The in-situ CO2 generation method was recently proposed and developed, demonstrating improved sweeping efficiencies[232-234].

As for the in-situ CO_2 EOR, three factors are important: the oil swelling, the viscosity reduction, and the IFT reduction between water and oil. IFT and interfacial properties of various systems, such as binary systems of (water + CO_2), (oil + CO_2), and the ternary system of (oil + water + CO_2), have been experimentally studied to understand the water-oil IFT reduction mechanism during CO_2-EOR. For example, Georgiadis *et al.*[235] implemented the pendant drop method to determine the IFT for the (H_2O + CO_2) system in the temperature range of 298 and 374 K with pressures up to 60 MPa. Abedini and co-workers[236-241] determined the equilibrium IFT of the crude oil–CO_2 system at 30℃ and

pressures from 0.66 to14.64 MPa in the laboratory. They observed that IFT piecewise decreased linearly with the increasing equilibrium pressures, as the decline slope is larger when the pressure is less than 6.84 MPa. They also measured the MMP of the oil–CO_2 system at 23, 30, 50, and 90℃. Georgiadis *et al.*[242] observed that as CO_2 concentration increased in the (oil + water + CO_2) system, the water-oil IFT decreased.

However, it is challenging to experimentally quantify and distinguish the CO_2 behavior at the microscopic water-oil interface and reveal the corresponding mechanisms. For instance, many laboratory CO_2 EOR studies only reported incremental oil recovery due to synergetic mechanisms but couldn't quantify the contribution of oil swelling, oil viscosity reduction, and the IFT change [84]. In recent years, MD simulations have been utilized to gain a molecular-level understanding of the CO_2 EOR process. Promising results have been reported to reveal the water/oil interface and how the injected CO_2 could affect interfacial properties. For example, Liu *et al.*[243] reported that CO_2 molecules preferentially accumulated at the water/oil interface at 10 MPa and 313 K. They attributed such accumulation to the IFT difference between water/CO_2 and water/oil. As the CO_2 concentration increased, they observed an increase in the water/oil interface roughness, an increase in the fluid mobility at the interface, and a decrease in water/oil IFT. Such observation is consistent with the experimental observation from Georgiadis *et al.* [242]. Zhao and co-workers[244] calculated the brine/CO_2/hexane system at 330 K and 20 MPa. They observed that the width of the interface region and the interface roughness between brine and hexane increased as CO_2 concentration increased, both of which caused the decrease of IFT between brine and hexane. Mohammed and Mansoori[245] conducted MD simulations to study the water/CO_2/alkane mixtures at 10 MPa and 350 K. They reported that the

hydrogen bonds between water and CO_2 account for CO_2 adsorption and the IFT reduction of the water/oil interface. In addition, Sun and co-workers[246-249] applied MD simulations to study the alkane/water and alkane/brine systems in the presence of CO_2 at pressures up to 200 MPa. Their results suggest that as the pressure increases, the water-oil IFT slightly increases with the same amount of CO_2, which is consistent with the experimental report[250]. In addition, their simulation results indicated that the water salinity affected the solubility of CO_2 in the water-rich phase. For example, as the salinity increases, the solubilities of CO_2 decrease in the water-rich phase. However, the interfacial properties such as IFT, CO_2 adsorption at the interface, and CO_2 orientation at the interface were not explicitly affected by salinity. Mohammed and Mansoori[251] conducted MD simulations to study the effect of supercritical CO_2 on the interfacial properties of a water-oil system with the heaviest oil fraction (asphaltene) at 10 MPa and 350 K. They found that the aromatics, CO_2, and asphaltenes accumulated at the water-oil interface with low CO_2 concentrations. As CO_2 concentration increased, CO_2 displaced the aromatics and asphaltenes away from the interface and into the bulk oil phase.

In this chapter, different from previous studies on pressure above 10 MPa, MD simulations were performed to study the CO_2/water/oil mixtures at 345 K and 8 MPa. Compared with previous studies, this chapter focused on low-pressure CO_2 with varying molar factions and its effect on the water-oil IFT. This study is important for the in-situ CO_2 generation EOR method as the CO_2-generating agents are usually injected well under 10 MPa. By analyzing the properties of the interface region and studying how CO_2 concentration would affect the adsorption amount, the molecular orientation, and the

interaction energy between oil and water, this chapter provided a molecular-level understanding of CO_2 contribution to EOR by the IFT reduction.

6.2 Simulation Details

Fakher and Imqam[252] compiled more than 200 laboratory experiments and 20 field tests of supercritical CO_2 flooding and showed that immiscible CO_2 injection had been the most frequently used EOR. According to their study, the most frequent oils used in experiments and tests have molecular weights above 500 g/mol, and the second oil MW frequency is between 80.7 to 200 g/mol. However, when the oil MW is more than 500 g/mol, their molecular structures and atomic compositions have too many uncertainties to handle by the MD method. Furthermore, even for high molecular weight oils, the mixture molecular weight in the reservoir could be significantly less given the natural gas solution. Therefore, the oil used in my binary and ternary systems would be selected from C6-C16 alkane groups.

Moreover, it was found that the IFT between water and different alkanes (C6, C10, C12, C16) when the pressure is less than 30 MPa is very similar, and the largest difference was smaller than 5 mN/m[246, 247]. Therefore, this chapter only used n-octane representing the oil, and I believed it could be used to study the IFT. Furthermore, the choice of hydrocarbon is also aligned with laboratory experiments on the IFT study for EOR purposes[253, 254].

LAMMPS was utilized for MD simulations of two systems in this chapter: (a) the binary system of CO_2/oil at pressures of 2, 4, 6, and 8 MPa and a temperature of 345 K; For the binary system, the CO_2 solubility in the oil was calculated under those four pressures and was compared with experimental data to validate the simulation setup and force field details. (b) the ternary system of CO_2/oil/water at a pressure of 8 MPa and temperature of

345 K. For the ternary system, interface properties such as IFT, molecular orientation, and CO_2 adsorption behaviors were studied as a function of the CO_2 concentration. The solubility of CO_2 in the oil calculated from the binary system at 8 MPa was used to decide the CO_2 concentration employed in the ternary system.

United-atom TraPPE force field was used to model n-octane. The TraPPE force field has been developed and successfully applied to describe alkane systems[255]. EPM2[256, 257], and TIP3P[258] were adopted to model CO_2 and water, respectively. The PPPM method was used for the long-range electrostatic interactions. The 12-6 Lennard-Jones potential treated the non-bonded van der Waals interactions.

The simulation of the binary system was initialized by placing 2000 CO_2 molecules on the right side and 2000 n-octane molecules on the left side of a simulation box. The simulation box had a length of 5.2 nm and a width of 5.2 nm. The height of the simulation box was set as 19.02 nm, 9.42 nm, 6.22 nm, and 4.62 nm for 2, 4, 6, and 8 MPa, respectively. The 20 ns simulation with NVT ensemble was applied at first to the system to reach its equilibrium state, where the size of the simulation box, the simulation temperature, and the number of atoms were fixed during the simulation. Then, another 5 ns simulation was applied to collect the data. Pu *et al.*[259] used an NVT ensemble on their CO_2/n-octane binary system to determine the CO_2 solubility in n-octane at 343.15 K, and their simulation value was consistent with the experimental value. I also utilized the NVT ensemble for binary systems. But it is worth pointing out that NVT and NPT ensembles shall provide identical results for sufficiently long MD simulations. Therefore, there is no advantage to using the NVT ensemble. During the simulation, periodic boundary conditions were employed in all three spatial directions. The leapfrog algorithm with a

timestep of 1 fs was implemented. **Figure 41(a)** shows the equilibrium state of the binary system.

The simulation of the ternary system was initialized by placing 2000 n-octane molecules in the middle and 1000 water molecules on each side of a simulation box. Apart from the water and n-octane molecules, the different numbers of CO_2 molecules were randomly placed in the simulation box to represent the different concentrations of CO_2 in the ternary system. The simulation box had an initial length of 5.5 nm and a width of 5.5 nm. The height of the simulation box was initially set as 50 nm for all different concentrations of CO_2. The 20 ns simulation with NPT ensemble was applied to the ternary system to reach its equilibrium state, where the number of atoms, the simulation pressure, and the simulation temperature was fixed during the simulation. After a 20 ns equilibration run, another 5 ns simulation with NVT was applied to collect the data. Periodic boundary conditions were employed in all three spatial directions of the simulation box during the simulation. Finally, the leapfrog algorithm with a timestep of 1 fs was implemented. **Figure 41(b)** shows the equilibrium state of the ternary system along with the Z direction.

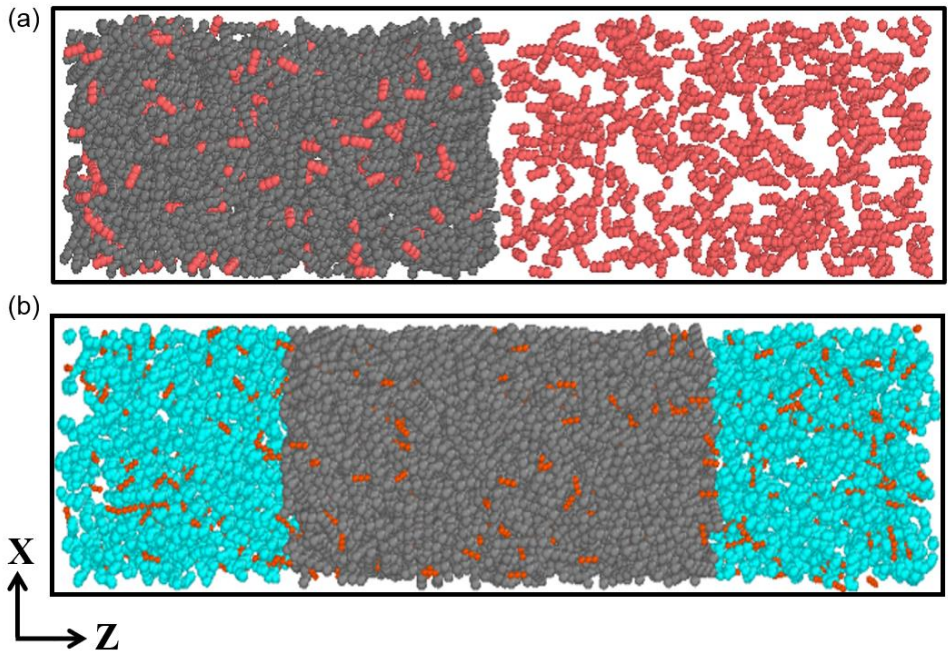

Figure 41. (a) The equilibrium state of the binary system at 8 MPa and 345 K: Grey, n-octane; Red, CO_2;(b) The equilibrium state of the ternary system at 8 MPa and 345 K: Grey, n-octane; Red, CO_2; Blue, water.

6.3 Interfacial Properties Computation

The interfacial tension between the water and n-octane in the ternary system was calculated through the Gibbs IFT formulation[260]:

$$r = -\frac{1}{2}\left(\frac{P_{xx}+P_{yy}}{2} - P_{zz}\right)L_z \tag{6.1}$$

where L_z is the length of the simulation box along the z-direction. P_{xx}, P_{yy}, and P_{zz} are three diagonal elements of the pressure tensor. The coefficient $\frac{1}{2}$ represents the two existing interfaces. As illustrated in **Figure 41(b)**, two interfaces exist in the ternary system, perpendicular to the z-direction.

The orientational order parameter (S) of CO_2 molecules was also calculated, which could describe the preferential orientation of CO_2 molecules as the function of their positions along the z-direction[261]:

$$S = \frac{1}{2} < 3cos^2(\theta) - 1 > \quad (6.2)$$

The θ was defined as the angle between the centerline of the CO_2 molecule with the z-direction.

6.4 Results and Discussions

6.4.1 Binary System

To determine the solubility of CO_2 in n-octane, the number density profile of n-octane and CO_2 along the z-direction was calculated, respectively. For example, at 8 MPa, the number density profile of the binary system is shown in **Figure 42(a)**. In this density profile, the right boundary of the interface region between CO_2 and n-octane could be determined when the n-octane density is zero in the CO_2 phase. The left boundary is where the local density of CO_2 is larger than its bulk density. The previous study[259] indicated that the CO_2 molecules could accumulate at the interface between CO_2 and n-octane. Thus, it was expected that a larger CO_2 density should be in the interface region. The number of CO_2 and n-octane molecules in the region I was used to calculate the CO_2 solubility in n-octane. The CO_2 solubilities in n-octane at different pressures are shown in **Table 7** and compared with the results from the previous studies in **Figure 42(b)**[262, 263]. The relative errors to the experimental and simulation results are also shown in **Figure 42(b)**. It is worth noting that the experimentally measured gas solubilities in hydrocarbons have relative errors from 10% to 35%[264].

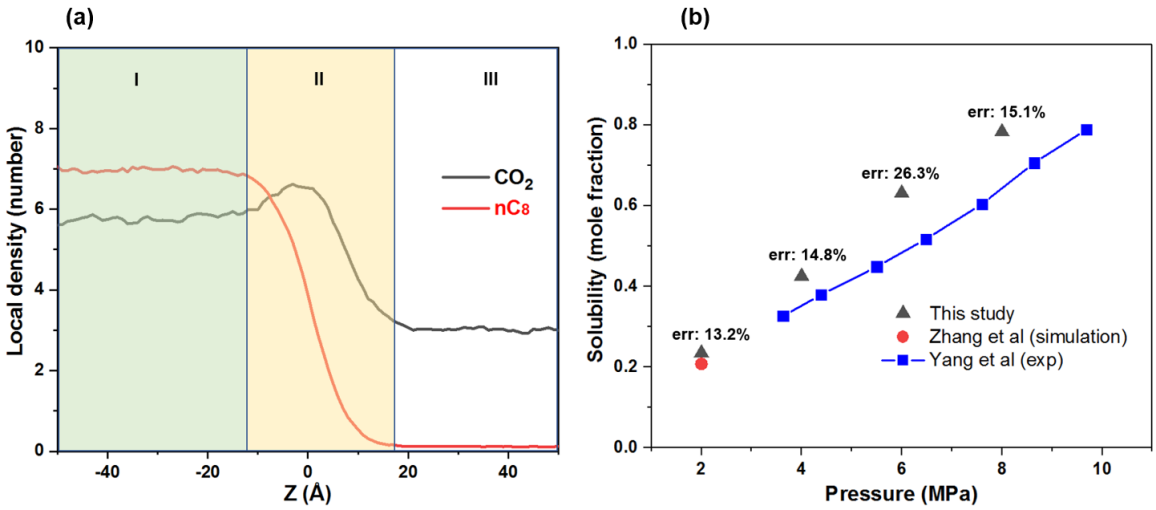

Figure 42. (a) Region I: the n-octane rich phase. Region II: the CO_2/n-octane interface region. Region III: the CO_2-rich phase. (b) the solubilities of CO_2 are around 350 K with different pressures reported in previous studies and this study.

Table 7. The values of CO_2 solubility in n-octane at different pressures with 345 K.

Pressure (MPa)	2	4	6	8
Solubility (mole fraction)	0.235	0.425	0.631	0.783

6.4.2 Ternary System

To construct the ternary system, 2000 water and 2000 n-octane molecules were mixed with the different mole fractions of CO_2 molecules. As shown in chapter 6.4.1, the solubility (mole fraction) of CO_2 in n-octane is 0.783 at 345 K and 8 MPa. Under the same condition, the solubility of CO_2 in water is reported to be 0.015[265]. Therefore, in this chapter, the mole fraction of CO_2, X_{CO2}, in the ternary system was defined as:

$$X_{CO2} = \frac{X^o_{CO2} + X^w_{CO2}}{N^o} \quad (6.3)$$

Where X^o_{CO2} *and* X^w_{CO2} are the number of CO_2 molecules in octane and water, respectively, and N^o is the total number of octane molecules. 11 ternary systems have been constructed accordingly for MD simulations, with CO_2 mole fractions of 0%, 6.5%, 11.5%, 21.5%, 26.5%, 36.5%, 46.5%, 51.5%, 61.5%, 70%, and 79.8%. The maximum CO_2 mole fraction

is 0.798: 0.783 of CO_2 in n-octane, see **Table 7**, and 0.015 of CO_2 in water (written as 79.8% concentration). The minimum CO_2 mole fraction is 0.065: 0.05 of CO_2 in n-octane and 0.015 of CO_2 in water (written as 6.5% concentration). Lake *et al.*[266] concluded that the injected volume of CO_2 into the reservoir could be in the range between 25-60% pore volume(PV), commonly around 30% PV. By considering residual oil saturation, the maximum CO_2 mole fraction of 0.798 I set in the ternary system is reasonable.

Similar to **Figure 42**, the ternary system is divided into three regions according to the density profile. The density profile analysis is shown in **Figure 43** for the ternary system with a 61.5% CO_2 concentration. The location of the interface was defined through the Gibbs Dividing Surface (GDS)[267], where the excess oil molecules in the water-rich region equal the number of excess water molecules in the oil-rich region. In addition, the interfacial width is determined by the "90%-0%" rule. The right and left boundaries are where water density equals 90% and 0% of bulk water density.

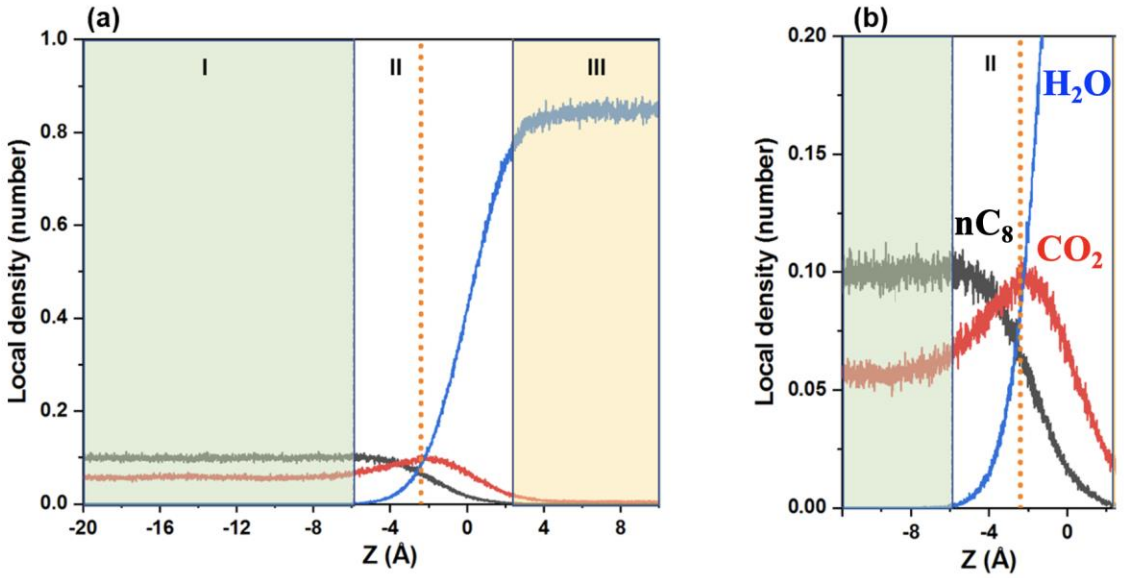

Figure 43. (a) The density profile of the ternary system with 61.5% CO_2 at 345 K and 8 MPa: n-octane (black), CO_2 (red), and water (blue). The orange dashed line indicates the

GDS interface. Regions I, II, and III correspond to the n-octane-rich phase, the interface, and the water-rich phase, respectively. (b) the zoom-in density profile, where CO_2 has a higher density in the interface region.

Figure 43 demonstrates that the CO_2 density reaches the maximum in the interface region. The Gibbs Dividing Surface could help identify where CO_2 molecules accumulate. This preferential accumulation (or adsorption) holds for all studied CO_2 concentrations. The density profile for different CO_2 concentrations has been analyzed in **Figure 44(a),** where the CO_2 accumulation is observed in the interface region for all calculated cases. To quantify such preference, the CO_2 density in the interface region was calculated and compared with bulk CO_2 density. **Figure 44(b)** reveals that the interface region expands as the overall CO_2 mole fraction increases. This confirms the EOR basic principle that the n-octane could be separated from water by adding adequate CO_2 molecules.

Meanwhile, the interfacial CO_2 density increases as more CO_2 molecules are added to the same n-octane/water mixture. **Figure 45** illustrates the configuration details of the interface region for low, medium, and high initial CO_2 mole fractions. As CO_2 concentration increases, the number of CO_2 molecules in the interface region also increases.

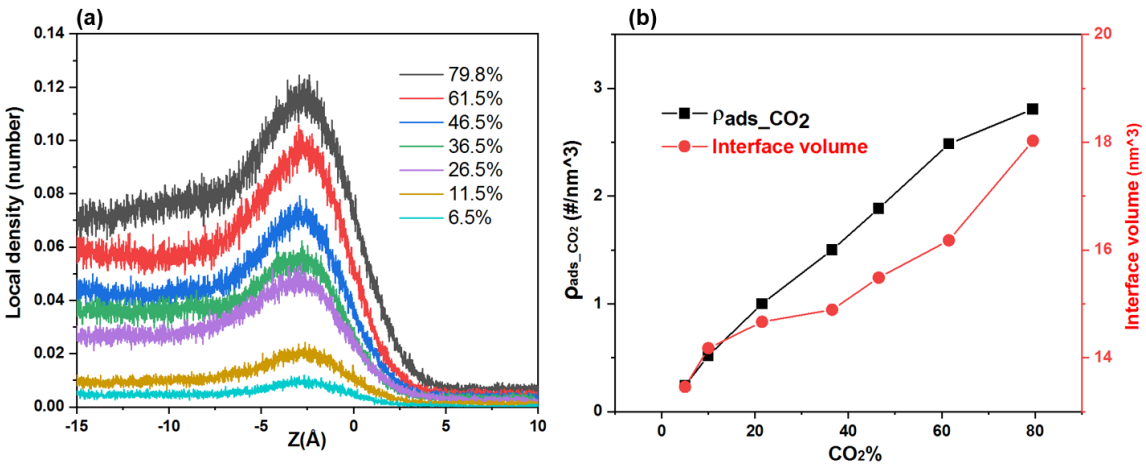

Figure 44. (a) the CO_2 density profiles with different CO_2 concentrations at 8 MPa and 345 K. (b) the density of adsorbed CO_2 molecules in the interface region and the volume of the interface region as a function of CO_2 concentration.

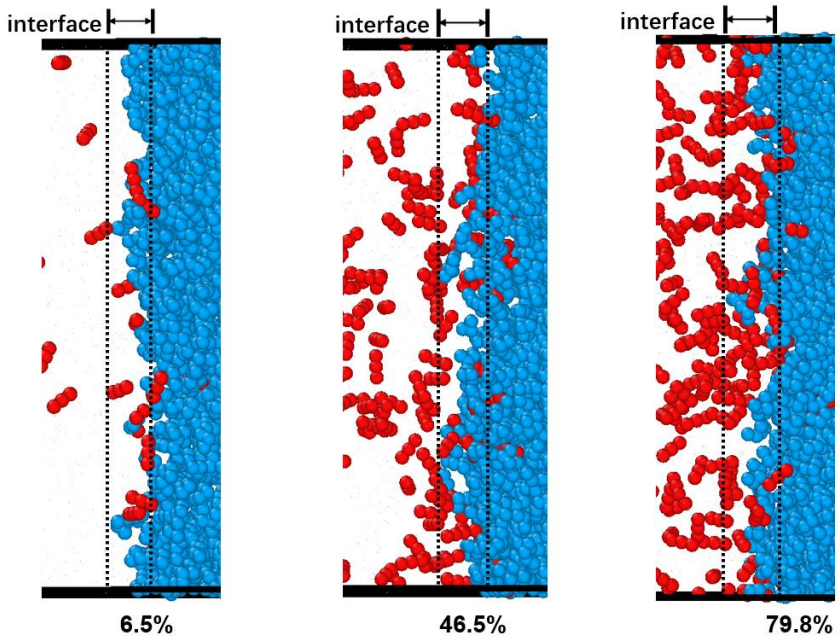

Figure 45. The configuration details of the interface region with low, medium, and high CO_2 concentrations. The dashed lines define the boundaries of the interface region. CO_2: red; H_2O: blue. N-octane molecules are not shown for clarity.

Figure 46 illustrates the n-octane/water interfacial tension, the density of accumulated (adsorbed) interfacial CO_2 molecules, and the intermolecular interaction energy between

n-octane and water in the interface region from those studied 11 ternary systems. As defined in the 12-6 LJ potential, when the distance between two non-bonded atoms (r) is larger than the zero-crossing distance for the potential (σ), the intermolecular interaction energy would be the attractive negative interaction. Thus, the observed negative intermolecular interaction energy suggests the attraction force between n-octane and water in the interface region. The such attractive force decreases as CO_2 concentration increases. This is because when more CO_2 molecules get adsorbed at the interface, they generally increase the distance between water and n-octane molecules, which weakens the interaction between n-octane and water. Therefore, the decrease in n-octane/water interaction is responsible for the IFT decrease, as indicated by the black curve in **Figure 46**. As shown in **Figure 47**, the intermolecular interaction energies between CO_2-octane and CO_2-water have also been determined as a function of CO_2 concentration, both of which increase when the CO_2 concentration increases. Since the solubility of CO_2 in n-octane is larger than that in water, more CO_2 molecules are dissolved in the oil-rich phase, causing a larger increase in the intermolar interaction between CO_2 and n-octane.

Similarly, the slight increase in the intermolar interaction between CO_2 and water is attributed to more adsorbed CO_2 molecules at the interface when the CO_2 concentration increases. Since the pressure effect on the water-oil IFT is very small, the water/n-octane IFT was compared with an experimental value[268] at 3.45 MPa and 338.15 K to validate the reliability of IFT values calculated in this chapter. The water/n-octane IFT without CO_2 is about 49 mN/m, which is consistent with the experiment value of 47 mN/m.

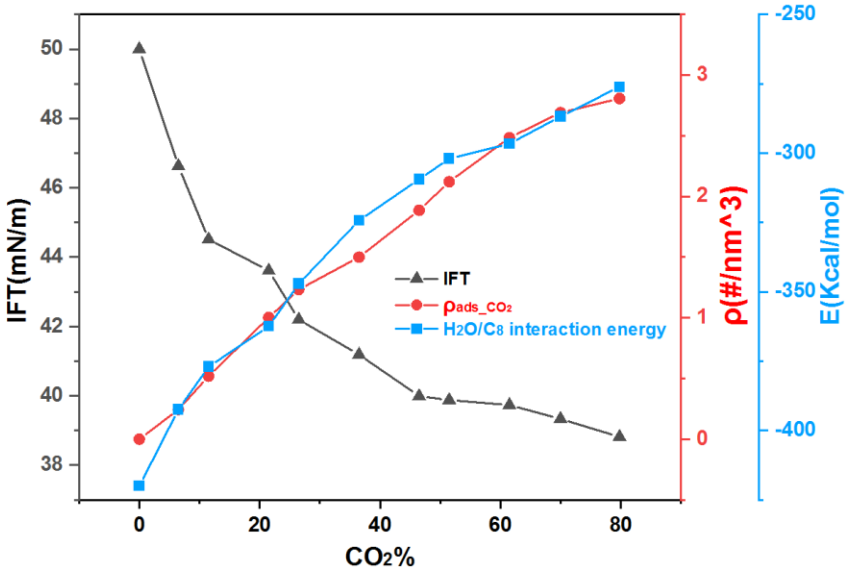

Figure 46. The interfacial tension (IFT, black), the density of adsorbed CO2 (red), and the interaction energy of n-octane and water (blue) for all studied 11 ternary systems.

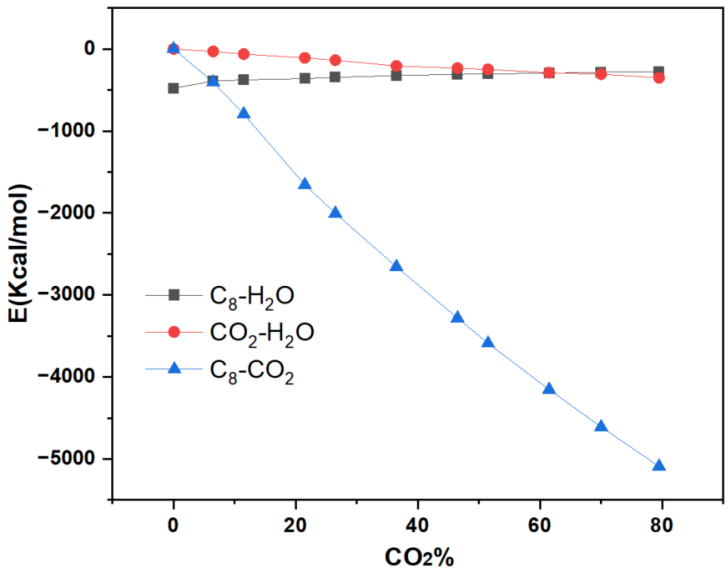

Figure 47. The intermolecular interaction energy between different molecules versus CO_2 concentration.

In **Figure 48(a)**, two linear functions were used to fit the IFT curve and indicate the rate of the IFT change. The slopes indicate about 10 mN/m reduction from 0% to 40%

concentrations, followed by about 2 mN/m decrease from 40% to 80% concentrations. To describe this phenomenon, the density profile of the ternary system with 61.5% CO_2 concentration was analyzed, as shown in **Figure 48(b)**. The likely reason is that the first contact region (region A) exists between n-octane and water that dominates the water/n-octane IFT. Region A was gradually filled with the adsorbed CO_2 as CO_2 concentration increased from 0-40%, significantly decreasing the water/n-octane IFT. However, with around 40% concentration, region A was almost saturated with the adsorbed CO_2 molecules. Further increasing the CO_2 concentration (40%-80%) couldn't effectively decrease the water/n-octane IFT. The visualization of region A in the interface region is displayed in **Figure 49**. The results in **Figure 50** show the pressure effect on the water-oil IFT with a specific CO_2 concentration. The data points in **Figure 50** are collected from 3 MD simulation studies[246-248] and 3 experimental studies[242, 250, 269]. Those results suggest that the pressure effect on water-oil IFT is small. The largest difference between these data points is around 5 mN/m. Therefore, it could be concluded[242, 246-248, 250, 269] that the pressure effect on water-oil IFT below 10 MPa is negligible and that the model in **Figure 48(a)** could be used to describe the water-oil IFT with CO_2 presence under low-pressure conditions below 10 MPa.

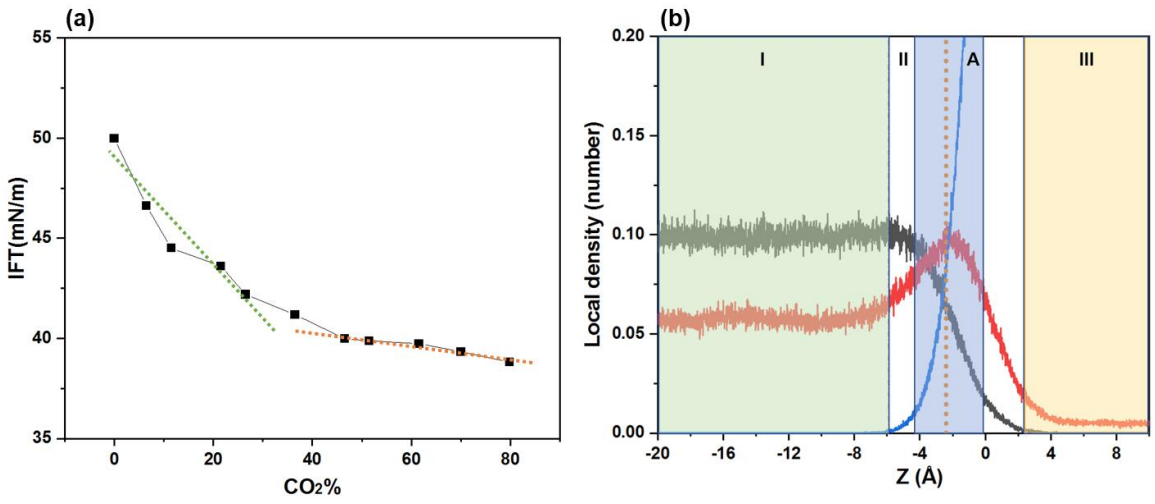

Figure 48. (a) The fitted IFT curve for studied CO_2 concentrations. (b) The density profiles of the ternary system with 61.5% CO_2 concentration: n-octane, black; CO_2, red; water: blue. The GDS is illustrated by the orange dashed line. Regions of I, II, and III represent the n-octane-rich phase, the interface, and the water-rich phase, respectively. Region A, a subsection of the interface region, illustrates the initial contact of water and n-octane.

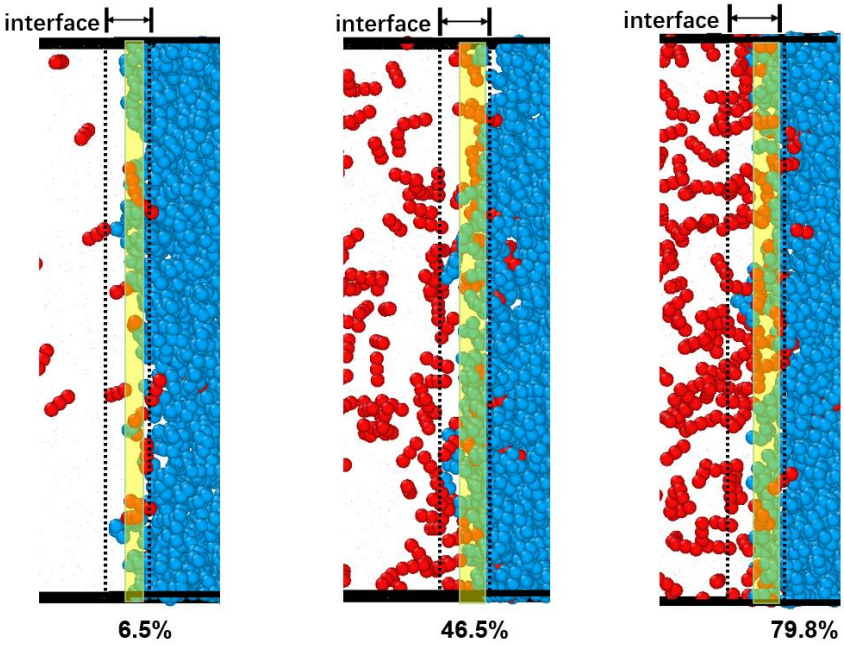

Figure 49. Configurations of n-octane/water interface region with different CO_2 concentrations. Two dash lines define the boundaries of the interface region. CO_2: red; H_2O: blue. N-octane molecules are not shown for clarity. The yellow color region defines Region A.

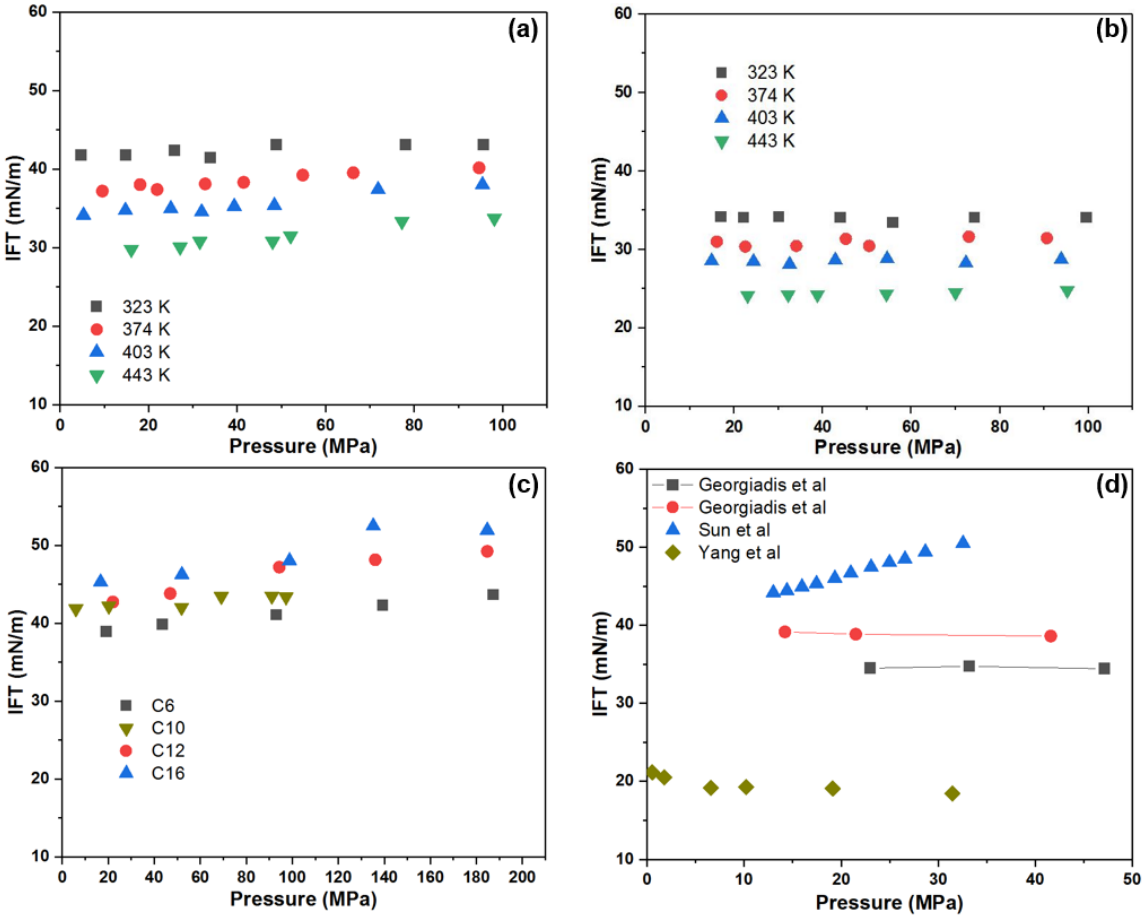

Figure 50. (a) CO_2/decane/water system with a 0.5-mole fraction of CO_2 under different temperature conditions. [248] (b) CO_2/decane/water system with a 0.8-mole fraction of CO_2 under different temperature conditions[248]. (c). CO_2/alkane/water system with CO_2/alkane ratio = 1:1. C6, C12, and C16 data points were simulated at 374 K[247]. C10 data points were simulated at 323 K[246]. (d) Laboratory data [242]: H_2O+(0.5 n-decane+0.5 CO_2) system with black square symbol; H_2O+(0.8 n-decane+0.2 CO_2) system with red circle symbol, Sun *et al.* [250]: H_2O+(0.659 oil+0.341 CO_2) system, and Yang *et al.*[269]: H_2O+(oil+CO_2 saturated) system.

6.4.3 Molecular Orientation

The orientation order parameter S(θ) of CO_2 molecules was calculated to show its preferential orientation along the Z-direction in the binary and ternary systems. Eqn (6.2) shows that the S value approaching -0.5 would indicate that CO_2 molecules prefer to be parallel to the interface. While the S value approaching the unity would indicate that CO_2

molecules are perpendicular to the interface. For the random orientation, the S value would be zero.

Both the order parameter and the density profiles of CO_2 molecules are shown in **Figure 51(a)**. The S value was about zero for the Z direction, which indicates that CO_2 molecules are randomly orientated along the Z direction for the binary CO_2/n-octane system. For the ternary system of 61.5% CO_2 concentration, as illustrated in **Figure 51(b)**, the S value of CO_2 is almost zero in both the water-rich and n-octane-rich regions. However, the S value is about -0.07 for the interface region, suggesting a preferential orientation of CO_2 molecules in this region.

To further understand CO_2 orientation in the interface region, the S value for different CO_2 concentrations was analyzed and presented in **Figure 52**. As CO_2 concentration increases, the S value for the interface region becomes more negative, suggesting the parallel orientation of CO_2 molecules. Interestingly, for higher CO_2 concentrations, namely, 46.5%, 61.5%, and 79.8%, the S values are similar (~ -0.06) for those ternary systems. This observation is consistent with the previous IFT analysis in **Figure 48(a)**. Thus, it could be concluded that once the contact region of n-octane/water has been saturated with CO_2, no more CO_2 could be adsorbed. Thus, there shall be little change to the CO_2 orientation and the IFT. The orientation analysis in **Figure 52** also reveals that the change in CO_2 concentration affects CO_2 orientation near the interface, which is a fundamental descriptor of the IFT change.

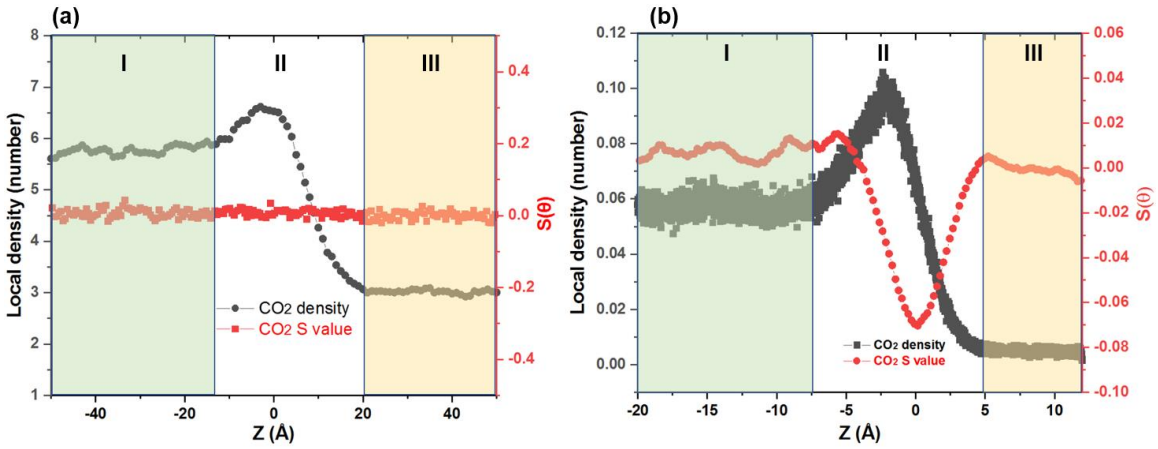

Figure 51. (a) Region I: the n-octane rich phase; Region II: the CO_2/n-octane interface; Region III: the CO_2-rich phase. (b) Region I: the n-octane rich phase; Region II: the water/n-octane interface; Region III: the water-rich phase.

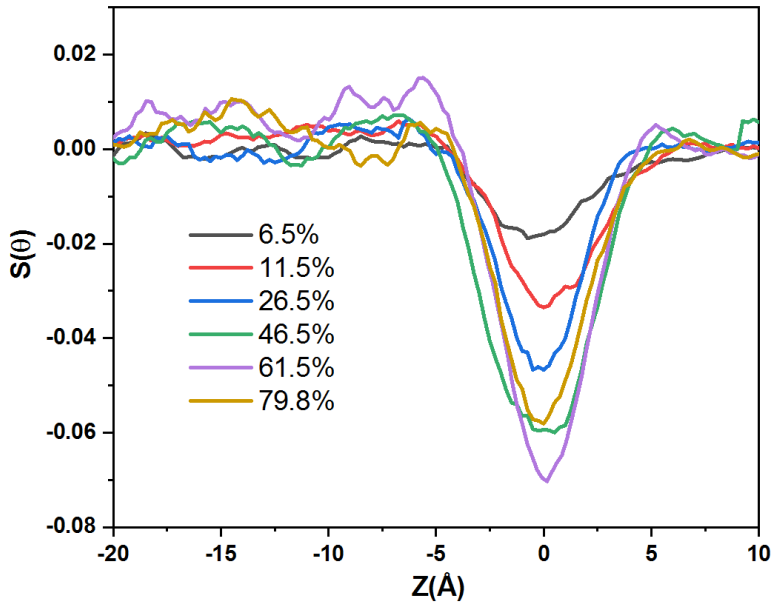

Figure 52. CO_2 orientational profiles for ternary systems of different CO_2 concentrations.

6.5 Conclusions

MD simulations have been performed in this chapter to understand the n-octane/water interfacial properties with the addition of CO_2. The water/n-octane interfacial tension, the adsorption, and the orientation of CO_2 have been analyzed as a function of the

CO_2 mole fraction. The simulation results demonstrate that the CO_2 mole fraction of 0.4 is required to reduce the water/n-octane interfacial tension. Because the water/n-octane IFT significantly decreases when the CO_2 concentration is between 0% and 40%. While at higher CO_2 concentrations of 40% to 80%, the IFT reduction is small. My literature survey did not show any similar observations in past studies. The analysis of CO_2 molecule orientation adds a different understanding to the water/n-octane interface. At low CO_2 concentrations of 0~40%, CO_2 molecules would change the orientation from the random distribution to parallel to the water/n-octane interface. Once the contact region of water/n-octane has been saturated by CO_2 molecules, increasing the CO_2 concentrations does not change much of the IFT or CO_2 orientation. From the molecular perspective, interfacial CO_2 orientation is affected by bulk CO_2 concentration and is closely correlated to the IFT change of those studied ternary systems.

Chapter 7: Conclusions and Suggested Future Work

7.1 Conclusions

MD simulations were performed to study multiple hydrocarbon component systems and their fundamental mixing behaviors and compute important application parameters. The applications include rejuvenating aged asphalts with waste cooking oil, waste polyethylene, and CO_2 EOR. The main conclusions are summarized as follows.

(1). A new aged asphalt model was constructed in this dissertation. A central feature of this new asphalt model is the consideration of oxidation chemistry and reported functional group concentrations since the properties of asphalt are known to be significantly related to the amounts of functional groups. Model oxidation compounds include proposed representative asphalt structures based on Peterson's dual reaction pathways for the degradation of benzylic hydroperoxide intermediates while taking the observed product distribution of cumene oxidation into account. Other oxygen-containing functional groups, such as anhydrides, carboxylic acids, and polynuclear aromatics, have been incorporated to account for the critical physical characteristics of aged asphalt. By extending the molecular basis set of asphalt components developed in this new model, the researchers could now construct more realistic models to represent varying SARA content, different oxidation levels, and functional group composition.

(2). The main component of WCO could decrease the viscosity and increase the self-diffusion coefficient of the aged asphalt at 404 K and 1 atm. The TG significantly weakens the molecular interaction between asphaltenes and

mitigates their aggregations formed in aged asphalt, which is why the TG could decrease the viscosity and increase the self-diffusion coefficient of the aged asphalt. However, the mitigation effect of TG on the formation of asphaltene aggregation is limited.

(3). At 298 K and 1 atm, the PE preferentially interacts with the maltenes in the aged asphalt, weakening the interactions between asphaltenes and maltenes. The MAH functional group grafted on PE improves the compatibility between PE and aged asphalt because it enhances the interaction between asphaltenes and PE. Besides, the MAH functional group enhances the interactions between asphaltenes-saturates and asphaltenes-aromatics. Last but not least, PE and PE-g-MAH couldn't affect the interactions between asphaltenes-asphaltenes and mitigate the formation of asphaltene aggregations in aged asphalt. By comparing the phase separation of PE-modified asphalt observed in my MD simulation and reported from previous experimental studies, a new point of view is that if the PE used to modify the asphalt has a small MW and short-enough chain length, the phase separation likely could be avoided.

(4). In CO_2-EOR techniques, the water-oil IFT reduction is an important oil recovery mechanism as it affects the endpoint mobility of oil. The research shows that under low-pressure conditions (< 10 MPa) with 345 K, the CO_2 concentration of 40% (0.4 mole fraction in the oil and water phases totally) is required to reduce the water/oil interfacial tension tangibly as the IFT change in a bilinear fashion. The IFT reduces relatively fast when the CO_2 concentration increases to 40%. After that, the IFT reduction is much slower.

(5). The CO_2 molecule orientation can fundamentally explain the relationship between water/oil IFT and CO_2 concentration. When CO_2 concentrations are between 0 and 40%, CO_2 molecules change the orientation from the random distribution to parallel to the water/n-octane interface and significantly decrease the water/oil IFT. Once the interface is saturated by CO_2 molecules at around 40% concentration, increasing the CO_2 concentration does not change much of the CO_2 orientation at the interface and water/oil IFT.

(6). The relationship between water/oil IFT and CO_2 concentration could be directly implemented in the numerical reservoir simulator (like CMG) to quantify the contribution of water/oil IFT reduction to oil recovery in CO_2 EOR under pressure conditions below 10 MPa.

7.2 Future Work

The following recommendations should be considered for future work.

(1). Several methods have been developed to compute the shear viscosity of fluid via MD simulation. They fall into equilibrium molecular dynamics (EMD) and nonequilibrium dynamics (NEMD). The GK method is the most widely used EMD method, and the SLLOD algorithm is the typical NEMD method. In Chapter 4, EMD-GK and NEMD-SLLOD methods have been used to determine the shear viscosity of asphalt models. In **Figure 53,** the values of shear viscosity determined from other MD simulation studies around 400 K [103, 104, 172, 182, 184, 186, 270, 271] are listed, all of which are relatively smaller than the experimental values[41, 51, 52, 184, 272-274], at least one order of magnitude underestimation. Different SARA fractions of asphalt samples tested in the

simulations and experiments are one of the reasons causing such a significant difference.

In addition, the methods used in these simulation studies are GK, SLLOD, and Muller-Plathe methods. The limitations of the GK and SLLOD methods have already been discussed in Chapter 4, which can be the reasons causing such a significant difference. The Muller-Plathe method is a reverse nonequilibrium method that reverses the cause-and-effect theory from the nonequilibrium method. In the SLLOD method, the "cause'' is the imposed velocity gradient, and the "effect" is the momentum flux measured through off-diagonal elements of the stress or pressure tensor. While in the Muller-Plathe method, it imposes the momentum flux("cause") on the system and forms the shear rate or velocity profile("effect") to estimate the viscosity. The shortcoming of the Muller-Plathe method is that at high momentum flux, the velocity profile shows significantly non-linearity, which leads to low accuracy of viscosity prediction[275].

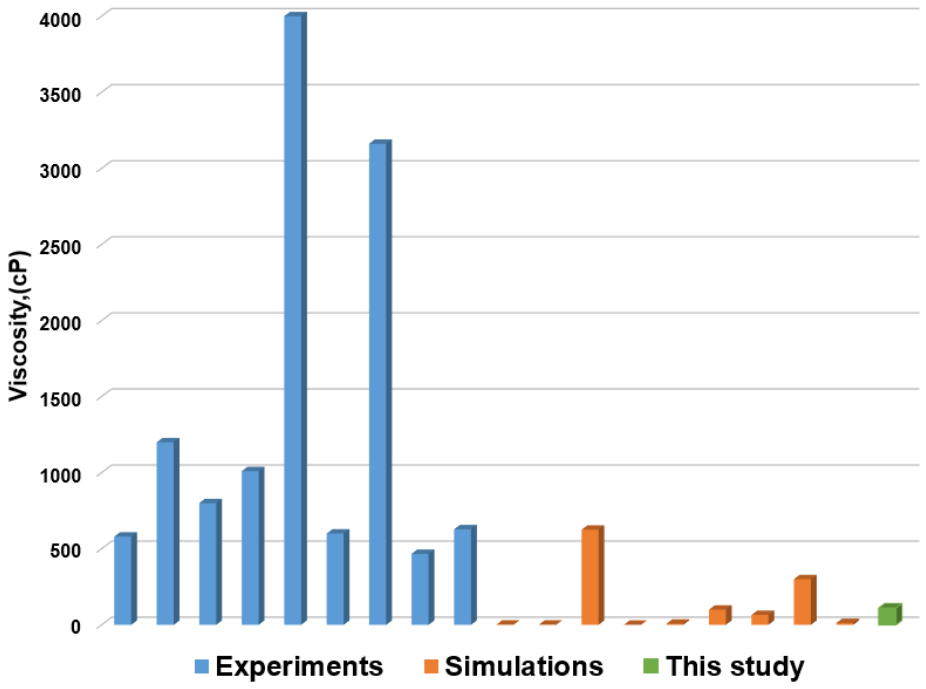

Figure 53. Reference viscosities reported from the MD simulations and experiments. Under similar pressure and temperature conditions, most of the viscosities determined via MD simulation are much smaller than those determined in the laboratory, except for the viscosity determined from Simulation-3.

To find or develop new methods that can narrow the difference between the viscosities determined by MD simulation and experiment is necessary. For example, in the GK method, Van-Oanh *et al.*[181] found that the viscosity convergence plateau can be reached only if the correlation length is much longer than the relaxation time of the system. Zhang and Greenfield[182] found the relaxation time of their asphalt system is about 7.5×10^3 ns at 358.15 K and about 0.24 ns at 443.15 K. However, 7.5×10^3 ns is too long for MD simulation to achieve. Thus, they point out that the GK method can only accurately predict the shear viscosity of asphalt systems at high temperatures. Therefore, in simulation 3, Li and Greenfield directly used the GK method to

predict the viscosity of their asphalt system at 533.15 K and then applied the Debye-Stokes-Einstein (DSE) theory to predict the viscosity at 400.15 K based on the viscosity and reorientation relaxation time determined at 533.15 K. The DSE theory can be used to relate molecular reorientation relaxation time and viscosity for temperatures above the glass transition temperature[276]. **Figure 53 shows** that the viscosity predicted by DSE theory is relatively consistent with experiment data around 400 K. In the future DSE should be tried.

(2). The ICE method resolves traditional supercritical CO_2 injection issues such as CO_2 availability, high transportation cost, and infrastructure investment. Therefore, it potentially be very attractive for thousands of stripper wells that produce oil on marginal economic feasibility. Previous efforts mainly focus on laboratory tests and mechanisms study. The actual field performance of this technology is likely dependent on reservoir heterogeneity and its economic viability is expected to be closely related to its optimization. Sadma *et al*.[277] used CMG to study the field performance of ICE and quantify the contributions to oil recovery factors from several plausible mechanisms.

However, in their study, the relative permeability remained the most uncertain parameter during history matching and modeling the ICE synergetic mechanisms. The relative permeability curve varies with the IFT change between water and oil due to CO_2 adsorption and in-situ surfactant produced at the water-oil interface. The relationship between water-oil IFT with the amount of CO_2 adsorption could be described by the study published by Chang *et al*[278].

In contrast, the effect of in-situ surfactant produced from the reaction between ammonia and oil acid has not been studied and needs to be done in the future.

(3). The difference truly existed between the microstructure of PE-modified asphalt simulated via MD simulation and observed from experiments, which may result in the difference between macroscopic properties of PE-modified asphalt determined from MD simulation and experiment. Developing a PE-modified asphalt model that could capture the nature of PE-modified asphalt is necessary for studying the PE-modified asphalt with MD simulation.

Nomenclature

ACF Autocorrelation function

AFM Atomic force microscopy

CED Cohesive energy density

EOR Enhanced oil recovery

HDPE High-density polyethylene

ICE In-situ CO2 enhanced oil recovery

IFT Interfacial tension

LDPE Low-density polyethylene

MAH Maleic anhydride functional group

MMP Minimum miscible pressure

MSD Mean-squared displacement

PE Polyethylene

PET Polyethylene terephthalate

PVC Polyvinyl chloride

PS Polystyrene

PP Polypropylene

RAP Reclaimed asphalt pavement

RDF Radial distribution function

SARA Saturates, Asphaltenes, Resins, Aromatics

SFE Surface free energy

TG Triglyceride

WCO Waste cooking oil

WPE Waste polyethylene

WPE-g-MAH Maleic anhydride grafted polyethylene

References

1. Jin, L.; He, Y.; Zhou, G.; Chang, Q.; Huang, L.; Wu, X., Natural gas density under extremely high pressure and high temperature: Comparison of molecular dynamics simulation with corresponding state model. *Chinese Journal of Chemical Engineering* **2021,** *31*, 2-9.
2. Qiao, Q.; Li, X.; Huang, L., Crystalline cellulose under pyrolysis conditions: the structure–property evolution via reactive molecular dynamics simulations. *Journal of Chemical & Engineering Data* **2019,** *65* (2), 360-372.
3. Hospital, A.; Goñi, J. R.; Orozco, M.; Gelpí, J. L., Molecular dynamics simulations: advances and applications. *Advances and applications in bioinformatics and chemistry: AABC* **2015,** *8*, 37.
4. Wang, S.; Huang, L.; Zhang, Y.; Li, L.; Lu, X., A mini-review on the modeling of volatile organic compound adsorption in activated carbons: Equilibrium, dynamics, and heat effects. *Chinese Journal of Chemical Engineering* **2021,** *31*, 153-163.
5. Abdo, A. A., Utilizing reclaimed asphalt Pavement (RAP) materials in new pavements-A Review. *International Journal of Thermal & Environmental Engineering* **2016,** *12* (1), 61-66.
6. Azahar, W. N. A. W.; Bujang, M.; Jaya, R. P.; Hainin, M. R.; Ngadi, N.; Abdullah, M. E.; Mohamed, A. A., A review on application of waste cooking oil as rejuvenator in porous asphalt mixture. *Jurnal teknologi* **2016,** *78* (4).
7. Ahmed, R. B.; Hossain, K., Waste cooking oil as an asphalt rejuvenator: A state-of-the-art review. *Construction and Building Materials* **2020,** *230*, 116985.
8. Kalantar, Z. N.; Karim, M. R.; Mahrez, A., A review of using waste and virgin polymer in pavement. *Construction and Building Materials* **2012,** *33*, 55-62.
9. Masad, E.; Roja, K. L.; Rehman, A.; Abdala, A., A review of asphalt modification using plastics: a focus on polyethylene. *Texas A&M University: Qatar, Doha* **2020**.
10. Grigg, R. B.; Schechter, D. S., State of the Industry in CO2 Floods. In *SPE Annual Technical Conference and Exhibition*, Society of Petroleum Engineers: San Antonio, Texas, 1997; p 7.
11. Markewitz, P.; Kuckshinrichs, W.; Leitner, W.; Linssen, J.; Zapp, P.; Bongartz, R.; Schreiber, A.; Müller, T. E., Worldwide innovations in the development of carbon capture technologies and the utilization of CO2. *Energy & Environmental Science* **2012,** *5* (6), 7281-7305.
12. Read, J.; Whiteoak, D., Shell Bitumen Handbook (5th Edition). ICE Publishing.
13. Jiménez-Mateos, J. M.; Quintero, L. C.; Rial, C., Characterization of petroleum bitumens and their fractions by thermogravimetric analysis and differential scanning calorimetry. *Fuel* **1996,** *75* (15), 1691-1700.
14. Speight, J. G., *The desulfurization of heavy oils and residua*. CRC Press: 1999.
15. Mortazavi, M.; Moulthrop, J. S., The SHRP materials reference library. **1993**.
16. Wiehe, I. A.; Liang, K. S., Asphaltenes, resins, and other petroleum macromolecules. *Fluid Phase Equilibria* **1996,** *117* (1), 201-210.
17. Corbett, L. W., Composition of asphalt based on generic fractionation, using solvent deasphaltening, elution-adsorption chromatography, and densimetric characterization. *Analytical Chemistry* **1969,** *41* (4), 576-579.
18. Mullins, O. C., The Modified Yen Model. *Energy & Fuels* **2010,** *24* (4), 2179-2207.
19. Roberts, F. L.; Kandhal, P. S.; Brown, E. R.; Lee, D.-Y.; Kennedy, T. W., Hot mix asphalt materials. *Mixture Design and Construction* **1996,** *2*.
20. Claudy, P.; Letoffe, J.; King, G.; Plancke, J., Characterization of asphalts cements by thermomicroscopy and differential scanning calorimetry: correlation to classic physical properties. *Fuel science & technology international* **1992,** *10* (4-6), 735-765.
21. Wang, J.; Wang, T.; Hou, X.; Xiao, F., Modelling of rheological and chemical properties of asphalt binder considering SARA fraction. *Fuel* **2019,** *238*, 320-330.

22. Jewell, D.; Weber, J.; Bunger, J.; Plancher, H.; Latham, D., Ion-exchange, coordination, and adsorption chromatographic separation of heavy-end petroleum distillates. *Analytical Chemistry* **1972,** *44* (8), 1391-1395.
23. Jewell, D. M.; Albaugh, E. W.; Davis, B. E.; Ruberto, R. G., Integration of chromatographic and spectroscopic techniques for the characterization of residual oils. *Industrial & Engineering Chemistry Fundamentals* **1974,** *13* (3), 278-282.
24. Suatoni, J.; Swab, R., Rapid hydrocarbon group-type analysis by high performance liquid chromatography. *Journal of Chromatographic Science* **1975,** *13* (8), 361-366.
25. Hayes, P. C.; Anderson, S. D., Quantitative determination of hydrocarbons by structural group-type via high-performance liquid chromatography with dielectric constant detection. *Analytical Chemistry* **1985,** *57* (11), 2094-2098.
26. Robbins, W. K., Quantitative measurement of mass and aromaticity distributions for heavy distillates 1. Capabilities of the HPLC-2 system. *Journal of chromatographic science* **1998,** *36* (9), 457-466.
27. Fan, T.; Buckley, J. S., Rapid and accurate SARA analysis of medium gravity crude oils. *Energy & Fuels* **2002,** *16* (6), 1571-1575.
28. Karlsen, D. A.; Larter, S. R., Analysis of petroleum fractions by TLC-FID: applications to petroleum reservoir description. *Organic geochemistry* **1991,** *17* (5), 603-617.
29. Jiang, C.; Larter, S. R.; Noke, K. J.; Snowdon, L. R., TLC–FID (Iatroscan) analysis of heavy oil and tar sand samples. *Organic Geochemistry* **2008,** *39* (8), 1210-1214.
30. Masson, J.; Price, T.; Collins, P., Dynamics of bitumen fractions by thin-layer chromatography/flame ionization detection. *Energy & Fuels* **2001,** *15* (4), 955-960.
31. Xu, G.; Wang, H., Molecular dynamics study of oxidative aging effect on asphalt binder properties. *Fuel* **2017,** *188*, 1-10.
32. Boysen, R.; Schabron, J., Laboratory and field asphalt binder aging: Chemical changes and influence on asphalt binder embrittlement. *Technical white papers of WRI* **2015**.
33. Qin, Q.; Schabron, J. F.; Boysen, R. B.; Farrar, M. J., Field aging effect on chemistry and rheology of asphalt binders and rheological predictions for field aging. *Fuel* **2014,** *121*, 86-94.
34. Petersen, J. C.; Materials, N. R. C. T. R. B. C. o. C. o. B., *A Review of the Fundamentals of Asphalt Oxidation: Chemical, Physicochemical, Physical Property, and Durability Relationships*. Transportation Research Board: 2009.
35. Lesueur, D., The colloidal structure of bitumen: Consequences on the rheology and on the mechanisms of bitumen modification. *Advances in Colloid and Interface Science* **2009,** *145* (1), 42-82.
36. Bell, C. A., *Summary report on aging of asphalt-aggregate systems*. Strategic Highway Research Program, National Research Council: 1989; Vol. 89.
37. Wang, Y.; Wen, Y.; Zhao, K.; Chong, D.; Wong, A., Evolution and locational variation of asphalt binder aging in long-life hot-mix asphalt pavements. *Construction and Building Materials* **2014,** *68*, 172–182.
38. Qu, X.; Oeser, M.; Radenberg, M. *Study of asphalt binder using molecular dynamics simulation*; Lehrstuhl und Institut für Straßenwesen: 2019.
39. Yuan, Q.; Liu, Z.; Zheng, K.; Ma, C., Chapter 7 - Asphalt. In *Civil Engineering Materials*, Yuan, Q.; Liu, Z.; Zheng, K.; Ma, C., Eds. Elsevier: 2021; pp 287-325.
40. Dokandari, P. A.; Kaya, D.; Sengoz, B.; Topal, A. In *Implementing waste oils with reclaimed asphalt pavement*, Proceedings of the 2nd World congress on civil, structural and environmental engineering (CSEE'17), 2017; pp 1-12.
41. Chen, M.; Leng, B.; Wu, S.; Sang, Y., Physical, chemical and rheological properties of waste edible vegetable oil rejuvenated asphalt binders. *Construction and Building materials* **2014,** *66*, 286-298.

42. Eriskin, E.; Karahancer, S.; Terzi, S.; Saltan, M., Waste frying oil modified bitumen usage for sustainable hot mix asphalt pavement. *Archives of Civil and Mechanical Engineering* **2017,** *17* (4), 863-870.
43. Joni, H. H.; Al-Rubaee, R. H. A.; Al-zerkani, M. A., Rejuvenation of aged asphalt binder extracted from reclaimed asphalt pavement using waste vegetable and engine oils. *Case Studies in Construction Materials* **2019,** *11*, e00279.
44. Li, H.; Dong, B.; Wang, W.; Zhao, G.; Guo, P.; Ma, Q., Effect of Waste Engine Oil and Waste Cooking Oil on Performance Improvement of Aged Asphalt. *Applied Sciences* **2019,** *9*, 1767.
45. Sang, Y.; Chen, M. Z.; Wen, J.; Leng, B. B.; Wu, S. P., Effect of Waste Edible Animal Oil on Physical Properties of Aged Asphalt. *Key Engineering Materials* **2014,** *599*, 130-134.
46. Somé, S. C.; Pavoine, A.; Chailleux, E., Evaluation of the potential use of waste sunflower and rapeseed oils-modified natural bitumen as binders for asphalt pavement design. *International Journal of Pavement Research and Technology* **2016,** *9* (5), 368-375.
47. Mahrez, A.; Karim, M. R.; Ibrahim, M. R.; Katman, H. Y. In *Prospects of using waste cooking oil as rejuvenating agent in bituminous binder*, Proceedings of the Eastern Asia Society for Transportation Studies Vol. 7 (The 8th International Conference of Eastern Asia Society for Transportation Studies, 2009), Eastern Asia Society for Transportation Studies: 2009; pp 289-289.
48. Sun, Z.; Yi, J.; Huang, Y.; Feng, D.; Guo, C., Properties of asphalt binder modified by bio-oil derived from waste cooking oil. *Construction and Building Materials* **2016,** *102*, 496-504.
49. Alcantara, R.; Amores, J.; Canoira, L.; Fidalgo, E.; Franco, M.; Navarro, A., Catalytic production of biodiesel from soy-bean oil, used frying oil and tallow. *Biomass and bioenergy* **2000,** *18* (6), 515-527.
50. Zaumanis, M.; Mallick, R. B.; Frank, R., 100% recycled hot mix asphalt: A review and analysis. *Resources, Conservation and Recycling* **2014,** *92*, 230-245.
51. Zargar, M.; Ahmadinia, E.; Asli, H.; Karim, M. R., Investigation of the possibility of using waste cooking oil as a rejuvenating agent for aged bitumen. *Journal of Hazardous Materials* **2012,** *233-234*, 254-258.
52. Ji, J.; Yao, H.; Suo, Z.; You, Z.; Li, H.; Xu, S.; Sun, L., Effectiveness of vegetable oils as rejuvenators for aged asphalt binders. *Journal of Materials in Civil Engineering* **2017,** *29* (3), D4016003.
53. El-Shorbagy, A. M.; El-Badawy, S. M.; Gabr, A. R., Investigation of waste oils as rejuvenators of aged bitumen for sustainable pavement. *Construction and Building Materials* **2019,** *220*, 228-237.
54. Gökalp, İ.; Uz, V., Utilizing of Waste Vegetable Cooking Oil in bitumen: Zero tolerance aging approach. *Construction and Building Materials* **2019,** *227*.
55. Xinxin, C.; Xuejuan, C.; Boming, T.; Yuanyuan, W.; Xiaolong, L., Investigation on possibility of waste vegetable oil rejuvenating aged asphalt. *Applied Sciences* **2018,** *8* (5), 765.
56. Sang, Y.; Chen, M. Z.; Wen, J.; Leng, B. B.; Wu, S. P. In *Effect of waste edible animal oil on physical properties of aged asphalt*, Key Engineering Materials, Trans Tech Publ: 2014; pp 130-134.
57. Gao, G.; Zhang, Y.; Zhang, Y.; Sun, K., Enhanced performance of LDPE/SBS blend modified asphalt through dynamic vulcanization. *Polymers and Polymer Composites* **2002,** *10* (6), 433-440.
58. Wang, X.; Zhang, Y.; Huang, B.; Chen, Z.; Zhong, M.; Wang, W.; Liu, X.; Fan, Y. n.; Hu, W., Atmospheric phthalate pollution in plastic agricultural greenhouses in Shaanxi Province, China. *Environmental Pollution* **2021,** *269*, 116096.
59. Dalhat, M. A.; Wahhab, H. I. A.-A.; Al-Adham, K., Recycled Plastic Waste Asphalt Concrete via Mineral Aggregate Substitution and Binder Modification. *Journal of Materials in Civil Engineering* **2019,** *31* (8), 04019134.

60. Reinke, G.; Glidden, S. In *Determination of Phosphorus in Asphalt Binders and in Binders Recovered from Bituminous Mixtures*, North East Asphalt User/Producer Group Meeting, 2007; pp 17-34.
61. Vargas, M. A.; Vargas, M. A.; Sánchez-Sólis, A.; Manero, O., Asphalt/polyethylene blends: Rheological properties, microstructure and viscosity modeling. *Construction and Building Materials* **2013,** *45*, 243-250.
62. Ho, S.; Church, R.; Klassen, K.; Law, B.; MacLeod, D.; Zanzotto, L., Study of recycled polyethylene materials as asphalt modifiers. *Canadian journal of civil engineering* **2006,** *33* (8), 968-981.
63. Punith, V.; Veeraragavan, A.; Amirkhanian, S. N., Evaluation of reclaimed polyethylene modified asphalt concrete mixtures. *International Journal of Pavement Research and Technology* **2011,** *4* (1), 1.
64. Babalghaith, A. M.; Koting, S.; Sulong, N. H. R.; Karim, M. R. In *Optimization of mixing time for polymer modified asphalt*, IOP Conference Series: Materials Science and Engineering, IOP Publishing: 2019; p 012030.
65. Otuoze, H. S.; Ejeh, S. P.; Amartey, Y. D.; Manasseh, J.; Shuaibu, A. A., Rheology and simple performance test (SPT) evaluation of high-density polypropylene (HDPP) waste-modified bituminous mix. *Jordan Journal of Civil Engineering* **2018,** *12* (1).
66. Cheng, Y.; Fu, Q.; Fang, C.; Zhang, Q.; Lu, C., Preparation, Structure, and Properties of Modified Asphalt with Waste Packaging Polypropylene and Organic Rectorite. *Advances in Materials Science and Engineering* **2019,** *2019*, 5362795.
67. Ziari, H.; Nasiri, E.; Amini, A.; Ferdosian, O., The effect of EAF dust and waste PVC on moisture sensitivity, rutting resistance, and fatigue performance of asphalt binders and mixtures. *Construction and Building Materials* **2019,** *203*, 188-200.
68. Cuadri, A. A.; Partal, P.; Ahmad, N.; Grenfell, J.; Airey, G., Chemically modified bitumens with enhanced rheology and adhesion properties to siliceous aggregates. *Construction and Building Materials* **2015,** *93*, 766-774.
69. Esfandabad, A. S.; Motevalizadeh, S. M.; Sedghi, R.; Ayar, P.; Asgharzadeh, S. M., Fracture and mechanical properties of asphalt mixtures containing granular polyethylene terephthalate (PET). *Construction and Building Materials* **2020,** *259*, 120410.
70. Fang, C.; Jiao, L.; Hu, J.; Yu, Q.; Guo, D.; Zhou, X.; Yu, R., Viscoelasticity of Asphalt Modified With Packaging Waste Expended Polystyrene. *Journal of Materials Science & Technology* **2014,** *30* (9), 939-943.
71. Schyns, Z. O.; Shaver, M. P., Mechanical recycling of packaging plastics: A review. *Macromolecular rapid communications* **2021,** *42* (3), 2000415.
72. Charitopoulou, M. A.; Kalogiannis, K. G.; Lappas, A. A.; Achilias, D. S., Novel trends in the thermo-chemical recycling of plastics from WEEE containing brominated flame retardants. *Environmental Science and Pollution Research* **2021,** *28* (42), 59190-59213.
73. Maris, J.; Bourdon, S.; Brossard, J.-M.; Cauret, L.; Fontaine, L.; Montembault, V., Mechanical recycling: Compatibilization of mixed thermoplastic wastes. *Polymer Degradation and Stability* **2018,** *147*, 245-266.
74. Garcia-Manyes, S.; Beedle, A. E., Steering chemical reactions with force. *Nature Reviews Chemistry* **2017,** *1* (11), 1-16.
75. Vinu, R.; Ojha, D.; Nair, V., Polymer pyrolysis for resource recovery. **2016**.
76. Ma, C.; Yu, J.; Wang, B.; Song, Z.; Xiang, J.; Hu, S.; Su, S.; Sun, L., Chemical recycling of brominated flame retarded plastics from e-waste for clean fuels production: a review. *Renewable and Sustainable Energy Reviews* **2016,** *61*, 433-450.
77. Babadagli, T., Development of mature oil fields — A review. *Journal of Petroleum Science and Engineering* **2007,** *57*, 221-246.
78. Alvarado, V.; Manrique, E., Enhanced Oil Recovery: An Update Review. *Energies* **2010,** *3*.

79. Srivastava, R. K.; Huang, S. S., Laboratory Investigation Of Weyburn Co2 Miscible Flooding. In *Technical Meeting / Petroleum Conference of The South Saskatchewan Section*, Petroleum Society of Canada: Regina, 1997; p 21.
80. Alquriaishi, A. A.; Shokir, E. M. E.-M., Experimental Investigation of Miscible CO2 Flooding. *Petroleum Science and Technology* **2011,** *29* (19), 2005-2016.
81. Zhang, Y. P.; Sayegh, S. G.; Luo, P.; Huang, S., Experimental Investigation of Immiscible Gas Process Performance for Medium Oil. *SPE-133203-PA* **2010,** *49* (02), 32-39.
82. Sigmund, P. M.; Kerr, W.; MacPherson, R. E., A Laboratory and Computer Model Evaluation of Immiscible CO2 Flooding in a Low-Temperature Reservoir. In *SPE Enhanced Oil Recovery Symposium*, Society of Petroleum Engineers: Tulsa, Oklahoma, 1984; p 10.
83. Mayer, E. H.; Earlougher, R. C., Sr.; Spivak, A.; Costa, A., Analysis of Heavy-Oil Immiscible CO2 Tertiary Coreflood Data. *SPE-14901-PA* **1988,** *3* (01), 69-75.
84. Wang, S.; Chen, C.; Shiau, B.; Harwell, J. H., In-situ CO2 generation for EOR by using urea as a gas generation agent. *Fuel* **2018,** *217*, 499-507.
85. Hussain, S., Numerical Mechanistic Study of In-Situ CO2 EOR–Kinetics and Recovery Performance Analysis. **2021**.
86. Bagci, A. S., Immiscible CO2 Flooding through Horizontal Wells. *Energy Sources, Part A: Recovery, Utilization, and Environmental Effects* **2007,** *29* (1), 85-95.
87. Hashemi Fath, A.; Pouranfard, A.-R., Evaluation of miscible and immiscible CO2 injection in one of the Iranian oil fields. *Egyptian Journal of Petroleum* **2014,** *23* (3), 255-270.
88. Cao, M.; Gu, Y., Oil recovery mechanisms and asphaltene precipitation phenomenon in immiscible and miscible CO2 flooding processes. *Fuel* **2013,** *109*, 157-166.
89. Ghedan, S. G., Global Laboratory Experience of CO2-EOR Flooding. In *SPE/EAGE Reservoir Characterization and Simulation Conference*, Society of Petroleum Engineers: Abu Dhabi, UAE, 2009; p 15.
90. Frenkel, D.; Smit, B., *Understanding molecular simulation: from algorithms to applications*. Elsevier: 2001; Vol. 1.
91. Allen, M. P., Introduction to molecular dynamics simulation. *Computational soft matter: from synthetic polymers to proteins* **2004,** *23* (1), 1-28.
92. Chen, Z.; Pei, J.; Li, R.; Xiao, F., Performance characteristics of asphalt materials based on molecular dynamics simulation–A review. *Construction and Building Materials* **2018,** *189*, 695-710.
93. Pacheco-Sánchez, J.; Alvarez-Ramirez, F.; Martínez-Magadán, J., Morphology of aggregated asphaltene structural models. *Energy & Fuels* **2004,** *18* (6), 1676-1686.
94. Zhang, L.; Greenfield, M. L., Molecular Orientation in Model Asphalts Using Molecular Simulation. *Energy & Fuels* **2007,** *21* (2), 1102-1111.
95. Artok, L.; Su, Y.; Hirose, Y.; Hosokawa, M.; Murata, S.; Nomura, M., Structure and reactivity of petroleum-derived asphaltene. *Energy & Fuels* **1999,** *13* (2), 287-296.
96. Groenzin, H.; Mullins, O. C., Molecular size and structure of asphaltenes from various sources. *Energy & Fuels* **2000,** *14* (3), 677-684.
97. Li, D. D.; Greenfield, M. L., Chemical compositions of improved model asphalt systems for molecular simulations. *Fuel* **2014,** *115*, 347-356.
98. Wang, P.; Dong, Z.-j.; Tan, Y.-q.; Liu, Z.-y., Investigating the Interactions of the Saturate, Aromatic, Resin, and Asphaltene Four Fractions in Asphalt Binders by Molecular Simulations. *Energy & Fuels* **2015,** *29* (1), 112-121.
99. Jennings, P.; Pribanic, J.; Desando, M.; Raub, M.; Moats, R.; Smith, J.; Mendes, T.; McGrane, M.; Fanconi, B.; VanderHart, D. *Binder characterization and evaluation by nuclear magnetic resonance spectroscopy*; 1993.
100. Bhasin, A.; Bommavaram, R.; Greenfield, M. L.; Little, D. N., Use of molecular dynamics to investigate self-healing mechanisms in asphalt binders. *Journal of Materials in Civil Engineering* **2011,** *23* (4), 485-492.

101. Sun, D.; Sun, G.; Zhu, X.; Ye, F.; Xu, J., Intrinsic temperature sensitive self-healing character of asphalt binders based on molecular dynamics simulations. *Fuel* **2018,** *211*, 609-620.
102. Samieadel, A.; Oldham, D.; Fini, E. H., Multi-scale characterization of the effect of wax on intermolecular interactions in asphalt binder. *Construction and building materials* **2017,** *157*, 1163-1172.
103. Yao, H.; Dai, Q.; You, Z., Molecular dynamics simulation of physicochemical properties of the asphalt model. *Fuel* **2016,** *164*, 83-93.
104. Li, D. D.; Greenfield, M. L., Viscosity, relaxation time, and dynamics within a model asphalt of larger molecules. *The Journal of Chemical Physics* **2014,** *140* (3), 034507.
105. Ding, Y.; Huang, B.; Shu, X.; Zhang, Y.; Woods, M. E., Use of molecular dynamics to investigate diffusion between virgin and aged asphalt binders. *Fuel* **2016,** *174*, 267-273.
106. Tarefder, R. A.; Arisa, I., Molecular dynamic simulations for determining change in thermodynamic properties of asphaltene and resin because of aging. *Energy & Fuels* **2011,** *25* (5), 2211-2222.
107. Petersen, J.; Harnsberger, P.; Robertson, R., Factors affecting the kinetics and mechanisms of asphalt oxidation and the relative effects of oxidation products on age hardening. *Preprints of Papers, American Chemical Society, Division of Fuel Chemistry* **1996,** *41* (CONF-960807-).
108. Lau, C.; Lunsford, K.; Glover, C.; Davison, R.; Bullin, J., Reaction rates and hardening susceptibilities as determined from pressure oxygen vessel aging of asphalts. *Transportation Research Record* **1992,** (1342).
109. Dorrence, S. M.; Barbour, F. A.; Petersen, J. C., Direct evidence of ketones in oxidized asphalts. *Analytical Chemistry* **1974,** *46* (14), 2242-2244.
110. Chang, Q.; O'Rear, E. A.; Ghos, S.; Zaman, M.; Huang, L.; Wu, X., An Atomistic Model of Aged Asphalt Guided by the Oxidation Chemistry of Benzylic Carbon with Application to Asphalt Rejuvenated with a Triglyceride. *Available at SSRN 4167609*.
111. Pan, J.; Tarefder, R. A., Investigation of asphalt aging behaviour due to oxidation using molecular dynamics simulation. *Molecular Simulation* **2016,** *42* (8), 667-678.
112. Qu, X.; Liu, Q.; Guo, M.; Wang, D. W.; Oeser, M., Study on the effect of aging on physical properties of asphalt binder from a microscale perspective. *Construction and Building Materials* **2018,** *187*, 718-729.
113. Xu, G.; Wang, H.; Sun, W., Molecular dynamics study of rejuvenator effect on RAP binder: Diffusion behavior and molecular structure. *Construction and Building Materials* **2018,** *158*, 1046-1054.
114. Aimoli, C. G.; Maginn, E. J.; Abreu, C. R., Transport properties of carbon dioxide and methane from molecular dynamics simulations. *The Journal of chemical physics* **2014,** *141* (13), 134101.
115. Zhang, X.-P.; Liu, Y.-Q.; Chang, Q.-H.; Zeng, R., Phase equilibria in the ternary systems LiCl–LiBr–H2O and LiCl–LiBr–CH3OH at 298 K. *Journal of Molecular Liquids* **2022,** *366*, 120318.
116. Kumar, P.; Varanasi, S. R.; Yashonath, S., Relation Between the Diffusivity, Viscosity, and Ionic Radius of LiCl in Water, Methanol, and Ethylene Glycol: A Molecular Dynamics Simulation. *The Journal of Physical Chemistry B* **2013,** *117* (27), 8196-8208.
117. Li, P.; Jiang, Z.; Zheng, M. i.; Bi, H. e.; Chen, L. e., Estimation of shale gas adsorption capacity of the Longmaxi Formation in the Upper Yangtze Platform, China. *Journal of Natural Gas Science & Engineering* **2016,** *34*, 1034-1043.
118. Guo, S.; Hou, B., A logging calculation method for shale adsorbed gas content and its application. *Journal of Petroleum Science and Engineering* **2017,** *150*, 250-256.
119. Xiong, J.; Liu, K.; Liu, X.; Liang, L.; Zeng, Q., Molecular simulation of methane adsorption in slit-like quartz pores. *RSC advances* **2016,** *6* (112), 110808-110819.

120. Sharma, A.; Namsani, S.; Singh, J. K., Molecular simulation of shale gas adsorption and diffusion in inorganic nanopores. *Molecular Simulation* **2015,** *41* (5-6), 414-422.
121. Zhai, Z.; Wang, X.; Jin, X.; Sun, L.; Li, J.; Cao, D., Adsorption and diffusion of shale gas reservoirs in modeled clay minerals at different geological depths. *Energy & Fuels* **2014,** *28* (12), 7467-7473.
122. Zhang, L.; Liu, C.; Li, Q., Molecular simulations of competitive adsorption behavior between CH4-C2H6 in K-illite clay at supercritical conditions. *Fuel* **2020,** *260*, 116358.
123. Ju, Y.; He, J.; Chang, E.; Zheng, L., Quantification of CH4 adsorption capacity in kerogen-rich reservoir shales: An experimental investigation and molecular dynamic simulation. *Energy* **2019,** *170*, 411-422.
124. Li, Z.-Z.; Min, T.; Kang, Q.; He, Y.-L.; Tao, W.-Q., Investigation of methane adsorption and its effect on gas transport in shale matrix through microscale and mesoscale simulations. *International Journal of Heat and Mass Transfer* **2016,** *98*, 675-686.
125. Wang, S.; Feng, Q.; Javadpour, F.; Xia, T.; Li, Z., Oil adsorption in shale nanopores and its effect on recoverable oil-in-place. *International Journal of Coal Geology* **2015,** *147*, 9-24.
126. Wu, H.; Chen, J.; Liu, H., Molecular dynamics simulations about adsorption and displacement of methane in carbon nanochannels. *The Journal of Physical Chemistry C* **2015,** *119* (24), 13652-13657.
127. Zhang, T.; He, Y.; Yang, Y.; Wu, K., Molecular simulation of shale gas adsorption in organic-matter nanopore. *Journal of Natural Gas Geoscience* **2017,** *2* (5-6), 323-332.
128. Chang, Q.; Huang, L.; Wu, X. In *Combination of simplified local density theory and molecular dynamics simulation to study the local density distribution of hydrocarbon gas in shale gas reservoir*, SPE Eastern Regional Meeting, OnePetro: 2019.
129. Chang, Q., Using Molecular Dynamics Simulation to Study Behavior of Hydrocarbon Fluid. **2019**.
130. Ohba, T.; Kaneko, K.; Yudasaka, M.; Iijima, S.; Takase, A.; Kanoh, H., Cooperative adsorption of supercritical CH4 in single-walled carbon nanohorns for compensation of nanopore potential. *The Journal of Physical Chemistry C* **2012,** *116* (41), 21870-21873.
131. Yuan, Q.; Zhu, X.; Lin, K.; Zhao, Y.-P., Molecular dynamics simulations of the enhanced recovery of confined methane with carbon dioxide. *Physical Chemistry Chemical Physics* **2015,** *17* (47), 31887-31893.
132. Zhu, X.; Zhao, Y.-P., Atomic mechanisms and equation of state of methane adsorption in carbon nanopores. *The Journal of Physical Chemistry C* **2014,** *118* (31), 17737-17744.
133. Ungerer, P.; Collell, J.; Yiannourakou, M., Molecular modeling of the volumetric and thermodynamic properties of kerogen: Influence of organic type and maturity. *Energy & Fuels* **2015,** *29* (1), 91-105.
134. Zhao, T.; Li, X.; Ning, Z.; Zhao, H.; Li, M., Molecular simulation of methane adsorption on type II kerogen with the impact of water content. *Journal of Petroleum Science and Engineering* **2018,** *161*, 302-310.
135. Michalec, L.; Lísal, M., Molecular simulation of shale gas adsorption onto overmature type II model kerogen with control microporosity. *Molecular Physics* **2017,** *115* (9-12), 1086-1103.
136. Tesson, S. p.; Firoozabadi, A., Methane adsorption and self-diffusion in shale kerogen and slit nanopores by molecular simulations. *The Journal of Physical Chemistry C* **2018,** *122* (41), 23528-23542.
137. Zhou, W.; Zhang, Z.; Wang, H.; Yang, X., Molecular investigation of CO2/CH4 competitive adsorption and confinement in realistic shale kerogen. *Nanomaterials* **2019,** *9* (12), 1646.
138. Takbiri-Borujeni, A.; Kazemi, M.; Sun, T.; Mansouri-Boroujeni, M. In *Effect of kerogen type and maturity on performance of carbon dioxide storage in shale*, SPE Annual Technical Conference and Exhibition, OnePetro: 2017.

139. Pathak, M.; Huang, H.; Meakin, P.; Deo, M., Molecular investigation of the interactions of carbon dioxide and methane with kerogen: Application in enhanced shale gas recovery. *Journal of Natural Gas Science and Engineering* **2018,** *51*, 1-8.
140. Wang, T.; Tian, S.; Li, G.; Sheng, M., Selective adsorption of supercritical carbon dioxide and methane binary mixture in shale kerogen nanopores. *Journal of Natural Gas Science and Engineering* **2018,** *50*, 181-188.
141. Wang, T.; Tian, S.; Li, G.; Sheng, M.; Ren, W.; Liu, Q.; Zhang, S., Molecular Simulation of CO2/CH4 Competitive Adsorption on Shale Kerogen for CO2 Sequestration and Enhanced Gas Recovery. *The Journal of Physical Chemistry C* **2018,** *122* (30), 17009-17018.
142. Zahoor, M.; Nizamuddin, S.; Madapusi, S.; Giustozzi, F., Sustainable asphalt rejuvenation using waste cooking oil: A comprehensive review. *Journal of Cleaner Production* **2021,** *278*, 123304.
143. Stulirova, J.; Pospisil, K., Observation of bitumen microstructure changes using scanning electron microscopy. *Road materials and pavement design* **2008,** *9* (4), 745-754.
144. Jun, Y.; Minghui, G.; Troy, P.; Jianming, W.; Xiaoting, W., Study on micro-structures of asphalt by using atomic force microscopy. *Acta Petrolei Sinica (Petroleum Processing Section)* **2015,** *31* (4), 959.
145. Yu, X.; Zaumanis, M.; Dos Santos, S.; Poulikakos, L. D., Rheological, microscopic, and chemical characterization of the rejuvenating effect on asphalt binders. *Fuel* **2014,** *135*, 162-171.
146. Osmari, P. H.; Aragão, F. T. S.; Leite, L. F. M.; Simão, R. A.; da Motta, L. M. G.; Kim, Y.-R., Chemical, microstructural, and rheological characterizations of binders to evaluate aging and rejuvenation. *Transportation Research Record* **2017,** *2632* (1), 14-24.
147. Kuang, D.; Ye, Z.; Yang, L.; Liu, N.; Lu, Z.; Chen, H., Effect of Rejuvenator Containing Dodecyl Benzene Sulfonic Acid (DBSA) on Physical Properties, Chemical Components, Colloidal Structure and Micro-Morphology of Aged Bitumen. *Materials (Basel)* **2018,** *11* (8).
148. Zhang, H.; Wang, H.; Yu, J., Effect of aging on morphology of organo‐montmorillonite modified bitumen by atomic force microscopy. *Journal of Microscopy* **2011,** *242* (1), 37-45.
149. Fischer, H.; Dillingh, E., On the investigation of the bulk microstructure of bitumen – Introducing two new techniques. *Fuel* **2014,** *118*, 365-368.
150. Blom, J.; Soenen, H.; Katsiki, A.; Van den Brande, N.; Rahier, H.; Van den bergh, W., Investigation of the bulk and surface microstructure of bitumen by atomic force microscopy. *Construction and Building Materials* **2018,** *177*, 158-169.
151. Petersen, J. C.; Glaser, R., Asphalt Oxidation Mechanisms and the Role of Oxidation Products on Age Hardening Revisited. *Road Materials and Pavement Design* **2011,** *12* (4), 795-819.
152. Xu, M.; Yi, J.; Qi, P.; Wang, H.; Marasteanu, M.; Feng, D., Improved Chemical System for Molecular Simulations of Asphalt. *Energy & Fuels* **2019,** *33* (4), 3187-3198.
153. Claine Petersen, J., A DUAL, SEQUENTIAL MECHANISM FOR THE OXIDATION OF PETROLEUM ASPHALTS. *Petroleum Science and Technology* **1998,** *16* (9-10), 1023-1059.
154. Sun, W.; Wang, H., Molecular dynamics simulation of diffusion coefficients between different types of rejuvenator and aged asphalt binder. *International Journal of Pavement Engineering* **2020,** *21* (8), 966-976.
155. Chang, Q.; Huang, L.; Wu, X., A Molecular-Level Study on the Interaction Behavior between Polyethylene and Aged Asphalt. In *International Conference on Transportation and Development 2022*, 2022; pp 179-189.
156. Jorgensen, W. L.; Maxwell, D. S.; Tirado-Rives, J., Development and Testing of the OPLS All-Atom Force Field on Conformational Energetics and Properties of Organic Liquids. *Journal of the American Chemical Society* **1996,** *118* (45), 11225-11236.

157. Jorgensen, W. L.; McDonald, N. A., Development of an all-atom force field for heterocycles. Properties of liquid pyridine and diazenes. *Journal of Molecular Structure: THEOCHEM* **1998,** *424* (1), 145-155.
158. McDonald, N. A.; Jorgensen, W. L., Development of an All-Atom Force Field for Heterocycles. Properties of Liquid Pyrrole, Furan, Diazoles, and Oxazoles. *The Journal of Physical Chemistry B* **1998,** *102* (41), 8049-8059.
159. Robertson, M. J.; Tirado-Rives, J.; Jorgensen, W. L., Improved Peptide and Protein Torsional Energetics with the OPLS-AA Force Field. *Journal of Chemical Theory and Computation* **2015,** *11* (7), 3499-3509.
160. Ponnuchamy, V., A theoretical investigation of different point charges combined with GAFF and OPLS-AA for acetic anhydride. *Chemical Physics Letters* **2020,** *754*, 137707.
161. Kamath, G.; Cao, F.; Potoff, J. J., An Improved Force Field for the Prediction of the Vapor−Liquid Equilibria for Carboxylic Acids. *The Journal of Physical Chemistry B* **2004,** *108* (37), 14130-14136.
162. Nevins, D.; Spera, F., Accurate computation of shear viscosity from equilibrium molecular dynamics simulations. *Molecular Simulation* **2007,** *33* (15), 1261-1266.
163. J Evans, D.; P Morriss, G., *Statistical mechanics of nonequilbrium liquids*. ANU Press: 2007.
164. Hess, S., Rheological properties via nonequilibrium molecular dynamics: from simple towards polymeric liquids. *Journal of Non-Newtonian Fluid Mechanics* **1987,** *23*, 305-319.
165. Shan, K.; Bao, C.; Li, D.; Zheng, C., Microscopic Analysis of the Rejuvenation Mechanism and Rejuvenation Effect of Asphalt Binders. *Advances in Materials Science and Engineering* **2021,** *2021*.
166. Wei, J.; Dong, F.; Li, Y.; Zhang, Y., Relationship analysis between surface free energy and chemical composition of asphalt binder. *Construction and Building Materials* **2014,** *71*, 116-123.
167. Xu, G.; Wang, H., Study of cohesion and adhesion properties of asphalt concrete with molecular dynamics simulation. *Computational Materials Science* **2016,** *112*, 161-169.
168. Luo, L.; Chu, L.; Fwa, T., Molecular dynamics analysis of oxidative aging effects on thermodynamic and interfacial bonding properties of asphalt mixtures. *Construction and Building Materials* **2021,** *269*, 121299.
169. Liu, J.; Liu, Q.; Wang, S.; Zhang, X.; Xiao, C.; Yu, B., Molecular dynamics evaluation of activation mechanism of rejuvenator in reclaimed asphalt pavement (RAP) binder. *Construction and Building Materials* **2021,** *298*, 123898.
170. Xu, G.; Wang, H., Diffusion and interaction mechanism of rejuvenating agent with virgin and recycled asphalt binder: A molecular dynamics study. *Molecular Simulation* **2018,** *44* (17), 1433-1443.
171. Ren, S.; Liu, X.; Lin, P.; Erkens, S.; Xiao, Y., Chemo-physical characterization and molecular dynamics simulation of long-term aging behaviors of bitumen. *Construction and Building Materials* **2021,** *302*, 124437.
172. Cui, B.; Gu, X.; Hu, D.; Dong, Q., A multiphysics evaluation of the rejuvenator effects on aged asphalt using molecular dynamics simulations. *Journal of Cleaner Production* **2020,** *259*, 120629.
173. Gao, Y.; Zhang, Y.; Yang, Y.; Zhang, J.; Gu, F., Molecular dynamics investigation of interfacial adhesion between oxidised bitumen and mineral surfaces. *Applied Surface Science* **2019,** *479*, 449-462.
174. Li, L.; Xin, C.; Guan, M.; Guo, M., Using Molecular Dynamics Simulation to Analyze the Feasibility of Using Waste Cooking Oil as an Alternative Rejuvenator for Aged Asphalt. *Sustainability* **2021,** *13* (8).
175. Yao, H. Property analysis of the asphalt materials using Molecular Dynamics (MD) method. Michigan Technological University, 2016.

176. Motamed, A.; Bhasin, A.; Liechti, K. M., Using the poker-chip test for determining the bulk modulus of asphalt binders. *Mechanics of Time-Dependent Materials* **2014,** *18*, 197-215.
177. Ling, H. I.; Smyth, A.; Betti, R., *Poromechanics IV*. DEStech Publications, Inc: 2009.
178. Guo, H. Interfacial adhesion performance between the low-density polyethylene (LDPE) modified bitumen and minerals based on molecular dynamics simulations. Aston University, 2021.
179. Ding, H.; Wang, H.; Qu, X.; Varveri, A.; Gao, J.; You, Z., Towards an understanding of diffusion mechanism of bio-rejuvenators in aged asphalt binder through molecular dynamics simulation. *Journal of Cleaner Production* **2021,** *299*, 126927.
180. Maginn, E. J.; Messerly, R. A.; Carlson, D. J.; Roe, D. R.; Elliot, J. R., Best Practices for Computing Transport Properties 1. Self-Diffusivity and Viscosity from Equilibrium Molecular Dynamics [Article v1.0]. *Living Journal of Computational Molecular Science* **2018,** *1* (1), 6324.
181. Van-Oanh, N.-T.; Houriez, C.; Rousseau, B., Viscosity of the 1-ethyl-3-methylimidazolium bis(trifluoromethylsulfonyl)imide ionic liquid from equilibrium and nonequilibrium molecular dynamics. *Physical Chemistry Chemical Physics* **2010,** *12* (4), 930-936.
182. Zhang, L.; Greenfield, M., Relaxation time, diffusion, and viscosity analysis of model asphalt systems using molecular simulation. *The Journal of chemical physics* **2007,** *127*, 194502.
183. Fallah, F.; Khabaz, F.; Kim, Y.-R.; Kommidi, S. R.; Haghshenas, H. F., Molecular dynamics modeling and simulation of bituminous binder chemical aging due to variation of oxidation level and saturate-aromatic-resin-asphaltene fraction. *Fuel* **2019,** *237*, 71-80.
184. Lemarchand, C. A.; Bailey, N. P.; Todd, B. D.; Daivis, P. J.; Hansen, J. S., Non-Newtonian behavior and molecular structure of Cooee bitumen under shear flow: A non-equilibrium molecular dynamics study. *The Journal of Chemical Physics* **2015,** *142* (24), 244501.
185. Djimasbe, R.; Galiullin, E. A.; Varfolomeev, M. A.; Fakhrutdinov, R. Z.; Al-Muntaser, A. A.; Farhadian, A., Experimental study of non-oxidized and oxidized bitumen obtained from heavy oil. *Scientific Reports* **2021,** *11* (1), 8107.
186. Sonibare, K.; Rucker, G.; Zhang, L., Molecular dynamics simulation on vegetable oil modified model asphalt. *Construction and Building Materials* **2021,** *270*, 121687.
187. Qu, X.; Liu, Q.; Wang, C.; Wang, D.; Oeser, M., Effect of Co-Production of Renewable Biomaterials on the Performance of Asphalt Binder in Macro and Micro Perspectives. *Materials* **2018,** *11* (2), 244.
188. Gökalp, İ.; Uz, V. E., Utilizing of Waste Vegetable Cooking Oil in bitumen: Zero tolerance aging approach. *Construction and Building Materials* **2019,** *227*, 116695.
189. Hossain, K.; Ahmed, R. B., *Application of Waste Cooking Oil in Construction of Asphalt Pavement*. 2019.
190. Xinxin, C.; Xuejuan, C.; Boming, T.; Yuanyuan, W.; Xiaolong, L., Investigation on Possibility of Waste Vegetable Oil Rejuvenating Aged Asphalt. *Applied Sciences* **2018,** *8* (5).
191. Szewczyk, P., *Study of the Phase Behavior of Triacylglycerols Using Molecular Dynamics Simulation*. University of Alberta: 2010.
192. Asli, H.; Ahmadinia, E.; Zargar, M.; Karim, M. R., Investigation on physical properties of waste cooking oil – Rejuvenated bitumen binder. *Construction and Building Materials* **2012,** *37*, 398-405.
193. Azahar, W. N. A. W.; Jaya, R. P.; Hainin, M. R.; Bujang, M.; Ngadi, N., Chemical modification of waste cooking oil to improve the physical and rheological properties of asphalt binder. *Construction and Building Materials* **2016,** *126*, 218-226.
194. Rodrigues, C.; Capitão, S.; Picado-Santos, L.; Almeida, A., Full Recycling of Asphalt Concrete with Waste Cooking Oil as Rejuvenator and LDPE from Urban Waste as Binder Modifier. *Sustainability* **2020,** *12* (19).

195. Zhang, D.; Chen, M.; Wu, S.; Liu, J.; Amirkhanian, S., Analysis of the Relationships between Waste Cooking Oil Qualities and Rejuvenated Asphalt Properties. *Materials* **2017,** *10* (5).
196. García-Morales, M.; Partal, P.; Navarro, F. J.; Martínez-Boza, F.; Gallegos, C.; González, N.; González, O.; Muñoz, M. E., Viscous properties and microstructure of recycled eva modified bitumen. *Fuel* **2004,** *83* (1), 31-38.
197. Lemarchand, C.; Schroeder, T.; Dyre, J.; Hansen, J., Cooee bitumen: Chemical aging. *The Journal of chemical physics* **2013,** *139*, 124506.
198. Khabaz, F.; Khare, R., Glass Transition and Molecular Mobility in Styrene–Butadiene Rubber Modified Asphalt. *The Journal of Physical Chemistry B* **2015,** *119* (44), 14261-14269.
199. Robertson, R. E.; Branthaver, J.; Plancher, H.; Duvall, J.; Ensley, E.; Harnsberger, P. *Chemical properties of asphalts and their relationship to pavement performance*; Strategic Highway Research Program, National Research Council Washington, DC: 1991.
200. Shan, K.; Bao, C.; Li, D.; Zheng, C., Microscopic Analysis of the Rejuvenation Mechanism and Rejuvenation Effect of Asphalt Binders. *Advances in Materials Science and Engineering* **2021,** *2021*, 1958968.
201. Zhu, H.; Xu, G.; Gong, M.; Yang, J., Recycling long-term-aged asphalts using bio-binder/plasticizer-based rejuvenator. *Construction and building materials* **2017,** *147*, 117-129.
202. Zhao, M.; Shen, F.; Ding, Q., Micromechanism of the dispersion behavior of polymer-modified rejuvenators in aged asphalt material. *Applied Sciences* **2018,** *8* (9), 1591.
203. Radhakrishnan, V.; Sri, M. R.; Reddy, K. S., Evaluation of asphalt binder rutting parameters. *Construction and Building Materials* **2018,** *173*, 298-307.
204. Hong, W.; Mo, L.; Pan, C.; Riara, M.; Wei, M.; Zhang, J., Investigation of rejuvenation and modification of aged asphalt binders by using aromatic oil-SBS polymer blend. *Construction and Building Materials* **2020,** *231*, 117154.
205. Du, Z.; Jiang, C.; Yuan, J.; Xiao, F.; Wang, J., Low temperature performance characteristics of polyethylene modified asphalts–A review. *Construction and Building Materials* **2020,** *264*, 120704.
206. Peng, C.; Guo, C.; You, Z.; Xu, F.; Ma, W.; You, L.; Li, T.; Zhou, L.; Huang, S.; Ma, H., The Effect of Waste Engine Oil and Waste Polyethylene on UV Aging Resistance of Asphalt. *Polymers* **2020,** *12* (3), 602.
207. Ye, X.; Zou, X.; Tian, F.; He, H., Feasibility study on recycled vegetable oil waste and recycled polyethylene for the modification of aged asphalt. *Plos one* **2021,** *16* (1), e0244159.
208. Yan, L.; Li, M.; Li, Q.; Li, H., Modified asphalt based on polyethylene with broad molecular weight distribution. *Construction and Building Materials* **2020,** *260*, 119707.
209. Li, M.; Luo, C.; Zhu, L.; Li, H.; Cong, P.; Feng, Y.; Yan, L., A novel epoxy-terminated polyethylene modified asphalt with low-viscosity and high storage stability. *Construction and Building Materials* **2022,** *335*, 127473.
210. Peng, C.; Lu, L.; You, Z.; Xu, F.; Zhou, L.; Ma, H.; Hu, Y.; Liu, Y., Influence of Waste Polyethylene on the Performances of Asphalt before and after Oxidative Aging Based on the Molecular Dynamics Simulation. *Journal of Materials in Civil Engineering* **2022,** *34* (10), 04022274.
211. Li, C.; Zhang, Y.; Zhang, Y., Melt grafting of maleic anhydride onto low-density polyethylene/polypropylene blends. *Polymer testing* **2003,** *22* (2), 191-195.
212. Polacco, G.; Berlincioni, S.; Biondi, D.; Stastna, J.; Zanzotto, L., Asphalt modification with different polyethylene-based polymers. *European polymer journal* **2005,** *41* (12), 2831-2844.
213. Zhang, H.; Wu, X.; Cao, D.; Zhang, Y.; He, M., Effect of linear low density-polyethylene grafted with maleic anhydride (LLDPE-g-MAH) on properties of high density-polyethylene/styrene–butadiene–styrene (HDPE/SBS) modified asphalt. *Construction and Building Materials* **2013,** *47*, 192-198.

214. Painter, P. C.; Coleman, M. M., *Fundamentals of polymer science: an introductory text*. Routledge: 2019.
215. Yu, C.; Hu, K.; Yang, Q.; Wang, D.; Zhang, W.; Chen, G.; Kapyelata, C., Analysis of the Storage Stability Property of Carbon Nanotube/Recycled Polyethylene-Modified Asphalt Using Molecular Dynamics Simulations. *Polymers* **2021,** *13* (10).
216. Liu, Y.; Tang, Y.; Chang, Q.; Ma, C.; He, S.; Yuan, L., Development of a novel heat- and shear-resistant nano-silica gelling agent. *Nanotechnology Reviews* **2022,** *11* (1), 2786-2799.
217. Moody, V.; Needles, H. L., 3 - Major Fibers and Their Properties. In *Tufted Carpet*, Moody, V.; Needles, H. L., Eds. William Andrew Publishing: Norwich, NY, 2004; pp 35-59.
218. Guo, F.; Zhang, J.; Pei, J.; Zhou, B.; Falchetto, A. C.; Hu, Z., Investigating the interaction behavior between asphalt binder and rubber in rubber asphalt by molecular dynamics simulation. *Construction and Building Materials* **2020,** *252*, 118956.
219. Punith, V.; Veeraragavan, A., Behavior of asphalt concrete mixtures with reclaimed polyethylene as additive. *Journal of materials in civil engineering* **2007,** *19* (6), 500-507.
220. Ghuzlan, K. A.; Al-Khateeb, G. G.; Qasem, Y., Rheological properties of polyethylene-modified asphalt binder. *Athens Journal of Technology and Engineering* **2013,** *10*, 1-14.
221. Dalhat, M.; Al-Abdul Wahhab, H., Performance of recycled plastic waste modified asphalt binder in Saudi Arabia. *International Journal of Pavement Engineering* **2017,** *18* (4), 349-357.
222. Hussein, I. A.; Iqbal, M. H.; Al-Abdul-Wahhab, H. I., Influence of Mw of LDPE and vinyl acetate content of EVA on the rheology of polymer modified asphalt. *Rheologica acta* **2005,** *45* (1), 92-104.
223. Nizamuddin, S.; Jamal, M.; Gravina, R.; Giustozzi, F., Recycled plastic as bitumen modifier: The role of recycled linear low-density polyethylene in the modification of physical, chemical and rheological properties of bitumen. *Journal of Cleaner Production* **2020,** *266*, 121988.
224. Rappe, A. K.; Goddard III, W. A., Charge equilibration for molecular dynamics simulations. *The Journal of Physical Chemistry* **1991,** *95* (8), 3358-3363.
225. Martin, M. G.; Siepmann, J. I., Novel configurational-bias Monte Carlo method for branched molecules. Transferable potentials for phase equilibria. 2. United-atom description of branched alkanes. *The Journal of Physical Chemistry B* **1999,** *103* (21), 4508-4517.
226. Mayo, S. L.; Olafson, B. D.; Goddard, W. A., DREIDING: a generic force field for molecular simulations. *The Journal of Physical Chemistry* **1990,** *94* (26), 8897-8909.
227. Lesueur, D., The colloidal structure of bitumen: Consequences on the rheology and on the mechanisms of bitumen modification. *Advances in colloid and interface science* **2009,** *145* (1-2), 42-82.
228. González, O.; Munoz, M.; Santamaría, A., Bitumen/polyethylene blends: using m-LLDPEs to improve stability and viscoelastic properties. *Rheologica acta* **2006,** *45* (5), 603-610.
229. Li, C.; Gong, J.; Zhao, R.; Xi, Z.; Wang, Q.; Xie, H., Laboratory performance of recycled polyethylene modified epoxy asphalt binders. *International Journal of Pavement Engineering* **2022**, 1-11.
230. Grigg, R. B.; Schechter, D. S. In *State of the Industry in CO2 Floods*, SPE Annual Technical Conference and Exhibition, 1997.
231. Markewitz, P.; Kuckshinrichs, W.; Leitner, W.; Linssen, J.; Zapp, P.; Bongartz, R.; Schreiber, A.; Müller, T. E., Worldwide innovations in the development of carbon capture technologies and the utilization of CO 2. *Energy & environmental science* **2012,** *5* (6), 7281-7305.
232. Wang, S.; Kadhum, M. J.; Chen, C.; Shiau, B.; Harwell, J. H., Development of in Situ CO2 Generation Formulations for Enhanced Oil Recovery. *Energy & Fuels* **2017,** *31* (12), 13475-13486.

233. Zhu, D.; Hou, J.; Wang, J.; Wu, X.; Wang, P.; Bai, B., Acid-alternating-base (AAB) technology for blockage removal and enhanced oil recovery in sandstone reservoirs. *Fuel* **2018,** *215*, 619-630.
234. Wang, S.; Chen, C.; Li, K.; Yuan, N.; Shiau, B.; Harwell, J. H., In situ CO2 enhanced oil recovery: parameters affecting reaction kinetics and recovery performance. *Energy & Fuels* **2019,** *33* (5), 3844-3854.
235. Georgiadis, A.; Maitland, G.; Trusler, J. P. M.; Bismarck, A., Interfacial Tension Measurements of the (H2O + CO2) System at Elevated Pressures and Temperatures. *Journal of Chemical & Engineering Data* **2010,** *55* (10), 4168-4175.
236. Abedini, A.; Torabi, F., Oil Recovery Performance of Immiscible and Miscible CO2 Huff-and-Puff Processes. *Energy & Fuels* **2014,** *28* (2), 774-784.
237. Abedini, A.; Torabi, F., On the CO2 storage potential of cyclic CO2 injection process for enhanced oil recovery. *Fuel* **2014,** *124*, 14-27.
238. Sharbatian, A.; Abedini, A.; Qi, Z.; Sinton, D., Full Characterization of CO2–Oil Properties On-Chip: Solubility, Diffusivity, Extraction Pressure, Miscibility, and Contact Angle. *Analytical Chemistry* **2018,** *90* (4), 2461-2467.
239. Mosavat, N.; Abedini, A.; Torabi, F., Phase Behaviour of CO2–Brine and CO2–Oil Systems for CO2 Storage and Enhanced Oil Recovery: Experimental Studies. *Energy Procedia* **2014,** *63*, 5631-5645.
240. Abedini, A.; Mosavat, N.; Torabi, F., Determination of Minimum Miscibility Pressure of Crude Oil–CO2 System by Oil Swelling/Extraction Test. *Energy Technology* **2014,** *2* (5), 431-439.
241. Ungar, F.; Ahitan, S.; Worthing, S.; Abedini, A.; Uleberg, K.; Yang, T., A new fluidics method to determine minimum miscibility pressure. *Journal of Petroleum Science and Engineering* **2022,** *208*, 109415.
242. Georgiadis, A.; Maitland, G.; Trusler, J. P. M.; Bismarck, A., Interfacial Tension Measurements of the (H2O + n-Decane + CO2) Ternary System at Elevated Pressures and Temperatures. *Journal of Chemical & Engineering Data* **2011,** *56* (12), 4900-4908.
243. Liu, B.; Shi, J.; Wang, M.; Zhang, J.; Sun, B.; Shen, Y.; Sun, X., Reduction in Interfacial Tension of Water-Oil Interface by Supercritical CO2 in Enhanced Oil Recovery Processes studied with Molecular Dynamics Simulation. *The Journal of Supercritical Fluids* **2015,** *111*.
244. Zhao, L.; Tao, L.; Lin, S., Molecular Dynamics Characterizations of the Supercritical CO2–Mediated Hexane–Brine Interface. *Industrial & Engineering Chemistry Research* **2015,** *54* (9), 2489-2496.
245. Mohammed, S.; Mansoori, G. A., The Role of Supercritical/Dense CO2 Gas in Altering Aqueous/Oil Interfacial Properties: A Molecular Dynamics Study. *Energy & Fuels* **2018,** *32* (2), 2095-2103.
246. Choudhary, N.; Anwari Che Ruslan, M. F.; Narayanan Nair, A. K.; Qiao, R.; Sun, S., Bulk and interfacial properties of the decane+ brine system in the presence of carbon dioxide, methane, and their mixture. *Industrial & Engineering Chemistry Research* **2021,** *60* (30), 11525-11534.
247. Yang, Y.; Nair, A. K. N.; Ruslan, M. F. A. C.; Sun, S., Interfacial properties of the alkane+ water system in the presence of carbon dioxide and hydrophobic silica. *Fuel* **2022,** *310*, 122332.
248. Yang, Y.; Narayanan Nair, A. K.; Anwari Che Ruslan, M. F.; Sun, S., Bulk and Interfacial Properties of the Decane + Water System in the Presence of Methane, Carbon Dioxide, and Their Mixture. *The Journal of Physical Chemistry B* **2020,** *124* (43), 9556-9569.
249. Yang, Y.; Narayanan Nair, A. K.; Sun, S., Molecular Dynamics Simulation Study of Carbon Dioxide, Methane, and Their Mixture in the Presence of Brine. *The Journal of Physical Chemistry B* **2017,** *121* (41), 9688-9698.

250. Sun, C.-Y.; Chen, G.-J., Measurement of Interfacial Tension for the CO2 Injected Crude Oil + Reservoir Water System. *Journal of Chemical & Engineering Data* **2005,** *50* (3), 936-938.
251. Mohammed, S.; Mansoori, G. A., Effect of CO2 on the Interfacial and Transport Properties of Water/Binary and Asphaltenic Oils: Insights from Molecular Dynamics. *Energy & Fuels* **2018,** *32* (4), 5409-5417.
252. Fakher, S.; Imqam, A., A data analysis of immiscible carbon dioxide injection applications for enhanced oil recovery based on an updated database. *SN Applied Sciences* **2020,** *2* (3), 448.
253. Levitt, D. B.; Jackson, A. C.; Heinson, C.; Britton, L. N.; Malik, T.; Dwarakanath, V.; Pope, G. A., Identification and evaluation of high-performance EOR surfactants. *SPE-180076-PA* **2009,** *12* (02), 243-253.
254. Tavassoli, S.; Korrani, A. K.; Pope, G. A.; Sepehrnoori, K., Low-salinity surfactant flooding—a multimechanistic enhanced-oil-recovery method. *Spe Journal* **2016,** *21* (03), 0744-0760.
255. Martin, M. G.; Siepmann, J. I., Transferable Potentials for Phase Equilibria. 1. United-Atom Description of n-Alkanes. *The Journal of Physical Chemistry B* **1998,** *102* (14), 2569-2577.
256. Harris, J. G.; Yung, K. H., Carbon dioxide's liquid-vapor coexistence curve and critical properties as predicted by a simple molecular model. *The Journal of Physical Chemistry* **1995,** *99* (31), 12021-12024.
257. Zhong, H.; Lai, S.; Wang, J.; Qiu, W.; Lüdemann, H.-D.; Chen, L., Molecular Dynamics Simulation of Transport and Structural Properties of CO2 Using Different Molecular Models. *Journal of Chemical & Engineering Data* **2015,** *60* (8), 2188-2196.
258. Mark, P.; Nilsson, L., Structure and dynamics of the TIP3P, SPC, and SPC/E water models at 298 K. *The Journal of Physical Chemistry A* **2001,** *105* (43), 9954-9960.
259. Pu, J.; Qin, X.; Gou, F.; Fang, W.; Peng, F.; Wang, R.; Guo, Z., Molecular Modeling of CO2 and n-Octane in Solubility Process and α-Quartz Nanoslit. *Energies* **2018,** *11* (11), 3045.
260. Zhang, Y.; Feller, S. E.; Brooks, B. R.; Pastor, R. W., Computer simulation of liquid/liquid interfaces. I. Theory and application to octane/water. *The Journal of chemical physics* **1995,** *103* (23), 10252-10266.
261. Minkara, M. S.; Josephson, T.; Venteicher, C. L.; Chen, J. L.; Stein, D. J.; Peters, C. J.; Siepmann, J. I., Monte Carlo simulations probing the liquid/vapour interface of water/hexane mixtures: adsorption thermodynamics, hydrophobic effect, and structural analysis. *Molecular Physics* **2018,** *116* (21-22), 3283-3291.
262. Yang, Z.; Li, M.; Peng, B.; Lin, M.; Dong, Z., Dispersion Property of CO2 in Oil. 1. Volume Expansion of CO2 + Alkane at near Critical and Supercritical Condition of CO2. *Journal of Chemical & Engineering Data* **2012,** *57* (3), 882-889.
263. Zhang, J.; Pan, Z.; Liu, K.; Burke, N., Molecular Simulation of CO2 Solubility and Its Effect on Octane Swelling. *Energy & Fuels* **2013,** *27* (5), 2741-2747.
264. Ashcroft, S. J.; Isa, M. B., Effect of Dissolved Gases on the Densities of Hydrocarbons. *Journal of Chemical & Engineering Data* **1997,** *42* (6), 1244-1248.
265. Bahadori, A.; Mokhatab, S., New correlations predict aqueous solubility and density of carbon dioxide. *International Journal of Greenhouse Gas Control* **2009,** *3*, 474-480.
266. Lake, L. W.; Lotfollahi, M.; Bryant, S. L., CO2 enhanced oil recovery experience and its messages for CO2 storage. In *Science of Carbon Storage in Deep Saline Formations*, Elsevier: 2019; pp 15-31.
267. Yuet, P. K.; Blankschtein, D., Molecular Dynamics Simulation Study of Water Surfaces: Comparison of Flexible Water Models. *The Journal of Physical Chemistry B* **2010,** *114* (43), 13786-13795.
268. Al-Sahhaf, T.; Elkamel, A.; Suttar Ahmed, A.; Khan, A. R., The Influence of Temperature, Pressure, Salinity, and Surfactant Concentration on the Interfacial Tension of the N-Octane-Water System. *Chemical Engineering Communications* **2005,** *192* (5), 667-684.

269. Yang, D.; Tontiwachwuthikul, P.; Gu, Y., Interfacial Tensions of the Crude Oil + Reservoir Brine + CO2 Systems at Pressures up to 31 MPa and Temperatures of 27 °C and 58 °C. *Journal of Chemical & Engineering Data* **2005,** *50* (4), 1242-1249.
270. Zhang, L.; Greenfield, M. L., Rotational relaxation times of individual compounds within simulations of molecular asphalt models. *The Journal of Chemical Physics* **2010,** *132* (18), 184502.
271. You, L.; Spyriouni, T.; Dai, Q.; You, Z.; Khanal, A., Experimental and molecular dynamics simulation study on thermal, transport, and rheological properties of asphalt. *Construction and Building Materials* **2020,** *265*, 120358.
272. Bilema, M.; Aman, M.; Hassan, N.; Abdullah, N. In *Investigation on rheology and physical properties of asphalt binder blended with waste cooking oil*, IOP Conference Series: Materials Science and Engineering, IOP Publishing: 2019; p 012045.
273. Zhai, H.; Salomon, D., Evaluation of Low-Temperature Properties and the Fragility of Asphalt Binders with Non-Arrhenius Viscosity–Temperature Dependence. *Transportation Research Record* **2005,** *1901* (1), 44-51.
274. Poh, C.; Hassan, N. In *The Effect of Oil Palm Waste Pyrolysis Bio-oil on Modified Bitumen Properties*, 2016.
275. Tenney, C. M.; Maginn, E. J., Limitations and recommendations for the calculation of shear viscosity using reverse nonequilibrium molecular dynamics. *The Journal of chemical physics* **2010,** *132* (1), 014103.
276. Gordon, P. A., Characterizing Isoparaffin Transport Properties with Stokes−Einstein Relationships. *Industrial & Engineering Chemistry Research* **2003,** *42* (26), 7025-7036.
277. Hussain, S.; Wu, X.; Shiau, B., Numerical Mechanistic Study of In-Situ CO2 EOR – Kinetics and Recovery Performance Analysis. In *SPE Annual Technical Conference and Exhibition*, 2021; p D012S068R001.
278. Chang, Q.; Huang, L.; Wu, X., A Molecular Dynamics Study on Low-Pressure Carbon Dioxide in the Water/Oil Interface for Enhanced Oil Recovery. *SPE Journal* **2022**, 1-10.